

Quantification of the Infrared Water Vapor Continuum by Atmospheric Measurements

Andreas Reichert



Karlsruher Institut für Technologie

München 2016

Quantification of the Infrared Water Vapor Continuum by Atmospheric Measurements

Andreas Reichert

Dissertation
an der Fakultät für Physik
der Ludwig-Maximilians-Universität
München

angefertigt am
Karlsruher Institut für Technologie (KIT)
Institut für Meteorologie und Klimaforschung
Atmosphärische Umweltforschung (IMK-IFU)
Garmisch-Partenkirchen

vorgelegt von
Andreas Reichert
aus Kösching

München, 24.10.2016

Erstgutachter: PD Dr. Ralf Sussmann

Zweitgutachter: Prof. Dr. Bernhard Mayer

Tag der mündlichen Prüfung: 24.11.2016

Zusammenfassung

Ziel der vorliegenden Arbeit ist eine verbesserte Quantifizierung des Wasserdampfkontinuums mittels atmosphärengestützter Messungen. Das Wasserdampfkontinuum stellt neben der Linienabsorption und -emission einen signifikanten Beitrag zur Wechselwirkung infraroter Strahlung mit atmosphärischem Wasserdampf dar. Aufgrund einer Reihe von Einschränkungen bisheriger labor- und atmosphärenbasierter Untersuchungen fehlt für weite Teile des infraroten Spektralbereichs eine genaue Quantifizierung des Wasserdampfkontinuums durch Messungen unter atmosphärentypischen Bedingungen. Dies führt zu signifikanten Unsicherheiten in Strahlungstransportsimulationen der Atmosphäre sowie den darauf basierenden Klimamodellen und Fernerkundungsverfahren, weshalb eine genaue quantitative Beschreibung der Wasserdampf-Strahlungsprozesse von entscheidender Bedeutung ist.

Die Grundlage der vorgestellten Untersuchung bildet ein Strahlungs-Schließungsexperiment, d.h. eine quantitativer Vergleich von Messungen der spektralen Strahldichte mit Modellrechnungen, der den Spektralbereich von 400 bis 7800 cm^{-1} (1.3–25.0 μm) abdeckt. Als Standort für dieses Experiment dient das Höhenobservatorium Zugspitze (47.42° N , 10.98° O , 2964 m ü. NN). Die Auswertung beruht auf spektral hochauflösten Messungen der thermischen Emission der Atmosphäre im fernen Infrarot sowie FTIR (Fourier Transform Infrarot)-Messungen solarer Absorptionsspektren im nahen Infrarot. Eine Reihe von neu entwickelten Methoden erlaubt eine Verbesserung der Sensitivität des Schließungsexperiments gegenüber bisherigen Studien sowie eine Abdeckung von bisher für atmosphärenbasierte Studien unzugänglichen Spektralbereichen. Dies umfasst u.a. neue Ansätze zur Korrektur der Effekte von Positionierungenauigkeiten bei Sonnenabsorptionsspektrometern sowie zur radiometrischen Kalibrierung von solaren FTIR-Messungen im nahen Infrarot.

Das vorgestellte Verfahren zur Bestimmung und Korrektur von Positionierungenauigkeiten beruht auf wiederholter Bestimmung der Dopplerverschiebung solarer Spektrallinien bei verschiedenen Ausrichtungen der solaren Rotationsachse relativ zur Zenitrichtung. Im Rahmen der Schließung verbessert dieses Korrekturverfahren die Genauigkeit der verwendeten Spurengas-Säulenmessungen sowie der radiometrischen Kalibrierung im nahen Infrarot. Die Auswirkungen der Korrektur werden anhand von Zeitreihen des säulengemittelten Methan-Mischungsverhältnisses (XCH_4) demonstriert. Hierbei zeigt sich, dass die Korrektur in der Lage ist, die Übereinstimmung der XCH_4 -Trends mit dem nahegelegenen Standort Garmisch (47.48° N , 11.06° O , 743 m ü. NN) wiederherzustellen.

Die Quantifizierung des Wasserdampfkontinuums aus solaren Absorptionsspektren im nahen Infrarot erfordert eine ausreichend genaue radiometrische Kalibrierung der Spektren. Zu diesem

Zweck wurde eine Kalibriermethode entwickelt, die auf einer Kombination der Langley-Methode mit Strahldichtemessungen einer Hochtemperatur-Schwarzkörperquelle basiert und mit der eine Kalibriergenauigkeit von 1–2 % erreicht werden kann. Die Validierung dieser Methode erfolgte mittels eines Vergleichs mehrmaliger Kalibermessungen, wobei sich eine Übereinstimmung im Rahmen der Unsicherheiten für 91 % des Spektralbereichs von 2500 bis 7800 cm^{-1} ergibt. Ein zweiter Validierungsansatz bestand im Vergleich mit Strahlungstransportrechnungen, wobei für 98 % des Spektralbereichs konsistente Ergebnisse vorliegen.

Die Ergebnisse zum Ferninfrarot-Wasserdampfkontinuum (400–580 cm^{-1}) entsprechen den Vorhersagen des weitverbreiteten MT_CKD 2.5.2-Modells (Mlawer et al., 2012) sowie den Ergebnissen aktueller atmosphärenbasierter Studien zum Kontinuum. Für einen Großteil des Spektralbereichs der Nahinfrarot-Messungen stellen die hier vorgestellten Ergebnisse die ersten Messungen des Kontinuums unter atmosphärentypischen Bedingungen dar. Die trockenen Atmosphärenbedingungen am Standort Zugspitze erlauben dabei eine Quantifizierung des Kontinuums innerhalb von Wasserdampf-Absorptionsbanden, wohingegen im Zentrum von Fensterbereichen nur ein oberer Grenzwert der Kontinuumsabsorption spezifiziert werden kann. Die Ergebnisse stimmen im Rahmen der Unsicherheiten für 75 % des Spektralbereichs von 2500 bis 7800 cm^{-1} mit dem MT_CKD 2.5.2-Modell überein. Abweichungen ergeben sich u.a. für die Spektralbereiche 2800–3000 cm^{-1} und 4100–4200 cm^{-1} , in denen die gemessene Kontinuumsabsorption ca. dem 5-fachen der MT_CKD-Modellvorhersage entspricht. Die Ergebnisse des Schließungsexperiments stimmen sowohl mit den kalorimetrisch-interferometrischen Messungen von Bicknell et al. (2006) als auch den mittels Cavity Ring-Down Spektroskopie bestimmten Resultaten von Mondelain et al. (2015) überein. Im Vergleich zu den FTIR-gestützten Labormessungen von Ptashnik et al. (2012, 2013) zeigen die Schließungsmessungen für atmosphärische Bedingungen eine 2- bis 5-fach geringere Kontinuumsabsorption in den Randbereichen von Wasserdampf-Absorptionsbanden. Konkret gilt dies für die Spektralbereiche 3200–3400 cm^{-1} , 4050–4200 cm^{-1} und 6950–7050 cm^{-1} .

Die vorliegende Arbeit stellt einen signifikanten Beitrag zu Verbesserung der Quantifizierung des Wasserdampfkontinuums unter atmosphärentypischen Bedingungen dar und führt daher zu einer weiteren Verringerung der Unsicherheiten von Strahlungstransportrechnungen der Atmosphäre. Da bisher keine Messungen des Nahinfrarot-Wasserdampfkontinuums unter atmosphärentypischen Bedingungen zur Verfügung standen, sind die Ergebnisse ein wichtiges Instrument zur Validierung des MT_CKD-Modells und zur Beurteilung widersprüchlicher Ergebnisse aktueller Laborstudien in diesem Spektralbereich. Das im Rahmen dieser Arbeit aufgebaute Langzeit-Schließungsexperiment liefert außerdem die Voraussetzung, um in Zukunft weitere zentrale Fragestellungen zum Wasserdampfkontinuum zu klären. Gemäß den Ergebnissen aktueller Studien zur Klimarelevanz des Wasserdampfkontinuums (Paynter und Ramaswamy, 2014; Rädel et al., 2015) ist zu erwarten, dass die in dieser Arbeit vorgestellten Ergebnisse zu signifikanten Effekten in Klimamodellen führen. Dies umfasst u.a. eine Anpassung des oberflächennahen Energiehaushalts in Form einer Verringerung des latenten und fühlbaren Wärmestroms und in weiterer Folge eine Verringerung von Konvektion und Niederschlägen in den Tropen.

Abstract

The aim of this work is to reduce the uncertainties of atmospheric radiative transfer calculations by improving the quantitative knowledge of the water vapor continuum using atmospheric measurements. In addition to line absorption and emission, the water vapor continuum is responsible for a significant fraction of the interaction between infrared radiation and atmospheric water vapor. Due to the limitations of previous field and laboratory studies, there remains a lack of accurate measurements of the water vapor continuum throughout a significant fraction of the infrared spectral range, especially under atmospheric conditions. The consequential significant uncertainties in atmospheric radiative transfer calculations lead to possible inaccuracies in climate models and numerous remote sensing techniques. An accurate quantification of water vapor radiative processes is therefore of vital importance.

The study presented in this thesis relies on a radiative closure experiment, i.e. a quantitative comparison of spectral radiance measurements with radiative transfer calculations in the spectral interval between 400 and 7800 cm⁻¹ (1.3–25.0 μ m). The experiment was set up at the Zugspitze (47.42° N, 10.98° E, 2964 m a.s.l.) high-altitude observatory and comprises thermal atmospheric emission spectra in the far infrared and solar FTIR (Fourier transform infrared) measurements covering the near infrared. Several new methods were developed to improve the sensitivity of the closure compared to previous studies and to be able to cover spectral intervals previously not accessible to atmospheric continuum studies, e.g. a new approach for the correction of sun-pointing inaccuracies in solar absorption spectrometry and for the radiometric calibration of near-infrared solar absorption spectra.

The method for quantification and correction of systematic sun-pointing inaccuracies in solar absorption spectrometry presented in this work relies on subsequent measurements of the Doppler shift of solar lines with differing orientations of the solar rotation axis relative to the zenith direction. The proposed concept augments the sensitivity of the closure experiment by improving the accuracy of trace gas column measurements and the near-infrared radiometric calibration used in this study. The mispointing correction is demonstrated using measurement time series of dry-air column-averaged mole fractions of methane (XCH₄), for which consistency of the XCH₄ trend with results from the nearby Garmisch FTIR site (47.48° N, 11.06° E, 743 m a.s.l.) is restored by applying the correction.

Water vapor continuum quantification from near-infrared solar absorption spectra requires sufficiently accurate radiometric calibration of the measured spectra. A new calibration approach presented in this work combines the Langley technique with spectral radiance measurements of a high-temperature blackbody calibration source. The calibration scheme

provides a calibration accuracy of less than 1 % in window regions and up to 2 % within absorption bands. A validation of this calibration uncertainty estimate is performed by investigation of calibration self-consistency, which yields compatible results within the estimated errors for 91 % of the 2500 to 7800 cm^{-1} -range. A second validation effort consists in a comparison of a set of calibrated spectra to radiative transfer model calculations, which are consistent within the estimated errors for 98 % of the spectral range.

The continuum results in the far infrared, namely in the 400 to 580 cm^{-1} spectral range, are consistent with the widely used MT_CKD 2.5.2 (Mlawer et al., 2012) continuum model and with the findings of other recent atmospheric closure studies. Throughout most of the spectral range covered by the near-infrared section of the closure study, the results presented in this work constitute the first quantification of the water vapor continuum absorption under atmospheric conditions. The dry atmospheric conditions at the Zugspitze site enable continuum quantification even within water vapor absorption bands, while only upper limits for continuum absorption can be provided in the centers of window regions. Throughout 75 % of the 2500 to 7800 cm^{-1} spectral range, the Zugspitze results are agree within our estimated uncertainty with the MT_CKD 2.5.2-model. Notable exceptions are the 2800 to 3000 cm^{-1} and 4100 to 4200 cm^{-1} spectral ranges, where our measurements indicate about 5 times stronger continuum absorption than MT_CKD. The measurements are consistent with the laboratory measurements of Mondelain et al. (2015), which rely on cavity ring-down spectroscopy (CDRS), and the calorimetric-interferometric measurements of Bicknell et al. (2006). Compared to the recent FTIR laboratory studies of Ptashnik et al. (2012, 2013), our measurements indicate 2–5 times weaker continuum absorption under atmospheric conditions in the wings of water vapor absorption bands, namely in the 3200 to 3400 cm^{-1} , 4050 to 4200 cm^{-1} , and 6950 to 7050 cm^{-1} spectral regions.

The results obtained in this work constitute a significant contribution to the characterization of the water vapor continuum under atmospheric conditions and thereby add to decrease the water vapor-related uncertainties in atmospheric radiative transfer calculations. Given that previously no results under atmospheric conditions were available in the near-infrared, the findings of this work are a valuable tool for the validation of the commonly used MT_CKD continuum model and allow resolving the inconsistencies between recent laboratory studies in this spectral range. Additionally, the experimental setup established in this work provides the foundation to address further key questions considering the water vapor continuum in the future. The findings of recent studies on the climate relevance of the water vapor continuum (Paynter and Ramaswamy, 2014; Rädel et al., 2015) imply that the results presented in this thesis are expected to have a significant impact on climate models. The likely effects comprise an adjustment of the surface energy budget through a decrease in both latent and sensible heat and, as a consequence, a reduction of tropical convection and rainfall.

Contents

I	Introduction	1
II	Scientific Background and Motivation	7
1	Atmospheric Radiative Processes of Water Vapor	9
1.1	Role of Water Vapor in Atmospheric Radiative Transfer	9
1.2	Radiative Quantities and Fundamental Concepts	12
1.3	Definition of the Water Vapor Continuum	14
1.4	Water Vapor Continuum Theory	15
1.5	Climate Relevance of the Water Vapor Continuum	16
2	Water Vapor Continuum Quantification	19
2.1	Previous Water Vapor Continuum Measurements	19
2.2	Open Questions and Scope of this Work	21
III	Methods	23
3	Concept of Radiative Closure Experiments	25
4	Techniques for Infrared Spectral Radiance Measurements	29
4.1	Solar FTIR	29
4.2	Thermal Emission Interferometry	32
5	Correction of Pointing Errors in Solar Absorption Spectrometry	35
5.1	Significance of Pointing Errors in Solar FTIR Measurements	35
5.2	Basic Idea for a Mispointing Correction Method	36

5.3	Implementation of the Mispointing Correction	38
5.4	Example Correction for the Zugspitze FTIR	45
6	Radiometric Calibration of NIR Solar Absorption Spectra	51
6.1	Instrumental Setup	51
6.2	Langley Calibration	52
6.3	Blackbody Calibration	58
6.4	Combined Calibration Method	59
6.5	Calibration Uncertainty	59
7	Implementation of the Zugspitze Radiative Closure Experiment	63
7.1	Idea and Setup	63
7.2	Spectral Radiance Measurements	64
7.3	State Measurements	67
7.4	Radiative Transfer Calculations	73
7.5	Uncertainty Analysis of Radiance Residuals	74
8	Continuum Quantification from Radiative Closure Measurements	83
8.1	Assessment of FIR Continuum	83
8.2	NIR Continuum Determination	86
IV	Results	91
9	Pointing Error Correction Results	93
9.1	Results and Validation via Methane Trend Analysis	93
9.2	Verification of Zugspitze Corrections via Comparison to Garmisch Methane Soundings	97
10	Solar FTIR Radiometric Calibration Results	99
10.1	Calibration Curve	99
10.2	Validation of Results	100
11	Water Vapor Continuum Results	105
11.1	FIR Continuum	105

11.2 NIR Continuum	107
V Summary and Outlook	115
Bibliography	121
List of Figures	133
List of Tables	135
List of Acronyms	137
Publications	141
Acknowledgments	145

Part I

Introduction

Water in solid, liquid, or gaseous form is a prerequisite for life on Earth. In the atmosphere, water plays a central role in most weather phenomena via the processes of evaporation, cloud formation and precipitation. The role of atmospheric water vapor, i.e. water in gaseous form, is less obvious but equally important: due to its molecular structure, water vapor is the most important contributor to the interaction between the gases of the atmosphere and both the solar radiation and the thermal radiation emitted by the Earth's surface. As a consequence, water vapor contributes about 60 % to the atmospheric greenhouse effect, i.e. the absorption of outgoing thermal radiation that leads to an increased temperature at the Earth's surface (e.g. Kiehl and Trenberth, 1997). The presence of atmospheric water vapor thereby constitutes a key ingredient for maintaining a surface temperature that is suitable for life on Earth.

In the context of anthropogenic climate change, water vapor has an equally fundamental importance, which is, however, often overlooked. On a global average, the Earth's surface temperature has increased by 0.85 [0.65 to 1.06] K in the period between 1880 and 2012. There is solid evidence that the main driver of this temperature increase are anthropogenic emissions of greenhouse gases such as carbon dioxide (CO_2) and methane (CH_4) (IPCC, 2013). For these trace gases, concentrations in the atmosphere exceed pre-industrial levels by about 40 % and 150 %, respectively. The anthropogenic emissions of water vapor are negligible compared to the natural water cycle, and therefore one would expect that water vapor is no main factor to be taken into account in the context of climate change induced by human activities. Consequently, other processes that obviously play central roles are given more attention in the public debate: the influence of increased emissions of greenhouse gases such as CO_2 or CH_4 as well as the human influence on microscopic atmospheric particles, so-called aerosols.

The relevance of atmospheric water vapor in the context of anthropogenic climate change results from feedback processes. A simplistic outline of the water vapor feedback is that with increasing temperatures due to anthropogenic greenhouse gas emissions, evaporation over the oceans increases, which then further strengthens the water vapor greenhouse effect. This simplistic model therefore suggests a positive water vapor feedback, i.e. an enhancement of global warming due to the feedback. More sophisticated model- and observation-based studies suggest that relative humidity remains approximately constant on average in a warming climate, which in fact results in increased absolute humidity and positive water vapor feedback. However, the exact magnitude of the feedback remains a topic of ongoing research (Held and Soden, 2000; IPCC, 2013).

A comprehensive understanding of climate change and the capacity to accurately predict future climate evolution in numeric models requires significant advances in a number of fields. Well-known key issues include e.g. the accurate treatment of cloud effects in the models (see e.g. Mayer, 2009) or the influence of aerosols. As outlined above, in addition to these well-known issues, relevant open questions also include a precise knowledge of water vapor-related effects. This comprises an accurate quantitative understanding of the interaction of atmospheric water vapor with solar and thermal radiation, since these interaction processes are the foundation of the climate relevance of water vapor.

The interaction of water molecules with infrared radiation can be assigned to several causative processes which lead to two distinct classes of spectral features: the first contribution

is due to absorption bands composed of spectral lines, which are present throughout the entire infrared spectral range. There is, however, an additional second contribution to the spectral signature of water vapor. This contribution, namely absorption that ranges over wide spectral intervals and varies only slowly with wavenumber, is commonly referred to as the water vapor continuum. While experimental evidence indicating the existence of the continuum was already found in the early 20th century (e.g. Brunt, 1932; Elsasser, 1938), the underlying physical processes responsible for continuum absorption remain a subject of ongoing research and scientific debate (see e.g. Shine et al., 2012).

In addition to the unclear causative processes, the magnitude and further characteristics of the water vapor continuum still lack accurate constraints by measurements for many spectral regions. Laboratory and atmospheric studies have helped to greatly improve quantitative knowledge of the continuum. Such studies, however, still suffer from a number of important limitations. As noted by Shine et al. (2012), laboratory experiments have to be performed at conditions not representative of the atmosphere. Most notably, they typically rely on higher temperatures and the extrapolation of laboratory results to atmospheric temperatures may result in significant inaccuracies. Atmospheric studies, in contrary, are complicated by the fact that “separation of true water vapour continuum signal from instrumental artefacts and other contributors is a serious challenge” (Shine et al., 2012).

Due to these limitations of previous studies, a number of key open questions concerning the water vapor continuum remain:

- What is the magnitude of the continuum in the near infrared (NIR) under atmospheric conditions?
- How reliable are the results on the far-infrared (FIR) continuum obtained via atmospheric measurements?
- Is the currently used temperature dependence of the continuum correct?

As outlined above, the inaccuracies in the quantitative description of water vapor radiative processes that may result from these open questions lead to significant uncertainties in atmospheric radiative transfer calculations employed e.g. in climate models and numerous remote sensing techniques. Recent studies have shown that a variation of the continuum strength within the current uncertainty range leads to significant changes in the surface energy budget and the hydrological cycle in climate models (Paynter and Ramaswamy, 2014; Rädel et al., 2015). This situation is made clear e.g. by Paynter and Ramaswamy (2011), who pointed out that “the continuum contributes notably to our lack of complete understanding of shortwave absorption”, which leads to the rather disconcerting conclusion to exert “caution in performing shortwave radiative transfer calculations, since the continuum could contribute up to a $\pm 2\%$ uncertainty in water vapor absorption”. An accurate quantification of the water vapor continuum throughout the entire infrared spectral range is therefore of vital importance.

The scope of this work is to improve the quantitative understanding of the water vapor continuum throughout the infrared spectral range and thereby reduce the uncertainties in atmospheric radiative transfer calculations. The study covers the range from 400 to 7800 cm^{-1} ,

i.e. 1.3 to 25.0 μm . In order to obtain continuum results under conditions representative of the atmosphere, this work relies on field measurements. In detail, this thesis describes a radiative closure experiment that enables continuum quantification based on a quantitative comparison of measurements of spectral radiance in the infrared to radiative transfer calculations. Due to a combination of several key aspects, this study is able to overcome some of the limitations of previous experiments: The measurements are carried out at the high-altitude Zugspitze observatory (47.42° N, 10.98° E, 2964 m a.s.l.), whose main advantages are very dry atmospheric conditions and an extensive permanent instrumentation that enables accurate measurements of both spectral radiance and relevant atmospheric state parameters. Furthermore, the measurements are set up as a long-term experiment, which leads to a more extensive measurement data set compared to previous campaign-based studies. Finally, a number of newly developed methods, such as a novel calibration scheme for the NIR spectral range, enable continuum quantification in spectral regions that were previously not accessible to atmospheric studies.

Following this introduction, the Part II of this thesis contains an introduction to the scientific background of the role of water vapor in atmospheric radiative processes and the water vapor continuum. In Part III, the existing and newly developed methods that are used in the radiative closure study are presented, while Part IV contains the corresponding results. Finally, Part V provides a summary of the findings and an outlook.

Part II

Scientific Background and Motivation

Chapter 1

Atmospheric Radiative Processes of Water Vapor

This chapter gives an introduction to the crucial influence of water vapor on the atmospheric radiation budget. For both main constituents of the atmospheric radiation balance, namely the downwelling solar and outgoing thermal radiation, water vapor plays a dominant role in the interaction between infrared radiation and the atmospheric trace gases. The main classes of spectral features caused by these interaction processes, line and continuum absorption, are outlined.

In addition to an overview of relevant fundamental concepts and variables in atmospheric radiative transfer, the current state of knowledge on the theoretical foundation of continuum absorption is discussed. The final section of this chapter highlights the climate relevance of the water vapor continuum.

1.1 Role of Water Vapor in Atmospheric Radiative Transfer

The Earth's atmospheric radiative balance is characterized by two main contributions: The largest energy input into the Earth system is due to shortwave downwelling solar radiation, which mainly entails contributions from the ultra-violet (UV) throughout the visible to the infrared spectral range. This input of energy into the Earth system is approximately balanced by the thermal outgoing longwave radiation, whose spectral maximum lies in the FIR. A schematic representation of the mean global energy balance including quantitative estimates of all relevant contributions is provided in Fig. 1.1 (adopted from Wild et al., 2013). Radiative forcing e.g. by anthropogenic greenhouse gas emissions can cause a temporary imbalance between these contributions, which leads to changes in the climate system. This adaption of the climate to the modified radiative balance is observable e.g. in the ongoing global warming observed since the beginning of the industrial era (e.g. IPCC, 2013).

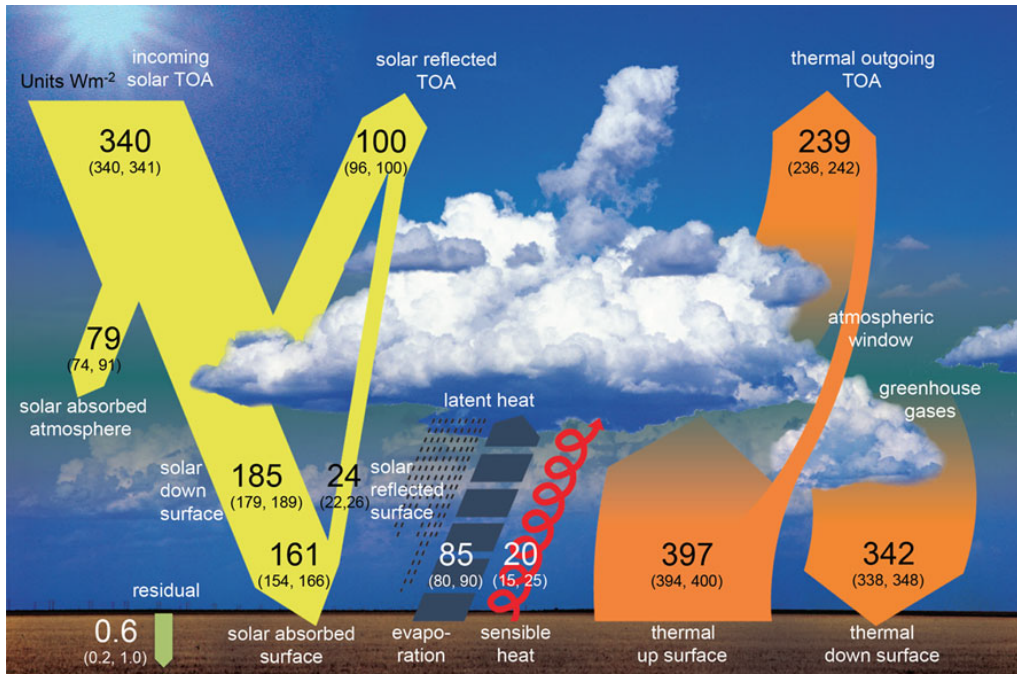


Figure 1.1: Schematic overview of the Earth's mean global energy balance. Units W m^{-2} . Figure adopted from Wild et al. (2013).

As depicted in Fig. 1.1, both longwave and shortwave contributions undergo interactions with different atmospheric constituents such as clouds, aerosols and atmospheric trace gases. Among other effects, this interaction causes the atmospheric greenhouse effect, i.e. the absorption of outgoing longwave radiation, which consequently leads to an increased temperature at the Earth's surface. The concept of the greenhouse effect was proposed by Fourier (1824), while Tyndall (1861) was able to demonstrate the attribution of this effect to absorption by gases such as water vapor or CO_2 via laboratory experiments and Arrhenius (1896) provided an extensive quantification of this effect. The greenhouse effect causes the mean surface temperature of the Earth to be about 14°C , while the mean temperature without the atmosphere would be about -19°C (see e.g. IPCC, 2007). As mentioned in the introduction, the atmospheric greenhouse effect is therefore a prerequisite for maintaining conditions suitable for life on Earth. Water vapor contributes about 60 % to the atmospheric greenhouse effect (e.g. Kiehl and Trenberth, 1997), while the remaining fraction is mostly due to CO_2 , CH_4 , nitrous oxide (N_2O) and ozone (O_3) in combination with minor contributions from other trace gases.

In general, considering the interaction between infrared radiation and the atmospheric trace gases, water vapor is the dominant contributor for both solar and thermal radiation (e.g. Harries et al., 2008). This role can be attributed mainly to two causes:

- Water vapor is relatively abundant in the atmosphere compared to other trace gases such as CO_2 . As an example, for a tropical standard atmosphere (Anderson et al., 1986), the mean number density of water vapor is about a factor of 20 higher than that of CO_2 .
- The structure of the water molecule leads to a high number of absorption bands ranging

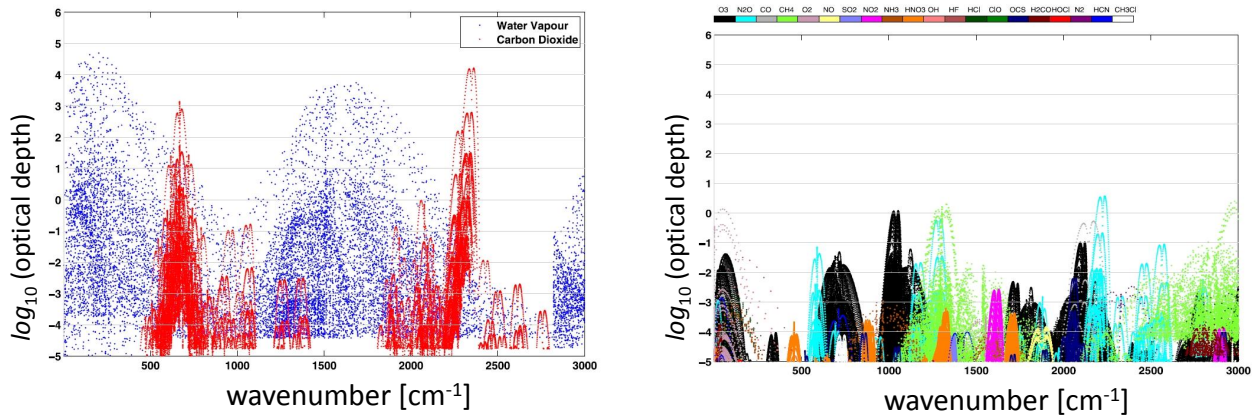


Figure 1.2: Optical depth of spectral lines throughout the infrared. Left: contributions by water vapor (blue) and CO₂ (red). Right: Contributions by further trace gases. Figure adopted from Harries et al., 2008.

throughout the entire infrared spectral range and beyond. Most notably, the permanent dipole moment of the water molecule causes the existence of a pure rotational absorption band, which is located in the spectral region of maximum thermal emission by the Earth's surface, the FIR. The existence of the pure rotational band is among the most important reasons for the dominant contribution of water vapor to the atmospheric greenhouse effect.

To illustrate this, Fig. 1.2 (adopted from Harries et al., 2008) shows model calculations of the optical depth of spectral lines of different trace gases for a standard atmosphere throughout the FIR and mid-infrared (MIR). These calculations clearly highlight the role of water vapor as the major contributor to molecular absorption and emission in the infrared and the role of CO₂ as the second biggest contributor.

As outlined in the introduction, even though direct anthropogenic water vapor emission is negligible, water vapor also plays an important role in the context of anthropogenic climate change via feedback processes. These processes result from the influence of anthropogenic climate change on the hydrological cycle, most importantly on the evaporation. Most studies agree on a positive water vapor feedback that is suggested by the simple assumption that higher temperatures result in increased evaporation and therefore increased water vapor greenhouse effect. The exact magnitude of the feedback, however, is a field of ongoing research. More extensive reviews on this topic can be found e.g. in Held and Soden (2000), Ramanathan and Inamdar (2006) or Harries et al. (2008).

The interaction of atmospheric water vapor with infrared radiation can be attributed to different processes which lead to two distinct classes of spectral features:

- i. Spectral lines, which in the infrared are due to purely rotational or vibrational-rotational transitions of the water molecules.
- ii. A second contribution which ranges over a broad spectral interval and varies only slowly with wavenumber, the so-called water vapor continuum.

A quantitative discussion of these contributions necessitates a basic framework of radiative quantities and formulae which will be introduced in the following section.

1.2 Radiative Quantities and Fundamental Concepts

This section contains a short overview of fundamental concepts and variables of atmospheric radiation. The content of this section was partly adapted from Liou (2002), which, alongside Zdunkowski et al. (2007), contains a more comprehensive review of this field.

Electromagnetic waves can be characterized by their wavelength λ . Throughout the remainder of this work, instead of λ , the wavenumber ν is generally used to specify spectral position:

$$\nu = \frac{1}{\lambda} \quad (1.1)$$

The following definition of the infrared spectral subdomains is adopted throughout the remainder of this work:

FIR: far infrared, $2 \text{ cm}^{-1} < \nu < 667 \text{ cm}^{-1}$

MIR: mid-infrared, $667 \text{ cm}^{-1} < \nu < 4000 \text{ cm}^{-1}$

NIR: near infrared, $4000 \text{ cm}^{-1} < \nu < 14000 \text{ cm}^{-1}$

The differential amount of radiant energy dE in a time interval dt , which crosses an element of area dA and is confined to the differential solid angle $d\Omega$ and the differential wavenumber interval $d\nu$, is defined as the spectral radiance $\mathbf{I}(\nu)$:

$$\mathbf{I}(\nu) = \frac{dE}{\cos\Theta dA d\Omega d\nu dt} , \quad (1.2)$$

where Θ designates the angle of incidence relative to the zenith direction.

The spectral irradiance $\mathbf{F}(\nu)$ can be calculated from $\mathbf{I}(\nu)$ via integration over the entire hemispheric solid angle:

$$\mathbf{F}(\nu) = \int_{\Omega} \mathbf{I}(\nu) \cos\Theta d\Omega \quad (1.3)$$

A fundamental concept for the description of thermal emission of electromagnetic radiation is the blackbody. The term “blackbody” is used for objects which completely absorb incident radiation. The radiance spectrum $\mathbf{B}(\lambda, T)$ of a blackbody has been established by Planck (1901):

$$\mathbf{B}(\lambda, T) = \frac{2hc^2}{\lambda^5} \frac{1}{\exp\left(\frac{hc}{\lambda k_b T}\right) - 1} , \quad (1.4)$$

where T designates the temperature of the blackbody, $h = 6.62612 \cdot 10^{-34} \text{ m}^2 \text{ kg s}^{-1}$ the Planck constant, $k_b = 1.38065 \cdot 10^{-23} \text{ m}^2 \text{ kg s}^{-2} \text{ K}^{-1}$ the Boltzmann constant and $c = 299792458 \text{ m s}^{-1}$ the speed of light.

Atmospheric radiative transfer is characterized by emission, absorption and scattering processes due to the interaction of electromagnetic radiation with atmospheric constituents. These interaction processes are described quantitatively by the radiative transfer equation (Chandrasekhar, 1950):

$$\begin{aligned} \frac{d\mathbf{I}(\nu)}{ds} = & -(\mathbf{K}_a(\nu) + \mathbf{K}_s(\nu))\mathbf{I}(\nu) \\ & + \mathbf{K}_a(\nu)\mathbf{B}(\nu, T) \\ & + \mathbf{K}_s(\nu) \int_{\pi}^0 \int_{2\pi}^0 \mathbf{I}^*(\nu, \Theta, \Phi) \frac{S(\Theta, \Phi)}{4\pi} d\Phi^* \sin\Theta^* d\Theta^* \end{aligned} \quad (1.5)$$

The first term of Eq. 1.5 describes attenuation of the incident radiation via absorption or scattering. The absorption coefficient \mathbf{K}_a and the scattering coefficient \mathbf{K}_s can be combined via the definition of the extinction coefficient \mathbf{K}_e :

$$\mathbf{K}_e = \mathbf{K}_a + \mathbf{K}_s \quad (1.6)$$

The second term of Eq. 1.5 corresponds to the emission of radiation by the medium, and relies on the blackbody spectrum of Eq. 1.4. The emission term can be expressed using the absorption coefficient \mathbf{K}_a since, according to Kirchhoff's law, the emissivity is equal to the absorptivity for any object in thermal equilibrium.

The third term describes scattering in beam direction and contains the scattering phase function $S(\Theta, \Phi)$. For the specific applications included in this thesis, namely thermal emission and direct solar absorption spectra, the scattering term can be neglected to a good approximation. This simplification of Eq. 1.5 omitting the scattering term is commonly referred to as the Schwarzschild equation.

If in addition to the scattering term the emission term can also be neglected, as in the case of solar absorption spectra, the solution of Eq. 1.5 corresponds to the Beer-Bouguer-Lambert law:

$$\mathbf{I}(\nu) = \mathbf{I}_0(\nu) \cdot e^{-\tau(\nu)}, \quad (1.7)$$

where $\mathbf{I}(\nu)$ designates the attenuated radiance, $\mathbf{I}_0(\nu)$ the incident radiance and $\tau(\nu)$ the optical depth (OD). The OD $\tau(\nu)$ is defined as

$$\tau(\nu) = \int_0^s \mathbf{K}_e(\nu, s') ds' = \int_0^s \mathbf{k}_e(\nu, s') n ds'. \quad (1.8)$$

For absorption due to atmospheric trace gases, \mathbf{k}_e is referred to as the molecular extinction coefficient, which is linked to \mathbf{K}_e via

$$\mathbf{K}_e = \mathbf{k}_e \cdot n, \quad (1.9)$$

where n designates the number density of the absorbing trace gas.

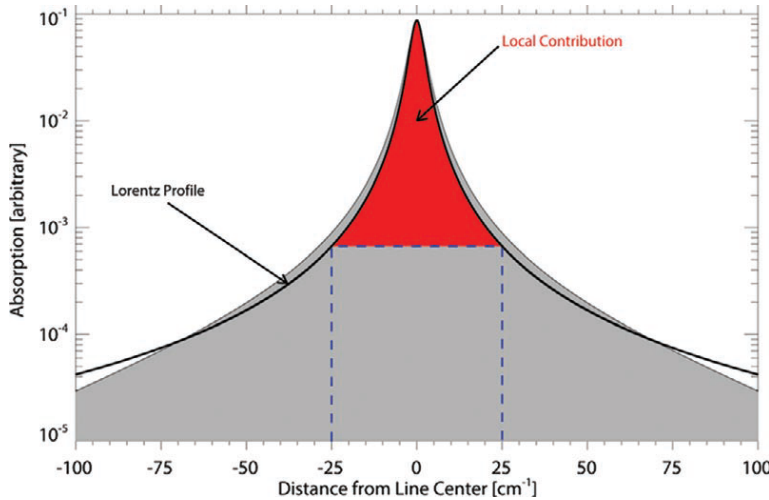


Figure 1.3: Standard definition of the water vapor continuum. All absorption due to water vapor that exceeds a Voight line shape within $\Delta\nu < \pm 25 \text{ cm}^{-1}$ from each water vapor line center minus the value of the Voight line shape at $\Delta\nu = \pm 25 \text{ cm}^{-1}$ is interpreted as continuum absorption (grey area). Figure adopted from Turner and Mlawer (2010).

1.3 Definition of the Water Vapor Continuum

As outlined in Sect. 1.1, the spectral signature caused by the interaction between water vapor and infrared radiation can be attributed to the contributions from spectral lines and the water vapor continuum. Water vapor continuum is commonly defined as all absorption due to water vapor that exceeds a Voight line shape within $\Delta\nu < \pm 25 \text{ cm}^{-1}$ from each water vapor line center minus the value of the Voight line shape at $\Delta\nu = \pm 25 \text{ cm}^{-1}$ (see Fig. 1.3). In other words, the continuum comprises:

- i. all water vapor absorption beyond $\Delta\nu = \pm 25 \text{ cm}^{-1}$,
- ii. deviations from the Voight line shape within $\Delta\nu < \pm 25 \text{ cm}^{-1}$, and finally
- iii. the “pedestal” within $\Delta\nu < \pm 25 \text{ cm}^{-1}$ that has the value of the Voight line at $\Delta\nu = 25 \text{ cm}^{-1}$.

The overall continuum is then computed as the sum of the contributions (i)–(iii) from all water vapor lines. Note that this definition of the continuum also leads to the fact that a quantitative description of the continuum is always associated to a set of line parameter values, i.e. when comparing continuum results one has to take care to use a common line parameter data base.

The water vapor continuum can be further decomposed in self- and foreign-broadened continuum contributions according to

$$k_{\text{cont}} = c_s \frac{\rho_{\text{H}_2\text{O}}}{\rho_0} + c_f \frac{\rho_{\text{air}}}{\rho_0}, \quad (1.10)$$

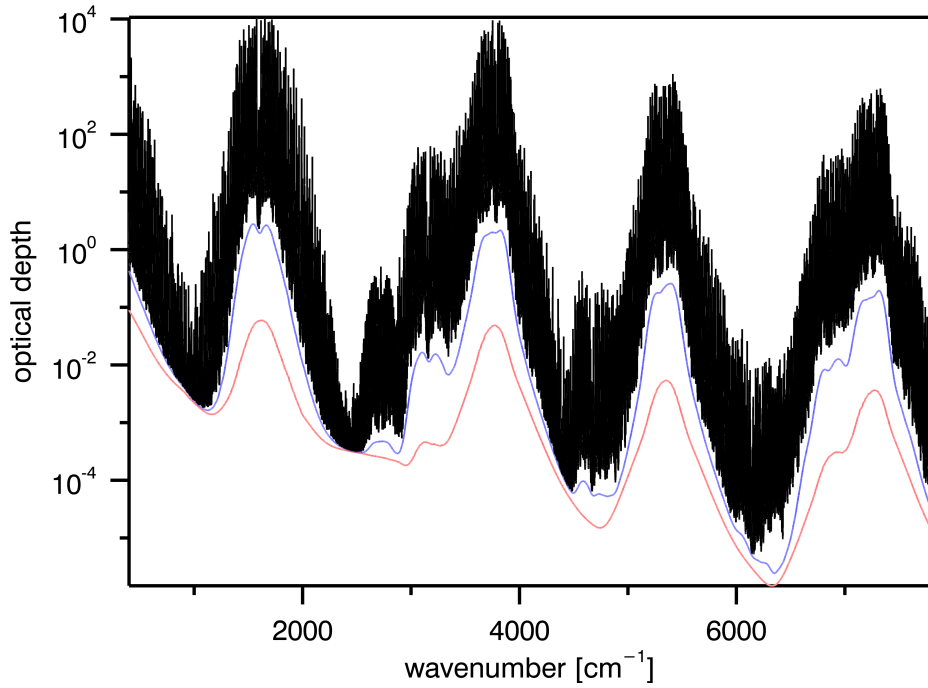


Figure 1.4: Water vapor OD for a mid-latitude winter standard atmosphere according to the MT_CKD 2.5.2-continuum model (Mlawer et al., 2012). Red: self continuum OD. Blue: total continuum OD (self+foreign). Black: Water vapor OD (continuum+spectral lines)

where \mathbf{k}_{cont} designates the continuum absorption coefficient. \mathbf{c}_s and \mathbf{c}_f are commonly referred to as the self and foreign continuum coefficients and $\rho_{\text{H}_2\text{O}}$, ρ_{air} , and ρ_0 are the densities of water vapor, dry air and a reference density, respectively. In detail, $\rho_0 = P_0/(k_b T_0)$, where $P_0 = 1013 \text{ mbar}$, k_b is the Boltzmann constant, and $T_0 = 296 \text{ K}$. Self and foreign continuum are characterized by their scaling of continuum OD with water vapor density: While the self continuum OD scales with the square of the water vapor density, the foreign continuum features only linear scaling. These contributions are visible in Fig. 1.4, which shows calculations of the water vapor optical depth and its contributions from continuum and spectral lines in the 400 to 7800 cm^{-1} spectral range which is covered by the analysis in this work. The representation corresponds to a mid-latitude winter standard atmosphere as defined in Anderson et al. (1986) and the widely used MT_CKD 2.5.2-continuum model (Mlawer et al., 2012).

1.4 Water Vapor Continuum Theory

The physical description of the mechanisms responsible for the water vapor continuum is a topic of ongoing research. Although no definite continuum theory does exist yet, a consensus has been reached on the existence of two physical processes contributing, namely

- i. monomer contributions resulting from perturbations of the water vapor line shape due to

- (self and foreign) pair-interactions during molecular collisions and
- ii. dimer contributions, i.e. absorption due to stable and/or metastable bound structures of two water vapor molecules.

The line shape hypothesis (i) states that the line shape of water vapor monomer transitions deviates from a Voight shape, most notably in the far wings of the line. Line shape theories based on a quantum mechanical approach that are able to reproduce the observed continuum were presented e.g. by Tipping and Ma (1995) and motivated the line-shape based continuum models CKD and MT_CKD. Evidence for the existence of water dimers in the atmosphere has been reported by Pfeilsticker et al. (2003) and Ptashnik (2008). The most compelling evidence for the dimer theory is that a negative exponential temperature dependence is observed for the self continuum. Such a temperature dependence is expected for dimer contributions since the number density of dimers decreases with increasing temperature.

However, the relative importance of the monomer and dimer contributions as a function of temperature and wavenumber (especially for window versus in-band regions) are far from being understood. For recent reviews see Shine et al. (2012, 2016); Mlawer et al. (2012), and references therein. The most widely used water vapor continuum model at this time (MT_CKD 2.5.2) is based on the monomer hypothesis, while contributions from water dimers shall be implemented in future versions (Mlawer et al., 2012). MT_CKD is a semi-empirical model combining a collision-induced component and a line shape component. In both terms empirical parameters are set in a way to achieve agreement with laboratory and field measurements. Constraining measurements have hitherto been restricted to measurements within the microwave, the FIR, the MIR and, recently, also the NIR, see Mlawer et al. (2012) for details and references. This means that considerable fractions of the full $0\text{--}20000\text{ cm}^{-1}$ range of MT_CKD are semi-empirical extrapolations in between the constraining measurements, i.e. continuum parameters reported there are not validated by measurements.

1.5 Climate Relevance of the Water Vapor Continuum

The water vapor continuum contributes up to 4 % to the reduction of outgoing longwave radiation by the atmosphere, i.e. it increases the water vapor greenhouse effect in the FIR and MIR compared to only line emission (Paynter and Ramaswamy, 2011). In the shortwave, water vapor continuum leads to an increase of absorption of solar radiation. Depending on the atmospheric state and the choice of continuum model, up to 6 % of the clear-sky water vapor absorption can be attributed to the continuum (Paynter and Ramaswamy, 2011). These significant contributions to the Earth's radiative energy balance implicate that the water vapor continuum has a major relevance for climate.

A number of recent studies have investigated the effects of the uncertainty in our knowledge of the continuum on current climate models. As an example, Turner et al. (2012a) showed that modifications to the previously derived strength of the FIR water vapor continuum in the $10\text{--}700\text{ cm}^{-1}$ region within the Community Earth System Model (CESM) had a statistically

significant impact on both the radiation and dynamics with changes in the vertical structure of temperature, humidity, and cloud amount, all of which impacted the diabatic heating profile.

In the NIR, Paynter and Ramaswamy (2012) showed that adjustments in the water vapor continuum according to recent laboratory studies could result in 1.1 W m^{-2} to 3.2 W m^{-2} additional clear-sky absorption of solar radiation on a global average. According to Paynter and Ramaswamy (2014), this sizable range is due to fairly large measurement uncertainties in the shortwave near-infrared window regions (Ptashnik et al., 2004, 2011, 2012, 2013; Paynter et al., 2007, 2009; Baranov and Lafferty, 2011, 2012; Mondelain et al., 2013). After inclusion of a modified parameterization for the shortwave water vapor continuum (BPS-MTCKD 2.0) to the Geophysical Fluid Dynamics Laboratory (GFDL) global model, Paynter and Ramaswamy (2014) find the surface energy budget adjusted predominantly through a decrease in both surface latent and sensible heat. This leads to a decrease in tropical convection and to a subsequent 1% reduction in tropical rainfall. Finally, the recent NIR continuum study of Rädel et al. (2015) investigated the impact of switching from the CKD continuum model frequently used in climate models to a continuum model where absorption is enhanced at wavelengths greater than $1 \mu\text{m}$ based on recent measurements (CAVIAR). They found that for CKD and CAVIAR respectively, and relative to the no-continuum case, the solar component of the water vapor feedback is enhanced by about 4 and 9%, the change in clear-sky downward surface irradiance is 7 and 18% more negative, and the global-mean precipitation response decreases by 1 and 4%.

The above examples clearly illustrate that an accurate quantitative knowledge of the water vapor continuum is of crucial importance for reducing the uncertainties of current climate models. Consequently, a series of experiments has been conducted to improve quantitative knowledge of the water vapor continuum, including the study presented in this work. These studies will be discussed in the following chapter.

Chapter 2

Water Vapor Continuum Quantification

This chapter introduces the aim of this work, namely quantitative measurements of the water vapor continuum. A review of previous measurement efforts covers laboratory and atmospheric studies relying on different experimental techniques. This overview makes clear that substantial open questions remain in the field of continuum quantification.

Unresolved key issues include the quantification of the NIR continuum under atmospheric conditions, which enables to resolve the unexplained discrepancies between recent laboratory studies relying on different measurement techniques. Further issues also include the improvement of continuum constraints in the FIR and MIR and a better understanding of the continuum temperature dependence. The scope of this work, which is based on these open questions, is presented at the end of this chapter.

2.1 Previous Water Vapor Continuum Measurements

As outlined in the previous section, the water vapor continuum contributes significantly to the interaction of infrared radiation with the atmosphere which leads to its important influence on climate. Accurate quantitative knowledge of the continuum is therefore a prerequisite for realistic atmospheric radiative transfer calculations, for instance in climate models. Consequently, numerous efforts have been made to improve continuum quantification. More extensive reviews of continuum quantification efforts are given e.g. by Shine et al. (2012, 2016) and the content of this section is partly adapted from these references.

A first approach to continuum quantification is via laboratory experiments relying on gas cells filled with pure water vapor or moist air. Such experiments typically rely on a broadband infrared light source and multi-pass gas cells. By subsequently measuring spectra with empty and filled cell, the optical depth of the gas contained in the multi-pass cell can be determined. Given a precise quantitative knowledge of water vapor line absorption, this contribution can be subtracted to obtain a quantitative estimate of the continuum absorption.

Early evidence for continuum absorption, i.e. broadband absorption that could not be explained by water vapor absorption lines was found by Brunt (1932) and Elsasser (1938) in the MIR window region. The initial quantitative foundation of current continuum models was provided by the measurements of Burch (1982, 1985) and Burch and Alt (1984). These studies relied on cell measurements in combination with a grating spectrometer and provided continuum quantification over a broad spectral and temperature range. Based on these studies, the CKD continuum model (Clough et al., 1989) was constrained quantitatively.

Subsequent studies relied primarily on FTIR (Fourier transform infrared) spectrometers (see Sect. 4.1) to improve the sensitivity of the continuum measurements. Measurements of both contributions to the continuum, the self and foreign continuum were achieved with this method (e.g. Baranov et al., 2008, 2011; Paynter et al., 2009, Ptashnik et al., 2011). While early experiments were performed with heated cells, recently, continuum quantification with FTIR spectrometry was also achieved at room temperature (e.g. Ptashnik et al., 2012, 2013).

An alternative experimental technique, which enables even more sensitive continuum measurements compared to FTIR spectroscopy is cavity ring-down spectroscopy (CRDS) and the related optical feedback cavity enhanced spectroscopy (OF-CEAS). Until now, a number of spectral regions of the MIR have been subject of such measurements (e.g. Cormier et al., 2002, 2005), while further studies covered portions of the NIR (Mondelain et al., 2013, 2014, 2015; Ventrillard et al., 2015). In principle, improvements to the experiments relying on this technique may enable continuum quantification also at atmospheric temperatures in the future. Further alternative techniques include the calorimetric-interferometric measurements by Fulghum and Tilleman (1991) and Bicknell et al. (2006).

At present, however, laboratory studies relying on different experimental techniques have yielded inconsistent results on the strength of both self and foreign continuum. Most notably, the FTIR measurements indicate the continuum absorption in the window regions to be up to two orders of magnitude stronger compared to the CRDS-based studies. As noted e.g. by Mondelain et al. (2014) and Ptashnik et al. (2013), the individual results feature differences far beyond the respective uncertainty estimates and an attribution of these differences to causative processes remains tentative. Due to the decrease of water vapor saturation pressure with decreasing temperature and given the sensitivity of currently available experimental setups, laboratory studies generally have been performed at least at room temperature or even heated to be able to measure the weak continuum absorption. Therefore, a further challenge for laboratory studies is that they are normally not feasible at representative atmospheric conditions, i.e. at atmospheric temperatures. To date, the temperature dependence of the self continuum still lacks secure observational constraints (e.g. Paynter and Ramaswamy, 2011). This makes application of the laboratory results on atmospheric radiative transfer calculations non-straightforward.

A second class of continuum quantification studies relies on atmospheric radiative closure experiments. This method is outlined in detail in Chapter 3. Atmospheric measurements are challenging and typically less sensitive than laboratory studies due to additional sources of uncertainty that ensue from imprecise knowledge of the atmospheric state at the time of the spectral radiance measurements. However, atmospheric studies are able to overcome

some of the main limitations of laboratory measurements since they enable measurements at low temperature. Such field closure studies comprise high-spectral-resolution radiance measurements and radiative transfer simulations of the measured spectra driven by coincident atmospheric state measurements of integrated water vapor (IWV) and other relevant parameters. As part of the U.S. Atmospheric Radiation Measurement (ARM) program (Ackerman and Stokes, 2003), a series of radiative closure experiments have been set up (e.g. Turner et al., 2004, 2012b) which was complemented by the Italian ECOWAR (Earth Cooling by Water Vapor Radiation) project (e.g. Bhawar et al., 2008; Bianchini et al., 2011). A number of experiments have addressed the water vapor continuum in the FIR (Tobin et al., 1999; Serio et al., 2008; Delamere et al., 2010; Liuzzi et al., 2014) and the MIR (Turner et al., 2004; Rowe et al., 2006; Rowe and Walden, 2009; Newman et al., 2012). A crucial requirement for radiative closure experiments in the FIR and MIR is to select a site guaranteeing a wide range of IWV levels including the occurrence of very low IWV levels. Dry atmospheric states ($\text{IWV} < 1 \text{ mm}$) are highly beneficial to attain information on absorption coefficients in otherwise saturated spectral regions (e.g. the pure rotational water band of water vapor). For these reasons, dedicated campaigns have been performed in dry regions on the globe, e.g. at the Sheba ice station (Tobin et al., 1999) or the RHUBC II campaign in the Atacama desert (Turner and Mlawer, 2010). The results of Tobin et al. (1999) were used to constrain the initial version of the widely used MT_CKD continuum model (Mlawer et al., 2012).

In the NIR spectral region, no atmospheric radiative closure experiments have been reported in the literature with the exception of the study by Sierk et al. (2004), which however only covered the spectral region $\nu > 10000 \text{ cm}^{-1}$. A hindrance for quantitative field studies may have been the fact that absorption in the NIR due to aerosols can become comparable to the magnitude of the water vapor continuum absorption of interest (Ptashnik et al., 2015). The possibility to accurately separate these two components depends on aerosol load (i.e. aerosol optical depth, AOD) and therefore on field site characteristics. A detailed outline of this crucial challenge will be given when introducing the new Zugspitze field experiment (including NIR measurements) in Chapter 7.

2.2 Open Questions and Scope of this Work

The previous section made clear that substantial effort has been made in constraining the water vapor continuum quantitatively via different experimental techniques. However, a number of key questions in this field remain unsolved and thereby lead to significant uncertainties in atmospheric radiative transfer calculations, e.g. in climate models.

In the FIR, continuum measurements are based on a very limited number of studies. A validation of previous efforts is therefore highly desirable. Throughout most of the NIR, currently no measurements of the water vapor continuum under atmospheric conditions are available. The use of laboratory results obtained at higher temperatures is furthermore hindered by a lack of secure constraints on the continuum temperature dependence. The situation in the NIR is further complicated by the fact that currently, laboratory studies employing different experimental techniques have yielded mutually inconsistent results on the strength of

the continuum absorption at room temperature.

A general shortcoming of atmospheric closure studies for continuum quantification is that they measure only overall continuum absorption. A separation of the measured absorption in contributions by the self and foreign continuum has not been achieved until now without relying on further assumptions such as a prescribed self-to-foreign-continuum ratio. The same holds true for the temperature dependence of the continuum, which is of vital importance for the application of continuum results to atmospheric radiative transfer calculations but has to date not been accurately quantified in atmospheric measurements.

The goal of this work is to contribute to the solution of these key open questions: Using a radiative closure study with thermal emission spectra, a validation of previous continuum quantification efforts in the FIR is implemented. Solar absorption spectra will be used to achieve a first quantification of the water vapor continuum under atmospheric conditions in the NIR and thereby resolve the inconsistencies between current laboratory studies. A key issue that has previously hindered such studies, the lack of sufficiently accurate radiometric calibration for solar FTIR instruments in the NIR, will be addressed using a novel radiometric calibration approach.

The closure measurements set up at the Zugspitze are designed as a long-term closure study that will provide an extensive data set covering a wide range of atmospheric temperature and IWV. Such a data set provides the foundation to investigate the continuum temperature dependence. Furthermore, self and foreign continuum contributions can be separated by their different dependence on water vapor density (see Sect. 1.1). Therefore, while these issues will not be a subject of this work due to the limited amount of measurement data currently available from the closure setup, the experiment implemented within the scope of this work will provide the necessary foundation to resolve these key questions in the future.

Part III

Methods

Chapter 3

Concept of Radiative Closure Experiments

This chapter introduces the technique of radiative closure experiments, which is used for continuum quantification in this work. In general, the concept of closure experiments consists in the determination of geophysical parameters via multiple different measurements or simulation techniques. A quantitative comparison of the results obtained with the different methods then allows for the evaluation of the accuracy of one or more of the techniques used. This work relies on a so-called radiative closure, while further typical applications of the closure method include e.g. the characterization of aerosol properties (see e.g. Quinn and Coffman, 1998).

In the case of radiative closure studies, the basic concept outlined above is implemented via a quantitative comparison of spectral radiance measurements with synthetic spectra generated using a radiative transfer model. The differences between measured and calculated spectra, which are commonly referred to as spectral residuals, give insight on whether the spectroscopic parameters assumed in the model calculations were correct or have to be modified. Spectroscopic parameters can then be adjusted in order to minimize the spectral residuals, resulting in a set of more accurate parameters. A logical scheme of this method is presented in Fig. 3.1. The sensitivity of the closure experiment, i.e. the accuracy of the derived parameters, depends on the uncertainty of the spectral residuals. It is therefore of crucial importance to accurately characterize all uncertainties associated with the measured or simulated spectra used in the closure.

While numerous spectroscopic parameters can be assessed with radiative closure studies, this work focusses on the quantification of the water vapor continuum as outlined in Chapter 2. Measurements of spectral radiance are carried out with several instruments to cover different spectral domains: while the solar FTIR technique is used for measuring solar absorption spectra in the NIR (Fig. 3.1, top right), thermal emission spectra in the FIR and MIR are measured with the ER-AERI instrument (Fig. 3.1, top left). A review of the basic techniques used for spectral radiance measurements in this work is provided in Chapter 4. Radiance spectra have to be radiometrically calibrated to be used in the closure analysis. Chapter 6 introduces a novel calibration method that allows to achieve sufficiently accurate calibration for water vapor

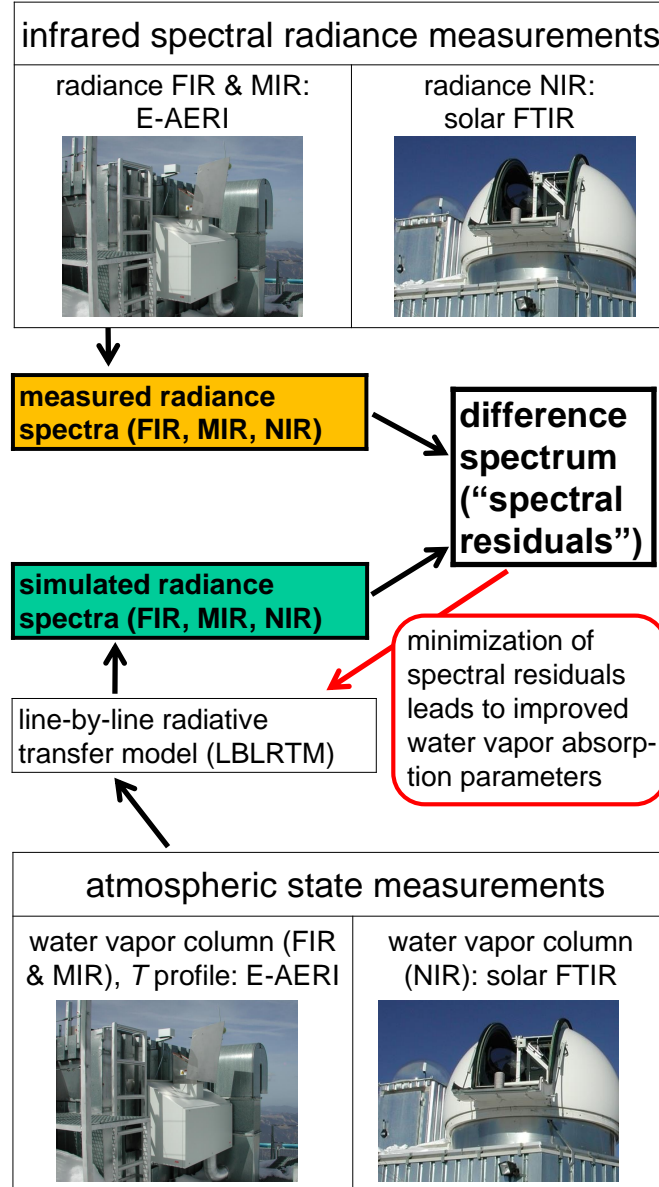


Figure 3.1: Logical scheme of the Zugspitze radiative closure experiment. Simulated radiance spectra are based on atmospheric state measurements performed coincidentally to the radiance measurements. The closure idea is to minimize spectral residuals between simulated and measured radiance spectra by iteratively adjusting/improving the water vapor absorption parameters used in the FIR, MIR, and NIR spectral radiance simulations.

continuum quantification based on NIR solar absorption spectra. Note that in addition to the NIR, the solar FTIR measurements and the corresponding water vapor continuum results also cover a fraction of the MIR spectral domain, namely 2800–4000 cm^{−1}. However, in the interest of brevity, this part of the closure study will be labeled “NIR closure” in the following.

Synthetic spectra are generated by means of a radiative transfer model, in the case of this study the LBLRTM model (Clough et al., 2005). As an input to the model calculations, a number of parameters describing the atmospheric state at the time and location of the spectral radiance measurements have to be specified. This entails the pressure and temperature profiles, as well as information on the profiles or total columns of a number of atmospheric trace gases. While water vapor column constitutes the most important input parameter in this study, water vapor profile shape, CO₂, CH₄, O₃, and N₂O total column also have to be specified. For the trace gas species with only column specifications, the profile shape is assumed to be consistent with the mid-latitude winter standard atmosphere (Anderson et al., 1986). Further atmospheric state input relevant for NIR measurements comprises AOD.

The accuracy of the radiometric calibration in the NIR and of several trace gas column measurements used in the analysis is further improved by a method that enables the correction of pointing errors in solar absorption spectrometry. This method will be presented in Chapter 5. A detailed description of the implementation of the closure method at the Zugspitze observatory and the sensitivity of the setup will be given in Chapter 7. Finally, the analysis steps required to achieve water vapor continuum quantification from the measurements will be described in Chapter 8.

Chapter 4

Techniques for Infrared Spectral Radiance Measurements

Radiative closure experiments rely on measurements of the spectral radiance. In the case of this work, the measurements comprise solar absorption spectra in the NIR and thermal emission spectra in the FIR and MIR. This chapter gives a short introduction to the techniques employed for those measurements.

The solar FTIR technique is used for the NIR measurements. The FIR/MIR measurements rely on thermal emission interferometry, which is based on the same basic measurement principle as the solar FTIR. However, due to the different spectral domain, significant differences to the solar FTIR exist especially for the radiometric calibration of measured spectra, which are also outlined in this chapter.

4.1 Solar FTIR

The closure measurements presented in this work rely on solar absorption spectra for continuum quantification in the NIR spectral range. The spectral radiance measurements in the NIR were carried out using the solar FTIR (Fourier transform infrared) technique. The Solar FTIR technique furthermore enables highly accurate measurements of integrated column amounts or low-resolution vertical profiles of atmospheric trace gases. These measurements serve as an input to the closure experiment for CO₂, CH₄, and N₂O columns as well as for the water vapor column in the NIR closure. This section contains a short introduction to the basic principles and characteristics of the solar FTIR method. A comprehensive review of the FTIR technique can be found e.g. in Griffiths and De Haseth (2007).

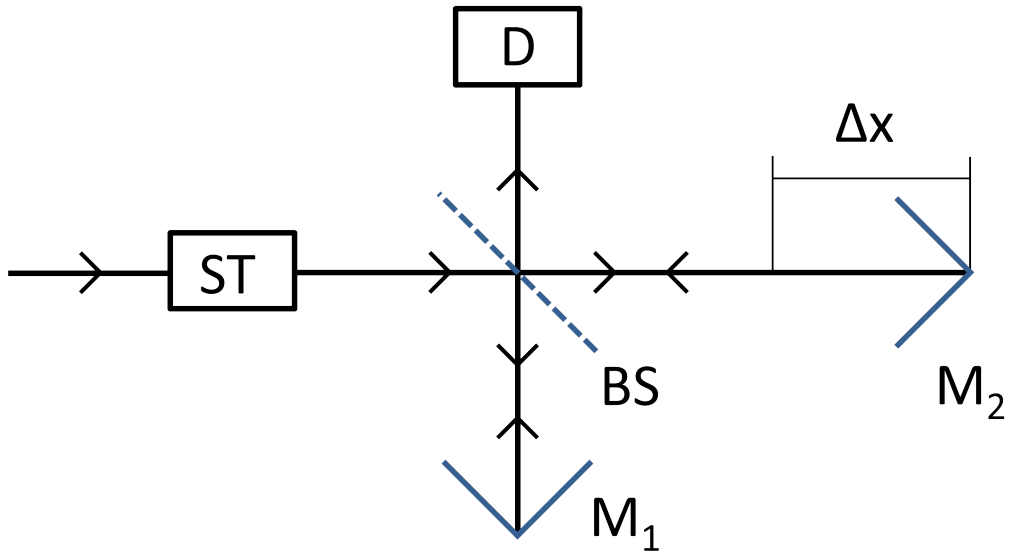


Figure 4.1: Schematic overview of the Michelson interferometer used in the solar FTIR technique. Solar radiation is directed into the spectrometer by the solar tracker (ST). Perpendicular beams from the semi-transparent beam splitter (BS) are reflected at the cube-corner mirrors M₁ and M₂. The resulting interference signal which depends on the optical path difference Δx is measured at the detector D.

Solar FTIR instruments are based on a Michelson-type interferometer, which enables very high spectral resolution measurements of infrared spectral radiance. The basic layout of the instrument is depicted schematically in Fig. 4.1. In order to direct the solar radiation to the spectrometer, a solar tracking unit (ST) is employed. A detailed discussion of the solar tracker used at the Zugspitze FTIR, which is shown in Fig. 6.1, can be found in Sect. 5.4. Different solar tracker designs as well as their respective advantages are discussed in Sect. 5.1.

Within the spectrometer, the incoming solar radiation is separated into two perpendicular beams by a semi-transparent beam splitter (BS). While one beam is reflected back to the beam splitter by a fixed mirror M₁, the other one is reflected at a second mirror M₂, which can be moved parallel to the beam direction. The distance from the beam splitter to M₂ differs from the distance to M₁ by Δx , which is commonly referred to as the optical path difference (OPD). Current solar FTIR instruments typically rely on cube-corner mirrors at the positions M₁ and M₂ instead of the plane mirrors used in the original Michelson interferometer design. This modification enables the compensation of mirror tilt for M₁ and M₂, which is among the major limitations of standard Michelson interferometers.

Both reflected beams interfere at the beam splitter and the resulting interference signal is recorded at the detector D. In detail, the measured quantity is referred to as the interferogram $\mathbf{I}(\Delta x)$, i.e. the signal \mathbf{I} measured at the detector depending on the OPD Δx . The detector system consists of a focusing device and a semiconductor detector. A variety of detector materials is available for different applications, namely for measurements in different spectral regions. The choice of detector type for the measurements used in this work is discussed in

Sect. 6.1. The OPD Δx has to be known with very high accuracy for further analysis of the interferogram. This sampling is achieved by means of measuring the interference signal of a laser with known wavelength (typically a helium-neon laser), which is aligned with the solar beam.

The solar radiance spectrum $\mathbf{I}(\nu)$ can be deduced from the interferogram $\mathbf{I}(\Delta x)$ and vice versa via a Fourier transform:

$$\begin{aligned}\mathbf{I}(\Delta x) &= \int_{-\infty}^{\infty} \mathbf{I}(\nu) \cos(2\pi\nu\Delta x) d\nu \\ \Leftrightarrow \mathbf{I}(\nu) &= \int_{-\infty}^{\infty} \mathbf{I}(\Delta x) \cos(2\pi\nu\Delta x) d\Delta x\end{aligned}\quad (4.1)$$

Equation 4.1 implies that the full information content of the radiance spectrum can only be reconstructed via the Fourier transform if the interferogram is measured with an infinite maximum OPD. Since this is not feasible in real instruments, the spectrum determined from an interferogram with finite maximum optical path difference OPD_{\max} is not identical to the incident solar absorption spectrum. The effect on the measurement can be described by a multiplication of the interferogram with an apodization function $\mathbf{A}(\Delta x)$, and the resulting impact on the spectrum is described by a convolution of the spectrum with the Fourier transform of the apodization function. A finite OPD_{\max} can be expressed by the following apodization function:

$$\mathbf{A}(\Delta x) = \begin{cases} 1 & \text{if } \Delta x \leq \text{OPD}_{\max} \\ 0 & \text{if } \Delta x > \text{OPD}_{\max} \end{cases} \quad (4.2)$$

This apodization corresponds to a convolution of the solar spectrum with a sinc function ($\sin(\nu)/\nu$). A spectral line of infinitesimal width (which, of course, does not exist in reality) is thereby broadened to a sinc line shape in the measured spectrum. This results in the commonly used definition of the spectral resolution $\Delta\nu$ of an FTIR:

$$\Delta\nu = \frac{1}{2 \cdot \text{OPD}_{\max}} \quad (4.3)$$

Other effects such as non-ideal alignment of the moveable mirror M_2 or further optical elements in the spectrometer correspond to additional apodization and lead to further modifications of the measured spectrum. The effect of this sum of apodization contributions on the measured spectrum can be combined in the so-called instrumental line shape (ILS). The ILS is convoluted with an ideal spectrum to describe all instrumental effects on the measurement.

The FTIR technique has a number of key advantages over alternative instrument designs such as prism or grating spectrometers. Firstly, the so-called multiplex or Fellgett's advantage states that FTIR instruments are capable of measuring all spectral elements simultaneously, thereby improving the signal-to-noise ratio of a measurement of a given duration by a factor of \sqrt{M} compared to other techniques, where M designates the number of resolved spectral elements. A second crucial advantage, named Jacquinot or throughput advantage, is that the FTIR method does allow for a higher solid angle in the collimated beam passing through the instrument. This is due to the fact that the FTIR instruments do not rely on slits in the

optical path, and results in an improvement of the signal-to-noise ratio of about a factor 200 compared to grating spectrometers.

For further analysis in a closure experiment, solar FTIR spectra have to be radiometrically calibrated. This work introduces a novel calibration approach that relies on a combination of the Langley technique and measurements of a high-temperature blackbody source, which will be presented in Chapter 6. This approach enables sufficient calibration accuracy to quantify water vapor continuum absorption from the Zugspitze measurements in the NIR.

4.2 Thermal Emission Interferometry

Thermal atmospheric emission in the FIR and MIR can be measured using FTIR spectroscopy in an analogous way to solar radiation. However, due to the different spectral domain, specific challenges arise when using the FTIR technique for thermal emission spectrometry. These challenges are exemplary outlined here based on the AERI instrument (Atmospheric Emitted Radiance Interferometer, Knuteson et al., 2004a, 2004b), which measures downwelling thermal radiance in the FIR and MIR. An extended range AERI (ER-AERI) is part of the instrumentation available at the Zugspitze summit observatory and is shown in Fig. 3.1 (top left).

The most significant difference to the NIR that ensues for measurements of thermal atmospheric emission in the FIR and MIR is the radiometric calibration of observed spectra. In the NIR, thermal emission by the instrument is negligible compared to the downwelling solar radiance as discussed in Sect. 6.5. In the FIR and MIR, however, the radiance of the atmospheric scene may be of the same order of magnitude than the emission from the instrument, since atmospheric temperature in the lowermost layers is close to the ambient (and instrument) temperature. This impedes accurate calibration via the technique presented in Chapter 6. The AERI therefore makes use of the calibration technique that has been developed by Revercomb et al. (1988). This calibration scheme relies on two blackbody calibration sources at different cavity temperatures, namely at ambient temperature and 60 °C.

The calibration approach of Revercomb et al. (1988) relies on an alternative representation of Eq. 4.1, namely the use of a complex Fourier transform for the calculation of spectra from interferograms:

$$\mathbf{I}(\Delta x) = \frac{1}{2} \int_{-\infty}^{\infty} \mathbf{I}(\nu) \exp^{i\Phi(\nu)} \exp^{i2\pi\nu\Delta x} d\nu \quad (4.4)$$

In addition to the magnitude of the spectrum $\mathbf{I}(\nu)$ used in Eq. 4.1, Eq. 4.4 furthermore introduces a phase $\Phi(\nu)$. The phase $\Phi(\nu)$ is used e.g. to describe the effect of interferograms whose central maximum does not exactly coincide with $\text{OPD} = 0$ and which therefore are not consistent with Eq. 4.1.

Following Revercomb et al. (1988) and Knuteson et al. (2004b), the calibrated AERI radiance spectrum can be determined using the equation given below. Note that the notation introduced by Revercomb et al. (1988) and Knuteson et al. (2004b) is used, which is not identical to the naming of variables used throughout the remainder of this work.

$$\mathbf{L}_\nu = \text{Re} \left[\frac{\mathbf{C}_\nu - \mathbf{C}_{c\nu}}{\mathbf{C}_{h\nu} - \mathbf{C}_{c\nu}} \right] [\mathbf{B}_\nu(T_h) - \mathbf{B}_\nu(T_c)] + \mathbf{B}_\nu(T_c) , \quad (4.5)$$

where \mathbf{L}_ν designates the calibrated spectral radiance. The further parameters \mathbf{C}_ν , $\mathbf{C}_{h\nu}$ and $\mathbf{C}_{c\nu}$ correspond to the complex spectra obtained from the atmospheric scene and the hot and ambient blackbodies using Eq. 4.4. Finally, $\mathbf{B}_\nu(T_h)$ and $\mathbf{B}_\nu(T_c)$ designate the theoretical spectra of the hot and ambient blackbodies at temperatures T_h and T_c .

Equation 4.5 differs from the straightforward expression for a two-point blackbody calibration in the fact that the ratio of differences of the full complex spectra is used instead of only relying on the magnitudes of the spectra. Via this modification, the calibration procedure achieves that both complex phase and offset contributions do not bias the radiative calibration.

According to Knuteson et al. (2004b), the AERI blackbody radiance spectra are given by

$$\begin{aligned} \mathbf{B}_\nu(T_h) &= \mathbf{e}_\nu^h \mathbf{B}_\nu(T_h) + (1 - \mathbf{e}_\nu^h) \mathbf{B}_\nu(T_r) \\ \mathbf{B}_\nu(T_c) &= \mathbf{e}_\nu^c \mathbf{B}_\nu(T_c) + (1 - \mathbf{e}_\nu^c) \mathbf{B}_\nu(T_r) , \end{aligned} \quad (4.6)$$

where $\mathbf{B}_\nu(T_r)$ corresponds to the theoretical blackbody radiance given by the Planck function at the temperature T_r as defined in Eq. 1.4. The temperature T_r is set to the radiative temperature of the instrument parts that can emit into the blackbody cavity. For the AERI measurements this temperature is assumed to be the temperature of the blackbody support structure. The parameters \mathbf{e}_ν^h and \mathbf{e}_ν^c designate the emissivities of the calibration sources. Equation 4.6 therefore corresponds to a correction of the theoretical blackbody radiance spectra to account for deviations of the blackbody emissivity from 1.

Chapter 5

Correction of Pointing Errors in Solar Absorption Spectrometry

Solar FTIR measurements rely on a tracking system that maintains the alignment of the instrument's line of sight with the center of the solar disc. However, the sun tracking is generally prone to small inaccuracies. This mispointing leads to errors in trace gas column amounts or profiles determined from the solar FTIR spectra. Pointing errors furthermore influence the accuracy of the radiometric calibration of solar FTIR spectra that will be presented in Chapter 6.

This chapter describes a novel method that allows quantification of pointing inaccuracies in solar FTIR measurements. Mispointing information is deduced from the Doppler shift of solar spectral lines in the measured spectra. A combination of multiple measurements of solar line shifts at different times allows to constrain the absolute value and direction of the mispointing. This technique is relevant for water vapor continuum quantification, since it enables the correction of the mispointing effects on trace gas column measurements and the radiometric calibration mentioned above. The mispointing correction thereby improves the sensitivity of the closure experiment and enables a more accurate quantification of the weak continuum absorption. The content of this chapter has been partly adapted from the related publication by Reichert et al. (2015).

5.1 Significance of Pointing Errors in Solar FTIR Measurements

Solar FTIR spectrometry is one of the key measurement techniques for highly accurate ground-based vertical soundings of atmospheric trace gases. In the context of this work, solar FTIR measurements are used to constrain total column amounts of a number of atmospheric trace gases (water vapor, CO₂, CH₄, and N₂O). In addition, the solar FTIR technique is employed for the spectral radiance measurements in the NIR (see Sect. 7.2) and for the radiometric calibration of these spectra (Chapter 6).

Since solar absorption spectrometers are using the sun as light source, all such instruments contain a device for active tracking of the solar position. The simplest approach to achieve continuous sun tracking is to adjust the observed sky position according to precalculated values. However, such passive tracking does not fulfill typical accuracy requirements. Therefore, most current solar FTIR systems make use of feedback from a quadrant diode to control the solar tracker position and thereby achieve improved pointing accuracy (see e.g. Adrian et al., 1994; Notholt et al., 1995; Washenfelder et al., 2006). Further improvements can be made by using feedback from a camera image of the position of the solar disc on the spectrometer's entrance aperture instead of a quadrant diode (Gisi et al., 2011).

However, the continuous alignment of the instrument's line of sight with the center of the solar disc is generally prone to inaccuracies. Tracking errors in vertical direction cause the airmass observed by the spectrometer to differ from the air mass assumed in trace gas retrievals (Hase, 2000). To a good approximation, this airmass error results in an equal relative error in the retrieved trace gas columns. Additionally, mispointing may result in further errors in retrieved column amounts, such as instrumental line shape variations if field stops inside the spectrometer are not fully illuminated.

As outlined in Hase (2000), a mispointing of 0.1° in zenith direction results in about 1% trace gas column error for an apparent solar zenith angle (sza) of 80° . These errors exceed current accuracy requirements for measured column amounts, e.g. the 0.5% accuracy requested for the TCCON network (Toon et al., 2009). In the context of this work, mispointing furthermore influences the accuracy of the NIR radiometric calibration as will be discussed in Sect. 6.5. It is therefore an issue to determine and correct for the influence of mispointing in solar FTIR measurements.

Information on the mispointing is contained in solar lines which appear in ground-based solar spectra in addition to the terrestrial absorption features. Mispointing perpendicular to the solar rotation axis causes rotational Doppler shifts in the solar lines. Measurements of the solar line shift therefore enable the determination of mispointing perpendicular to the solar rotation axis (Gisi et al., 2011). However, these measurements do not permit complete determination of the mispointing direction and norm since they do not contain information on the mispointing component parallel to the solar rotation axis. This is the basic reason why there is currently no method available that enables a correction of mispointing-induced retrieval errors. In this work, a method to overcome this limitation and thereby enable a posteriori-correction of mispointing effects is presented, to our knowledge for the first time.

The following sections entail a description of the mispointing problem and the basic idea to its correction (Sect. 5.2), a detailed description of the implementation of this method (Sect. 5.3), and the application of the correction procedure to the Zugspitze measurements (Sect. 5.4).

5.2 Basic Idea for a Mispointing Correction Method

For all sun-tracking spectrometers, the alignment of the instrument's line-of-sight with the sky position of the solar disc center is prone to inaccuracies. The zenith direction component of

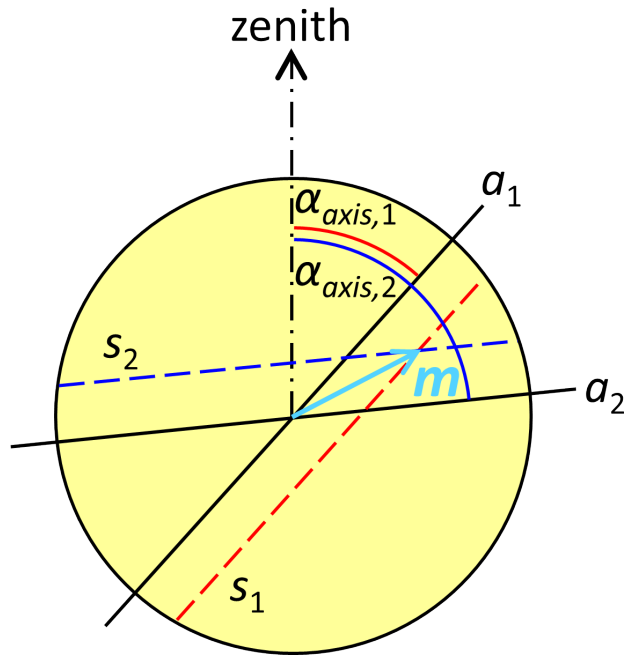


Figure 5.1: Schematics of the mispointing determination strategy. Solar line shifts are measured at times t_1, t_2 with corresponding solar axis orientations $\alpha_{\text{axis}, 1}$ and $\alpha_{\text{axis}, 2}$. The mispointing vector \mathbf{m} is defined by the intersection of the lines s_1 and s_2 parallel to the solar rotation axes a_1 and a_2 , respectively. Differential solar rotation is neglected in this figure.

this mispointing causes the airmass assumed in trace gas column retrievals to differ from the real airmass during the measurement. This error in airmass results in an equally large relative error in the retrieved trace gas column.

As outlined in the previous section, only the mispointing perpendicular to the solar rotation axis but not the component parallel to the axis can be deduced from the Doppler shift of solar lines. Therefore, the component of mispointing in zenith direction that causes bias in the retrieved trace gas columns cannot be deduced directly from such measurements.

However, the orientation of the solar axis relative to the zenith direction varies over time. If the change of the mispointing between two measurements is negligible compared to the magnitude of the mispointing, the changing axis orientation enables the determination of zenith and horizontal component of mispointing. The mispointing can therefore be fully constrained from a set of shift measurements at times t_1, t_2 with different axis orientations $\alpha_{\text{axis}, 1}$ and $\alpha_{\text{axis}, 2}$ (Fig. 5.1). In the following, the vector from the center of the solar disc to the actual pointing coordinates is designated as mispointing vector \mathbf{m} .

Neglecting differential solar rotation (which is addressed in Sect. 5.3), i.e. assuming constant angular velocity at all solar latitudes, a single shift measurement constrains the mispointing to lie on the straight line s parallel to the solar rotation axis a . The distance between s and a is proportional to the measured solar line shift $\Delta\nu/\nu$. Combining two measurements with different axis orientations $\alpha_{\text{axis}, 1}$ and $\alpha_{\text{axis}, 2}$, the mispointing vector \mathbf{m} is then defined by the intersection coordinates of the corresponding straight lines s_1 and s_2 , respectively. In order

to reduce errors due to inaccurate solar line shift measurements, it is favorable to combine larger sets of measured spectra to compute a mean mispointing vector instead of using only two measurements. In this case, the mean mispointing is defined by the mean intersection coordinates of all pairs of measurements that can be selected from a given set of spectra. Note that this approach relies on the assumption that changes of the mispointing within the set of spectra used to compute one mean value of \mathbf{m} are negligible compared to the magnitude of the mispointing itself.

5.3 Implementation of the Mispointing Correction

Substeps of the Correction Scheme

In the following, the steps required to implement the mispointing determination approach are described in detail. As a first step, the time series of measured spectra is divided in time bins. We outlined in the previous section that the mispointing determination method relies on the assumption of approximately constant mispointing within each of the time bins. Therefore, the suitable choice of time bins results in a trade-off between low statistical errors in mispointing results achieved by a large bin size and improved fulfillment of the underlying assumption of constant mispointing within each time bin that results from a smaller bin size. An example for the bin size adjustment in the case of the Zugspitze measurements is discussed in Sect. 5.4.

For all measured spectra, the solar line Doppler shift $\Delta\nu/\nu$ has to be determined. In our analysis, this task is performed using the PROFFIT software (Hase et al., 2004). The fit is performed on spectra measured with the optical bandpass filter used for CH_4 column retrievals, which covers the wavenumber range $2400 < \nu < 3100 \text{ cm}^{-1}$. In order to assess the accuracy of the solar line shift fit, these results are compared to solar line shift measurements in the adjacent $2000 < \nu < 2650 \text{ cm}^{-1}$ filter. The differences between the measured line shifts in both filters were set as an estimate of the shift measurement uncertainty. This uncertainty is subsequently used for the calculation of the mispointing uncertainty (see Sect. 5.3).

In addition to solar line shifts, the mispointing calculation requires knowledge of the orientation α_{axis} of the solar rotation axis relative to the zenith direction for each measured spectrum. More precisely, the orientation angle used in the mispointing calculation is the apparent angle from zenith direction to sun rotation axis direction at the time and location of the measurements, i.e. the angle between projections of zenith direction and sun rotation axis direction on a plane perpendicular to spectrometer's line of sight. All necessary steps for calculation of α_{axis} are outlined in Sect. 5.3.

Systematic mispointing is assumed to be caused by deviations of the sun tracker optics geometry from an idealized setup. Possible scenarios include e.g. inaccuracies in mirror orientation or misalignment of the quadrant diode that allows continuous adjustment of the instrument's line of sight to follow the sun position. For such sources of tracking error, it is plausible to assume constant mispointing during limited time intervals in a coordinate system valid in the spectrometer, contrary to e.g. the azimuth/elevation coordinate system in the sky. Due to the sun tracker optics, the image of the sun undergoes reflections and rotations when

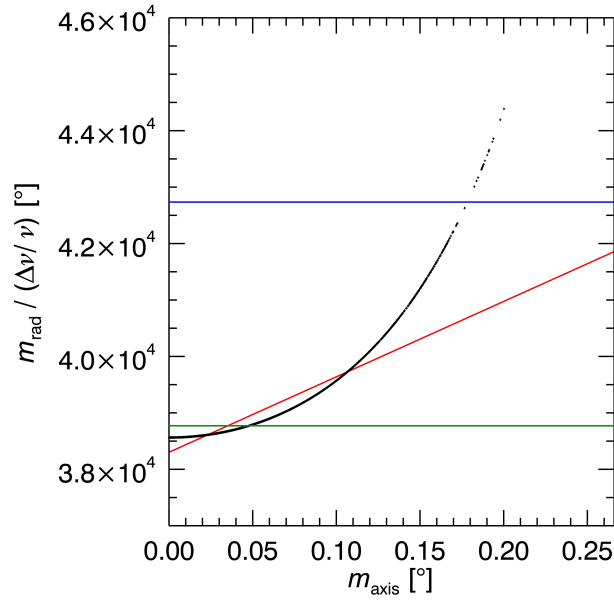


Figure 5.2: Conversion of solar shift to radial mispointing. m_{axis} designates the apparent distance from the solar equator. Blue: mean conversion factor given in Gisi et al. (2011). Green: iteratively determined mean conversion for the Zugspitze dataset according to Eq. 5.3. Black: conversion according to Eq. 5.2, using $\omega(\varphi)$ values calculated with Eq. 5.1, m_{axis} calculated using Eq. 5.3. Red: best fit linear conversion according to Eq. 5.4.

transferred to the spectrometer entrance aperture. Therefore, the resulting image of the sun on the entrance aperture has to be calculated for each measurement.

The transformation of the solar image due to the solar tracker optics can be described by a concatenation of 3×3 imaging matrices resulting in an overall transfer matrix \mathbf{T} . The orientation of the sun rotation axis on the entrance aperture is then calculated by multiplying a vector with orientation α_{axis} with the correct transfer matrix \mathbf{T} . For the retransformation of a mispointing vector \mathbf{m} derived in spectrometer coordinates to sky coordinates \mathbf{m}_{sky} , \mathbf{m} has to be multiplied with the inverse of the transfer matrix, that is $\mathbf{m}_{\text{sky}} = \mathbf{T}^{-1}\mathbf{m}$.

Contrary to the simplified solution scheme presented in Sect. 5.2, the angular velocity of solar rotation depends on solar latitude φ , a phenomenon called differential solar rotation. The latitude-dependent angular velocity of solar rotation $\omega(\varphi)$ is described approximately by the following relation:

$$\omega(\varphi) = c_1 + c_2 \sin^2 \varphi + c_3 \sin^4 \varphi \quad (5.1)$$

Currently accepted values for the constants c_1 , c_2 , and c_3 are: $c_1 = 14.713 \pm 0.0491 \text{ d}^{-1}$, $c_2 = -2.396 \pm 0.188 \text{ d}^{-1}$, $c_3 = -1.787 \pm 0.253 \text{ d}^{-1}$ (Snodgrass and Ulrich, 1990). Due to differential solar rotation, a single solar line shift measurement does not constrain the mispointing to lie on a straight line as depicted in Fig. 5.1, but on a line with constant velocity component along the observer's line of sight. The radial mispointing in degree perpendicular

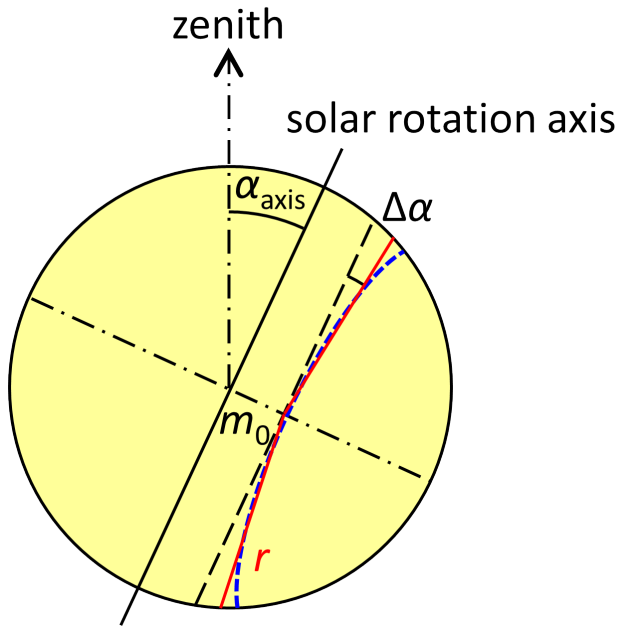


Figure 5.3: Linear approximation of differential rotation. A solar line shift measurement constrains the mispointing to lie on a line with constant velocity component along the observer's line of sight (blue line). Linear approximation of this relation results in a constraint of mispointing on rays r tilted away from the solar rotation axis by an angle $\Delta\alpha$ and with a minimum distance m_0 to the axis (red line).

to the solar rotation axis m_{rad} can be calculated from solar line shift measurements:

$$m_{\text{rad}} = [\Delta\nu/\nu \cdot c/\omega(\varphi)] \cdot r_{\text{sun, apparent}}/r_{\text{sun}} , \quad (5.2)$$

where $c = 2.99792458 \cdot 10^8 \text{ m s}^{-1}$, $r_{\text{sun}} = 6.958 \cdot 10^8 \text{ m}$, $r_{\text{sun, apparent}} = 0.266^\circ$.

In this study, instead of using Eq. 5.2 for mispointing calculation, a linear approximation to this relation is performed (see Fig. 5.2). Mispointing results determined from Zugspitze measurements suggest this approximation induces no significant additional error in the results. While the mean relative error of mispointing over the Zugspitze measurement time series is 9.5 %, the error of radial mispointing induced by the linear approximation is 0.36 %, which is negligible compared to the mispointing error.

The following steps are performed to obtain the linear approximation:

- A mean factor for conversion of solar shifts into mispointing is determined iteratively from our dataset. To obtain the conversion factor, the distributions of mispointing values parallel and perpendicular to the solar equator are assumed to be similar. Using the shift-mispointing conversion given in Gisi et al. (2011), a typical distribution of mispointing values parallel to the solar rotation axis is then calculated from the solar line shift measurements. By means of Eq. 5.1, this mispointing distribution can be converted to a typical angular velocity distribution for the given dataset. The mean value of this $\omega(\varphi)$ distribution is then used to calculate an improved shift-mispointing conversion

factor replacing $\omega(\varphi)$ in Eq. 5.2 by the mean value of the angular velocity distribution. The above steps are repeated iteratively until convergence is reached. This results in an adjusted shift-mispointing conversion of

$$m_{\text{rad, mean}} = \Delta\nu/\nu \cdot 38\,771.4^\circ. \quad (5.3)$$

- ii. The distribution of mispointing parallel to the equator m_{rad} can now be calculated using Eq. 5.3. The distribution of mispointing parallel to the sun rotation axis m_{axis} is assumed to be similar to the distribution of m_{rad} . A solar latitude distribution for our data set can now be derived using $\varphi = \arcsin(m_{\text{axis}}/r_{\text{sun, apparent}})$. This enables calculating $\omega(\varphi)$ by means of Eq. 5.1.
- iii. A linear fit to the mispointing values calculated using Eq. 5.2 and the angular velocity values determined in step (ii) is then performed. The final result for the best fit linear approximation is

$$m_{\text{rad, lin}} = \Delta\nu/\nu \cdot (a + b \cdot m_{\text{axis}}), \quad (5.4)$$

where $a = 38\,301.9 \pm 2.9^\circ$ and $b = 13\,363 \pm 63$.

Equation 5.4 implies that a solar shift measurement constrains the mispointing to lie on a pair of rays r with a distance to the solar rotation axis on the solar equator of $m_0 = \Delta\nu/\nu \cdot a$, and at an angle relative to the zenith direction of $\alpha_{\text{corr}} = \alpha_{\text{axis}} \pm \Delta\alpha$, where $\Delta\alpha = \arctan(\Delta\nu/\nu \cdot b)$, as shown in Fig. 5.3.

Given the orientation of the solar axis (see Sect. 5.3) and the conversion of solar line shift to mispointing, mispointing results can now be calculated. As described at the beginning of this section, the measurement time series is distributed in time bins. For each bin, all possible combinations of measurement pairs are considered. For each of the $n(n - 1)/2$ possible pairs selected from the n measurements within a time bin, a mispointing vector \mathbf{m} is calculated. Finally, the mean of the mispointing over each time bin is calculated as the error-weighted mean of all \mathbf{m} . The computation of the weighted means requires an estimate of the uncertainty of intersection coordinates. The uncertainty estimate was deduced from the difference of coincident solar shift measurements in adjacent optical filters. A detailed description of this uncertainty estimate is given in Sect. 5.3.

Corrected trace gas column amounts can be calculated from the mispointing results with two distinct correction methods: the a posteriori correction method consists in subtracting the mispointing in zenith direction $m_{y, \text{sky}}$ from the apparent sza taken from the trace gas retrieval ray trace calculation. Corrected airmass values can then be calculated according to

$$\text{airmass}_{\text{corr}} = 1 / \cos(\text{sza} - m_{y, \text{sky}}). \quad (5.5)$$

Retrieved trace gas columns are then multiplied with airmass/airmass_{corr} to obtain corrected columns.

The second (a priori) correction method takes into account that in addition to the effect on the conversion of slant path to vertical column, the mispointing has slight influence on the forward spectral calculations performed in the retrieval. The a priori method therefore uses

the mispointing-corrected sza as an input to the retrieval. The retrieval is then repeated with the corrected input values resulting in corrected trace gas column results.

Note that Eq. 5.5 given in the a posteriori method only permits an approximate airmass calculation. In order to achieve higher accuracy especially at high sza, a more sophisticated calculation such as the approach described by Kasten and Young (1989) can be chosen. Furthermore, the a priori scheme includes additional effects such as the influence of mispointing on the ray trace calculation in trace gas retrievals which are not considered in the a posteriori method. However, as will be shown in Sect. 9.1, the corrected trace gas columns obtained using the a posteriori approach show good consistency with the results from the more sophisticated a priori approach.

Orientation of Solar Rotation Axis

This section contains an outline of the calculation of α_{axis} , which is defined as the angle between projections of zenith direction and sun rotation axis on a plane perpendicular to the spectrometer's line of sight. For a sun-viewing instrument, this projection plane corresponds to the plane defined by the day/night separation line on the Earth. The orientation angle α_{axis} consists of three distinct projections onto the day/night separation plane: the first contribution β is the angle between the Earth rotation axis and the zenith direction, the second angle γ spans from the ecliptic axis to the Earth rotation axis. The final contribution δ describes the angle between the sun rotation axis and the ecliptic axis. In total, α_{axis} is calculated as:

$$\alpha_{\text{axis}} = \beta + \gamma - \delta \quad (5.6)$$

The calculation of the component β , ranging from the projections on the day/night separation plane of zenith direction to the Earth rotation axis is represented in Fig. 5.4a. The angle β has a daily cycle due to the Earth's rotation. The amplitude β_{max} of this daily cycle shows a seasonal variability due to variations in the inclination ε of the Earth axis relative to the day/night separation plane. The inclination ε can be calculated as

$$\varepsilon = \arcsin(\sin(\varepsilon_{\text{max}}) \cdot \sin(\Upsilon E)) , \quad (5.7)$$

where ΥE designates the heliocentric ecliptic longitude of the Earth and $\varepsilon_{\text{max}} = 23.43^\circ$. This leads to an amplitude of the daily cycle given by

$$\beta_{\text{max}} = \arctan(\tan(90^\circ - \text{observer latitude}) / \cos \varepsilon) . \quad (5.8)$$

The angle β can then be expressed in terms of β_{max} and observation time

$$\beta = -\arctan(\tan(\beta_{\text{max}}) \cdot \sin(\text{day fraction} \cdot 2\pi)) , \quad (5.9)$$

where day fraction = hours since local noon / 24 h.

The second orientation component γ is the angle between the Earth rotation axis and the ecliptic axis and has a seasonal cycle due to the inclination of the Earth axis. As shown in

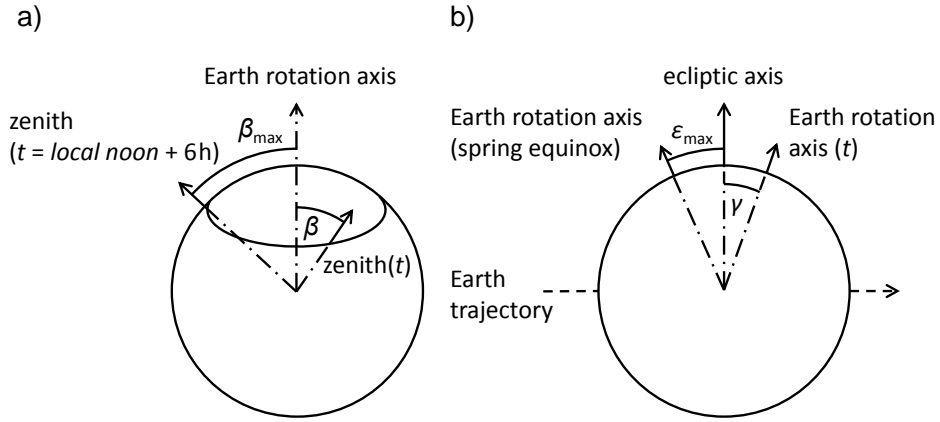


Figure 5.4: Calculation of sun axis orientation relative to zenith direction. (a) β : zenith direction relative to Earth rotation axis. (b) γ : Earth rotation axis relative to ecliptic axis. Both subfigures represent projections on the day/night separation plane, direction of view towards the sun.

Fig. 5.4b, the amplitude of this seasonal variability is equal to the inclination of the Earth axis relative to the ecliptic axis. Consequently, γ can be calculated as

$$\gamma = -\arctan(\tan(\varepsilon_{\max}) \cdot \cos(\gamma E)) . \quad (5.10)$$

The calculation of the third angle component δ , between sun rotation axis and ecliptic axis, is outlined in Giles (2000). In summary,

$$\delta = \arctan(-\cos(\eta - \Omega) \cdot \tan i) , \quad (5.11)$$

where standard values for the constants i and Ω are $i = 7.25^\circ$, $\Omega = 73.67^\circ + 0.013958^\circ (t \text{ [years]} - 1850.0)$, and $\eta = \gamma E + 180^\circ$.

Uncertainty Estimate of Intersection Coordinates

In order to obtain an estimate of the intersection coordinate uncertainty, the following approach was adopted: an estimate of solar line shift uncertainty can be gained from the difference of coincident solar shift measurements in the adjacent $2400 < \nu < 3100 \text{ cm}^{-1}$ and $2000 < \nu < 2650 \text{ cm}^{-1}$ filters. A 15-min coincidence interval was chosen for this calculation. The mean shift difference throughout the April 2006 to March 2015 interval considered in our study was $3.3 \cdot 10^{-7}$. Compared to the mean magnitude of solar line shifts of $9.9 \cdot 10^{-7}$, this corresponds to a mean relative difference of $\sim 33\%$.

Instead of infinitesimal-width rays as depicted in Fig. 5.3, the rays r_1 and r_2 are assumed to have a width corresponding to the measured solar shift difference. The ray widths Δr_1 and Δr_2 depend on the measured solar line shifts Δs_1 and Δs_2 , respectively. Furthermore, due to differential solar rotation, the conversion from shift differences to ray widths depends

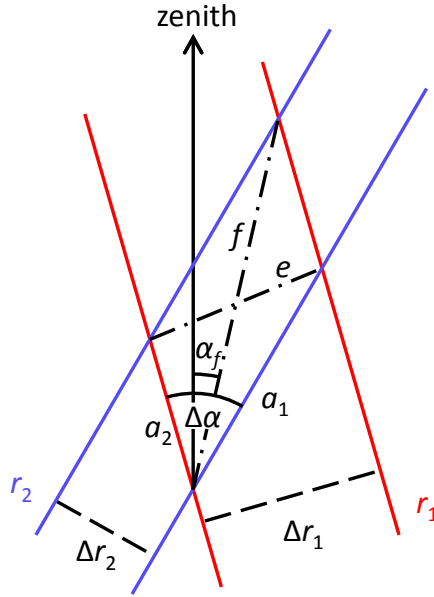


Figure 5.5: Calculation of mispointing uncertainty.

on the intersection coordinates. The conversion is given by the quotient of the mispointing perpendicular to the solar axis $m_{\text{rad, lin}}$ according to Eq. 5.4 and the measured solar shift s :

$$\Delta r = \Delta s \cdot (m_{\text{rad, lin}}/s) \quad (5.12)$$

Due to the finite ray widths Δr_1 and Δr_2 , an overlap parallelogram (see Fig. 5.5) emerges instead of an intersection point. The length of the diagonals of the parallelogram (e, f) can be calculated as follows:

$$\begin{aligned} \Delta\alpha &= \alpha_{\text{corr, 2}} - \alpha_{\text{corr, 1}} \\ a_1 &= |\Delta r_1 / \sin(\Delta\alpha)|, a_2 = |\Delta r_2 / \sin(\Delta\alpha)| \\ e^2 &= a_1^2 + a_2^2 - 2a_1 a_2 \cos(\Delta\alpha) \\ f^2 &= a_1^2 + a_2^2 - 2a_1 a_2 \cos(180^\circ - \Delta\alpha) . \end{aligned} \quad (5.13)$$

Finally, the x and y components of the uncertainty estimate, i.e. $\Delta x, \Delta y$, are given by the projection of the overlap parallelogram on the x and y axes, respectively. Note that the y axis is defined to be equivalent to the zenith direction.

$$\begin{aligned} \alpha_f &= \arccos(a_2^2 - a_1^2 - f^2 / (-2a_1 f)) + \alpha_{\text{corr, 2}} \\ \Delta x_e &= \cos(\alpha_f) \cdot e, \Delta x_f = \sin(\alpha_f) \cdot f \\ \Delta y_e &= \sin(\alpha_f) \cdot e, \Delta y_f = \cos(\alpha_f) \cdot f \\ \Delta x &= \max(\Delta x_e, \Delta x_f), \Delta y = \max(\Delta y_e, \Delta y_f) . \end{aligned} \quad (5.14)$$

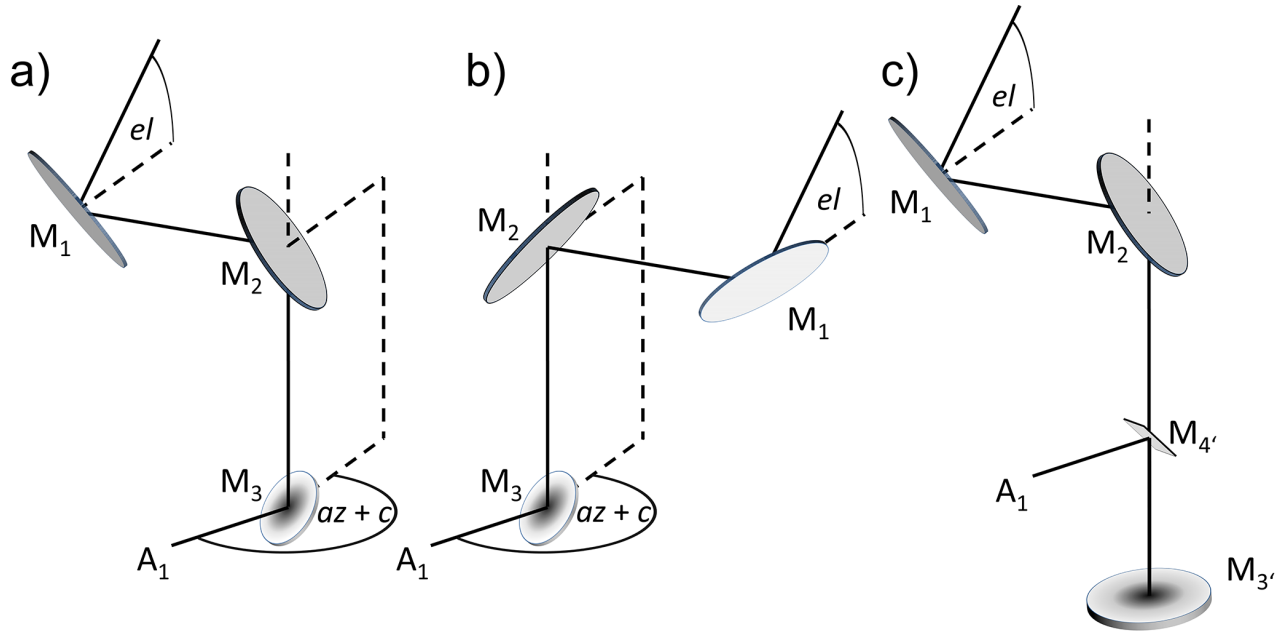


Figure 5.6: Geometry of the Zugspitze solar tracker optics. (a) Current optical setup after September 2014, Flip 1. (b) Current setup, Flip 0. (c) Optical setup before September 2012.

5.4 Example Correction for the Zugspitze FTIR

Solar FTIR and tracker setup

The solar FTIR instrument considered in the example correction is described in detail in Sect. 7 and Sussmann and Schäfer (1997). For the validation of correction results additional data from the nearby Garmisch FTIR (47.48° N, 11.06° E, 743 m a.s.l.) is used.

The geometry of the Zugspitze sun tracker is depicted schematically in Fig. 5.6. The custom-made tracker is located above the spectrometer, in an astronomical dome that is opened for measurements. The tracker optics consists of a first plane 45° elevation mirror (M_1) to adjust the elevation angle (el) of the instrument's line of sight. Sunlight is then guided to the spectrometer below by a second plane 45° mirror (M_2). The azimuth of the line of sight (az) is adjustable by rotation of both mirrors on an arm. The same sky position can be reached by the tracker system with two distinct arm orientations with 180° position difference: Flip 1, used for most measurements and depicted in Fig. 5.6a and Flip 0, used for measurements with $az < 116^\circ$ or $az > 296^\circ$ since September 2012, see Fig. 5.6b.

The setup in place since September 2012 furthermore contains an off-axis mirror (M_3 , $f = 478$ mm) that changes beam orientation to horizontal again and creates an image of the sun on the aperture A_1 . The image of the sun is centered on the aperture A_1 by a quadrant diode continuously giving feedback for tracker positioning. Since September 2014, the active tracking by means of the quadrant diode has been replaced by a Camtracker (Gisi et al., 2011) system inside the spectrometer. Before September 2012, horizontal beam direction and creation of an image on A_1 was achieved by the parabolic mirror M_3' ($f = 1920$ mm) and

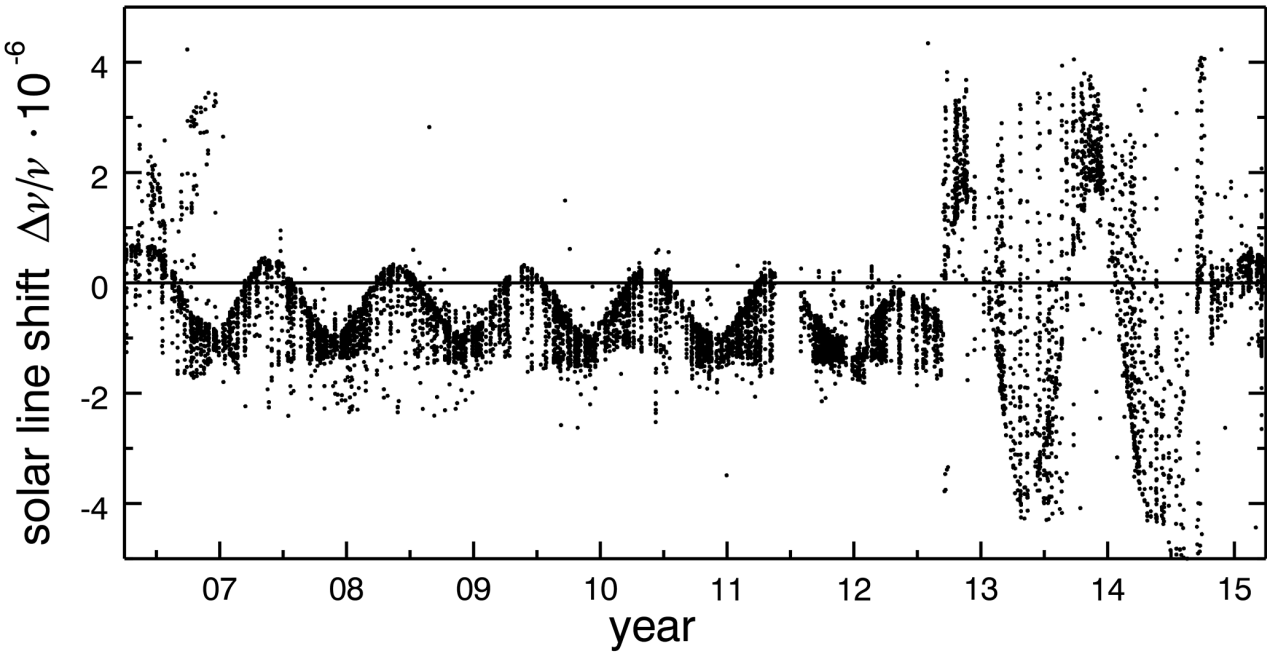


Figure 5.7: Time series of solar line shifts determined from Zugspitze FTIR spectra in the $2400 < \nu < 3100 \text{ cm}^{-1}$ optical filter.

an additional plane mirror M'_4 , instead of the off-axis mirror M_3 (see Fig. 5.6c). The optical configuration was changed in September 2012 in order to enable radiometric calibration of the measured spectra by means of a high-temperature blackbody source. However, due to the smaller size of the solar image at A_1 in the new setup, tracking accuracy has degraded significantly by the modification. This issue highlights the fact that optimum performance of quadrant diode-based sun tracker systems is only ensured within a narrow range of optical configurations. Great care has to be taken when changing parameters such as solar image size to maintain tracking accuracy. Camera-based setups such as the Camtracker system are less sensitive to optical system modifications. The installation of such a system therefore enabled to regain high tracking accuracy for the Zugspitze FTIR.

Implementation of correction

The first step in the implementation of the mispointing correction procedure consists in deducing solar line shifts from the measured spectra as described in Sect. 5.3. Figure 5.7 shows the time series of solar line shifts obtained from the Zugspitze measurements.

As mentioned in Sect. 5.3, the transformation of the solar image by the tracker optics can be characterized by 3×3 imaging matrices that describe changes in beam direction and changes of the solar image in the image plane perpendicular to the beam direction. In the following, we establish those transfer matrices for the optics setup described in the previous section. The corresponding transfer matrices are established for the configurations Flip 1 and Flip 0 in the current optical setup shown in Fig. 5.6a and b and the Flip 1 configuration for

the pre-September 2012 setup shown in Fig. 5.6c.

The complete transformation can be described by a concatenation of three different types of operations:

- i. reflections on a plane mirror perpendicular to the beam direction,
- ii. rotation of the coordinate system and finally
- iii. reflection on 45° mirrors.

Operation (i) corresponds to mirror matrices \mathbf{M} , e.g. for a mirror in the xy -plane

$$\mathbf{M}_{xy} = \begin{pmatrix} 1 & 0 & 0 \\ 0 & 1 & 0 \\ 0 & 0 & -1 \end{pmatrix}. \quad (5.15)$$

Operation (ii) is described by the standard \mathbb{R}^3 rotational matrices $\mathbf{R}_{x/y/z,\varphi}$, where $x/y/z$ designates the direction of the rotation axis and φ the rotation angle in mathematical orientation. Note that a rotation of the coordinate system by an angle φ corresponds to $\mathbf{R}_{x/y/z,-\varphi}$. Reflection on 45° mirrors (iii) can be further decomposed in a combination of rotation according to (ii) to a coordinate system in which the mirror lies in a plane of base vectors, e.g. the xy -plane. This rotation is followed by a reflection according to (i) and a final backwards rotation of the coordinate system. In the following, the transfer matrices for 45° mirrors are designated $\mathbf{S}_{x/y\pm}$, where the x/y -index specifies the coordinate axis parallel to the mirror if the z axis is orientated in beam direction prior to the reflection. The sign in the index is “-” if the third axis points towards the mirror and “+” if the third axis points away from the mirror. The matrices $\mathbf{S}_{x/y\pm}$ have the following form:

$$\mathbf{S}_{x\pm} = \begin{pmatrix} 1 & 0 & 0 \\ 0 & 0 & \pm 1 \\ 0 & \pm 1 & 0 \end{pmatrix}, \quad \mathbf{S}_{y\pm} = \begin{pmatrix} 0 & 0 & \pm 1 \\ 0 & 1 & 0 \\ \pm 1 & 0 & 0 \end{pmatrix}. \quad (5.16)$$

Using the basic operations (i), (ii), and (iii) transfer matrices \mathbf{T} for the Zugspitze sun tracker system can now be deduced. The initial coordinate system valid in the sky is defined with the x axis in horizontal, the y axis in zenith direction and the z axis along the line of sight towards the instrument. After each sub step of the path through the tracker optics, the coordinate system is rotated to orient the z axis in ingoing beam direction.

The individual steps can be tracked in Fig. 5.6. For the current setup and Flip 1 configuration (Fig. 5.6a), the transfer matrix components and final result are:

$$\begin{aligned} \mathbf{T}_{F1} &= \mathbf{T}_{F1}^{-1} = \mathbf{R}_{x,90^\circ} \mathbf{S}_{x+} \mathbf{R}_{z,az} \mathbf{R}_{x,-90^\circ} \mathbf{S}_{x-} \mathbf{R}_{z,el} \mathbf{R}_{y,-90^\circ} \mathbf{S}_{y+} \\ &= \begin{pmatrix} -\cos(-az + el) & -\sin(-az + el) & 0 \\ -\sin(-az + el) & \cos(-az + el) & 0 \\ 0 & 0 & 1 \end{pmatrix} \end{aligned} \quad (5.17)$$

Note that \mathbf{T}_{F1} describes the transfer to a spectrometer coordinate system in which the x and y axes are rotated relative to the horizontal and vertical direction by a constant angle c . As visible in Fig. 5.6, this constant rotation angle c depends on the orientation of the spectrometer and is equal for all measurements in all optical configurations. Since a transformation to a common spectrometer coordinate system with arbitrary orientation is sufficient for our analysis, the constant rotation is neglected in all transfer matrices.

In Flip 0 configuration (Fig. 5.6b), the corresponding matrix is given by

$$\begin{aligned}\mathbf{T}_{F0} &= \mathbf{T}_{F0}^{-1} = \mathbf{R}_{x,90^\circ} \mathbf{S}_{x+} \mathbf{R}_{z,az} \mathbf{R}_{z,180^\circ} \mathbf{R}_{x,-90^\circ} \mathbf{S}_{x-} \mathbf{R}_{z,-el} \mathbf{R}_{y,90^\circ} \mathbf{S}_{y-} \\ &= \begin{pmatrix} \cos(az + el) & -\sin(az + el) & 0 \\ -\sin(az + el) & -\cos(az + el) & 0 \\ 0 & 0 & 1 \end{pmatrix}.\end{aligned}\quad (5.18)$$

For the optical setup before September 2012 and Flip 1 configuration (Fig. 5.6c), we obtain:

$$\begin{aligned}\mathbf{T}_{F1old} &= \mathbf{R}_{x,-90^\circ} \mathbf{S}_{x\pm} \mathbf{R}_{y,180^\circ} \mathbf{M}_{xy} \mathbf{R}_{z,az} \mathbf{R}_{x,-90^\circ} \mathbf{S}_{x-} \mathbf{R}_{z,el} \mathbf{R}_{y,-90^\circ} \mathbf{S}_{y+} \\ &= \begin{pmatrix} \cos(-az + el) & \sin(-az + el) & 0 \\ -\sin(-az + el) & \cos(-az + el) & 0 \\ 0 & 0 & 1 \end{pmatrix} \neq \mathbf{T}_{F1old}^{-1} \\ \mathbf{T}_{F1old}^{-1} &= \begin{pmatrix} \cos(-az + el) & -\sin(-az + el) & 0 \\ \sin(-az + el) & \cos(-az + el) & 0 \\ 0 & 0 & 1 \end{pmatrix}\end{aligned}\quad (5.19)$$

The next analysis step consists in dividing the measurement time series in time bins. For the Zugspitze measurements, each time bin was chosen to comprise the number of measurement days necessary to reach a total number of at least n_{min} spectra in the bin. The choice of time bin size n_{min} results from a trade-off between the statistical uncertainty of the mispointing result and the degree of fulfillment of the assumption that mispointing is approximately constant within each time bin.

Figure 5.8 demonstrates this trade-off: the mean error of the mispointing result in zenith direction (Δm_y) declines with increasing bin size. Variations of the mispointing within a time bin result in scatter of the intersection coordinates for different measurement pairs included in the bin. Therefore, the scatter of the intersection coordinates as given by their standard deviation divided by the norm of the mispointing vector indicates how well the assumption of constant mispointing is fulfilled. As visible in Fig. 5.8a, the median of this intra-bin scatter increases with increasing n_{min} , indicating more variability of mispointing within time bins. As an indicator to find an optimum n_{min} , we use the mean of XCH_4 diurnal variation over the measurement time series (see Sussmann et al., 2011). Since the underlying real XCH_4 diurnal variation can be assumed to be significantly lower than the measured values, n_{min} is chosen to minimize the measured diurnal variation. As shown in Fig. 5.8b, a bin size of $n_{min} = 20$ is chosen for the Zugspitze measurements based on this criterion. The mean number of measurement days included in a time bin is 7.1 days. The mispointing determination scheme

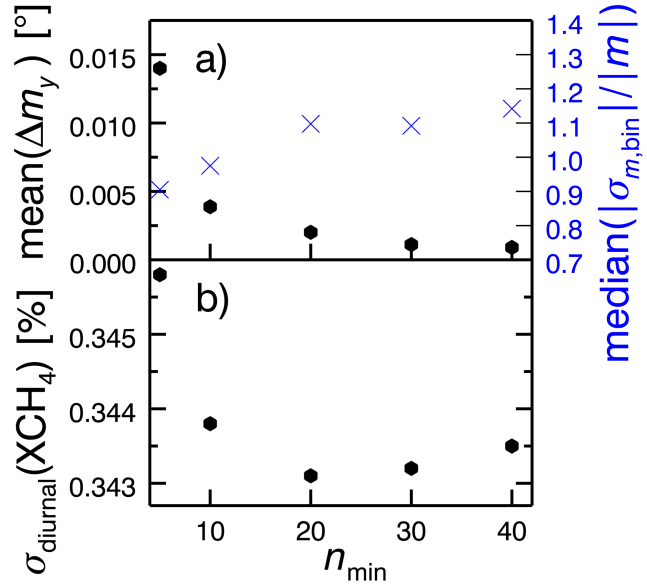


Figure 5.8: Choice of time bin size for Zugspitze mispointing determination. **(a)** Mean zenith mispointing error (black) and median of the relative scatter of mispointing results within time bins (blue). **(b)** Mean 1 σ -XCH₄ diurnal variation.

outlined in Sect. 5.3 can now be applied to the binned data, and the corresponding results are presented in Sect. 9.

Chapter 6

Radiometric Calibration of NIR Solar Absorption Spectra

In this chapter, a novel method for the radiometric calibration of solar absorption spectra in the NIR is presented. Previously, no standard calibration scheme which meets the accuracy requirements of the closure experiment was available for this spectral range. However, radiometric calibration is a prerequisite for the use of solar FTIR spectra for water vapor continuum quantification.

The technique outlined here consists in a combination of two methods: firstly the Langley method, which enables highly accurate calibration in spectral windows with little atmospheric absorption. The Langley results are combined with measurements of a high-temperature blackbody source, which enables constraining the shape of the calibration curve between the windows suitable for Langley measurements.

6.1 Instrumental Setup

Zugspitze NIR Solar Absorption Measurements

The NIR solar absorption spectra to which the calibration is applied are measured with the solar FTIR spectrometer located at the high-altitude observatory on the summit of Mt. Zugspitze, Germany. The spectrometer setup is described in more detail in Süssmann and Schäfer (1997) and Sect. 7.2.

Spectra are typically measured with a liquid nitrogen-cooled InSb detector (1850 to 9600 cm^{-1}) in combination with a KBr beam splitter. An alternative setup consisting of an InGaAs detector (4000 to 12800 cm^{-1}) and a CaF_2 beam splitter is available. This setup has the advantage of improved signal-to-noise ratio especially above 6000 cm^{-1} and avoids a spectral interval of low instrumental sensitivity between 5200 to 5800 cm^{-1} attributed to low transmissivity of the KBr beam splitter. However, for routine operations of the solar FTIR spectrometer, especially for the long-term determination of atmospheric trace gas column

Table 6.1: Specifications of the blackbody calibration source.

Type	MIKRON M330-EU
Manufacturer	Lumasense Technologies
Temperature range	573.15 K to 1973.15 K
Temperature uncertainty	$\pm 0.025 \cdot (T - 273.15 \text{ K}) \pm 1 \text{ K}$
Source homogeneity	$\pm 1 \text{ K}$ within inner 1/3 of aperture
Aperture diameter	25 mm
Emissivity	0.99 ± 0.005

amounts and vertical profiles (e.g. Borsdorff and Sussmann, 2009; Sussmann et al., 2009, 2012; Hausmann et al., 2016), the first option is more suitable. Therefore, most spectra to be calibrated were recorded with the InSb/KBr setup, while the InGaAs/CaF₂ setup was only used in a number of single-day measurement campaigns. While the calibration scheme presented here is applicable for both configurations, we therefore focus on the InSb/KBr setup throughout the remainder of this chapter.

Blackbody Calibration Unit

The calibration procedure makes use of a blackbody calibration source installed in the Zugspitze solar FTIR dome. The calibration source (MIKRON M330-EU, Lumasense Technologies) is shown in Fig. 6.1, while its technical specifications according to the manufacturer are given in Table 6.1. Blackbody spectra are measured with the solar FTIR using the solar tracker optics and an additional gold-coated 90° off-axis mirror. The thermal radiation emitted by the calibration source is directed to the solar tracker by means of the additional off-axis mirror, whose distance to the blackbody cavity interior is set to its focal length of $f = 478 \text{ mm}$. Blackbody source and off-axis mirror are aligned in order to produce a parallel beam with a diameter of 156 mm that is incident at a 90° angle on the solar tracker elevation mirror.

6.2 Langley Calibration

Our approach comprises a Langley-type calibration which is described in this section and a blackbody calibration presented in Sect. 6.3. Our new calibration strategy is a combination of both as explained in Sect. 6.4.

General Description

The Langley method (described e.g. by Liou, 2002) has been frequently used for solar constant determination or calibration of sun photometers. It relies on repeated measurements of solar irradiance or radiance at a range of solar zenith angles. Taking the logarithm of the Beer-Bouguer-Lambert law (Eq. 1.7) results in the linear relation

$$\ln(\mathbf{F}(\nu)) = \ln(\mathbf{F}_0(\nu)) - \mathbf{k}(\nu) \cdot m, \quad (6.1)$$

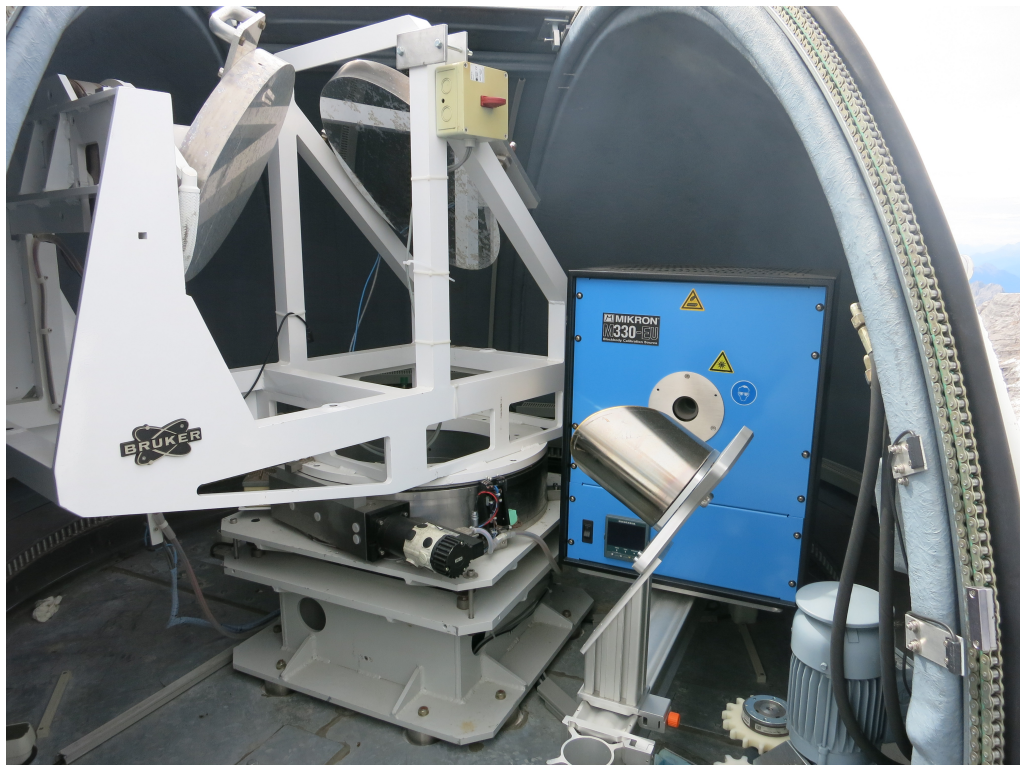


Figure 6.1: Blackbody calibration source inside the Zugspitze solar FTIR dome, additional 90° off-axis mirror and solar tracker.

where $\mathbf{F}_0(\nu)$ denotes the extra-atmospheric solar irradiance, $\mathbf{k}(\nu)$ the atmospheric absorption coefficient and m the relative airmass, i.e. the ratio of the airmass along the line of sight of the observer to the sun and the airmass in zenith direction.

Equation 6.1 implies that the logarithm of the extra-atmospheric solar irradiance can be calculated by measuring solar radiance at a range of airmass values and interpolation of the results to airmass 0 according to the best fit linear relation between airmass and logarithm of measured radiance. The resulting value of $\mathbf{F}_0(\nu)$ can then be compared to the known extra-atmospheric solar spectrum (ESS) to yield a radiometric calibration at that wavenumber. An inversion of this scheme, i.e. deducing an ESS from calibrated solar FTIR measurements was presented by Menang et al. (2013).

Equation 6.1 is only fulfilled if atmospheric properties like IWV or AOD do not vary during the measurements. Since IWV varies significantly even over short time scales (e.g. Kämpfer, 2013; Vogelmann et al., 2015), accurate Langley measurements in spectral regions with significant absorption by water vapor have to be carried out within short time intervals, i.e. at high solar zenith angles. Refraction has a significant influence at high solar zenith angles. In order to include refraction effects, airmass values used in this study were computed by means of ray tracing calculations. Since atmospheric absorption is dominated by water vapor for most spectral points considered in this study, instead of using the air column, the related water vapor column was utilized as an airmass input to the Langley fits.

Selection of Suitable Spectra

Langley calibration coefficients were determined from daily sets of selected solar FTIR spectra recorded under apparently cloud-free conditions at 0.02 cm^{-1} resolution and averaged over 4 scans. Several effects may lead to radiance measurements inconsistent with Eq. 6.1 and thereby lead to biased calibration results. A first issue is related to the fact that the instrument's field of view (FOV) covers different areas of the solar tracker mirrors throughout the day. This is a result of inaccuracies in mirror alignment. Mirror aging and dirtying leads to spatially inhomogeneous reflectivity of the tracker mirrors. Therefore, even if the atmospheric radiance is constant, a spurious variation in measured radiance depending on the instrument's viewing direction can be detected, which leads to calibration errors. Thin clouds in the line of sight of the solar FTIR reduce the measured radiance and therefore also bias the calibration result.

A preliminary Langley plot is used to select the spectra which are least affected by cloud, IWV variation, and FOV effects:

- i. A spectral interval with little molecular absorption, namely $4300\text{ cm}^{-1} < \nu < 4350\text{ cm}^{-1}$, was selected. Within this interval, Langley plots according to Eq. 6.1 were generated using the mean radiance for spectral points with the lowest atmospheric optical depth (red and green points in Fig. 6.2).
- ii. A first estimate of the linear relation avoiding cloud and FOV bias (continuous black line in Fig. 6.2) was fitted using the spectra with the highest mean radiance within each

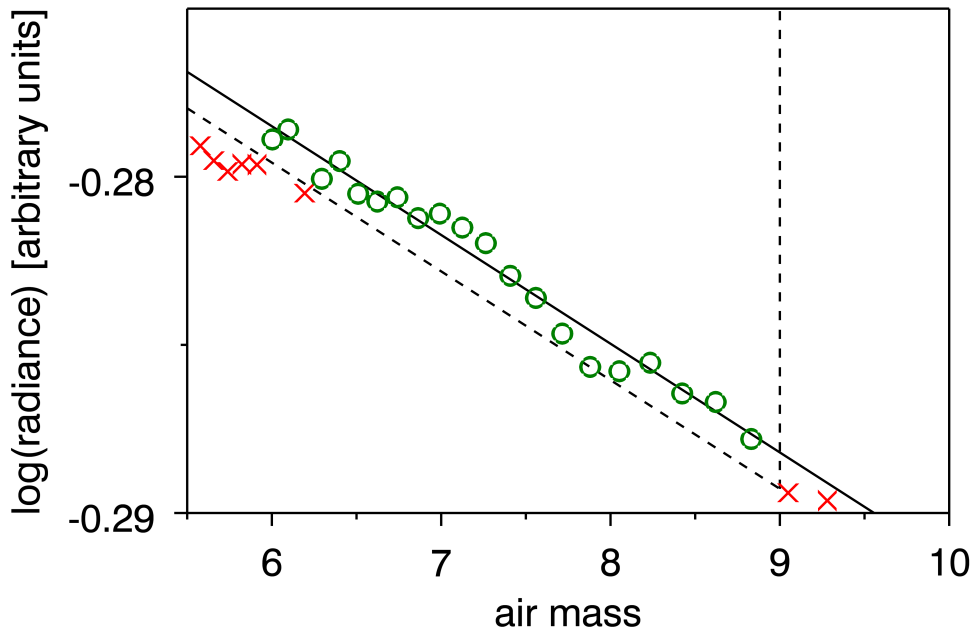


Figure 6.2: Selection of spectra for the Langley measurements made on 13 December 2013. Continuous black line: first estimate linear fit, dashed black line: selection threshold, green circles: selected spectra, red crosses: excluded spectra

airmass bin (width $\Delta m = 1$). airmass bins for which the mean radiance did not decrease with increasing airmass as expected for cloud-free measurements were discarded.

- iii. The maximum deviation from the ideal linear relation not attributable to FOV influence or IWV temporal variability was calculated. The FOV effect was estimated as will be outlined in Sect. 6.5. Based on the results of Vogelmann et al. (2015), the expected IWV variability was estimated to be about 1 mm during typical Langley measurements with 1-2 h duration.
- iv. Spectra consistent with the linear relation determined in (ii) minus the maximum deviation estimated in (iii) measured at an airmass less than 9.0 were selected for further analysis (dashed line in Fig. 6.2). An airmass threshold is required since, at very high solar zenith angles, airmass calculation becomes increasingly inaccurate, and airmass changes significantly during the spectral averaging period. The selected spectra are shown as green circles in Fig. 6.2, while discarded spectra are shown in red.

Further analysis is carried out for Langley datasets with a sufficiently high number of selected spectra according to the selection criteria presented above (> 10 measurements) over an airmass range of at least $\Delta m = 2$ and with $IWV < 5$ mm, since moist atmospheric conditions reduce the fraction of spectral intervals suitable for accurate calibration. Langley measurements fulfilling these criteria were recorded on 12 December 2013 and 13 December 2013.

Choice of Solar Spectrum

The Langley calibration method requires knowledge of the ESS. In this study, the semi-empirical synthetic ESS of Kurucz (2005) is used. This extra-atmospheric spectrum is widely adopted for atmospheric radiative transfer calculations due to its high spectral resolution (radiance spectra are provided with 0.1 cm^{-1} point spacing) and its wide spectral range (0 to 50000 cm^{-1}). This ESS can be easily replaced by alternative spectra without further modifications to the calibration method.

Possible alternative ESS choices include the spectrum proposed by Thuillier et al. (2003) that is based on satellite observations. This spectrum covers a range of 0.1 to 2400 nm with a NIR spectral resolution of 0.5 nm. This resolution allows for the identification of broad solar lines but does not provide fine enough resolution for a detailed representation of solar line shapes. An advantage of the Thuillier et al. (2003) solar spectrum over the Kurucz (2005) spectrum is that it includes an uncertainty estimate that can be used in the uncertainty analysis of the radiometric calibration. A further alternative high-resolution ESS was deduced by Menang et al. (2013) using the Langley technique in comparison with the blackbody calibration implemented by Gardiner et al. (2012). The influence of ESS inaccuracies on the calibration uncertainty will be discussed in Sect. 6.5.

Langley Fit and Spectral Window Selection

A number of issues have to be considered before generating Langley fits according to Eq. 6.1 using the selected spectra. During measurements, the line of sight of the solar FTIR continuously tracks the position of the center of the solar disc. Sun tracking inaccuracies influence the Langley measurements due to the spatial inhomogeneity of the solar emission, the so-called solar limb darkening. Furthermore, mispointing leads to erroneous airmass input for the Langley fit. As outlined in Chapter, systematic mispointing can be determined using multiple measurements of solar line Doppler shifts at different orientations of the solar rotation axis. Using this method, mispointing-corrected airmass values can be calculated as an input to the Langley fits. The effect of solar limb darkening can be corrected for using the analytical description of relative intensity of NIR solar radiation depending on the fractional radius r given by Hestroffer and Magnan (1998),

$$\mathbf{I}(r) = (1 - r^2)^{\alpha/2}, \quad (6.2)$$

where $\alpha = -0.023 + 0.29210^{-4}\text{ cm}\cdot\nu$. The mispointing correction consists in multiplying the calibration result by $\mathbf{I}(r)$, where r designates the norm of the mispointing divided by the apparent solar radius.

The uncertainty of the Langley calibration varies strongly throughout the spectrum. Therefore, it is necessary to select spectral windows in which accurate Langley results can be obtained. Figure 6.3 shows the selection steps applied to the Langley results. In the following, several selection criteria make use of upper or lower linear envelopes to the spectra. These envelopes are constructed by selecting the highest or lowest values in the spectra within each wavenumber

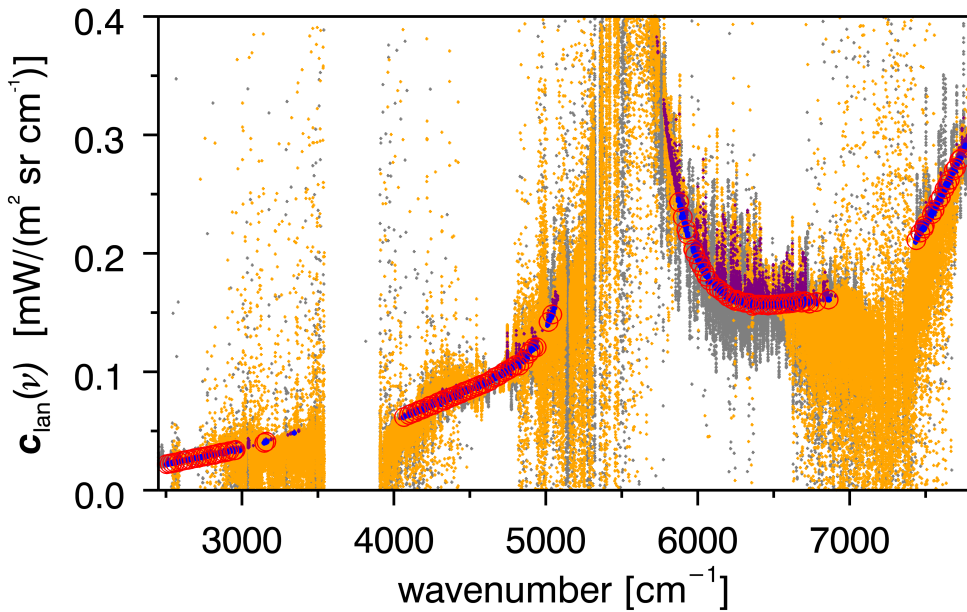


Figure 6.3: Selection of suitable spectral points and averaging for Langley calibration (measurements from 13 December 2013). Grey: initial Langley fit results; orange: results not affected by solar lines; purple: results after applying fit uncertainty threshold; blue: final results after applying stability threshold; red circles: Langley calibration results averaged over 20 cm^{-1} bins.

bin of a given width. The envelope is then constructed by linear interpolation between these selected points. In detail, the following selection criteria were used:

- i. Spectral points within solar lines are excluded due to the higher ESS radiance uncertainty in these regions. In detail, all points with ESS radiance more than 1 % below the upper linear envelope using 20 cm^{-1} width bins are excluded (grey points in Fig. 6.3).
- ii. All spectral points for which the relative Langley fit uncertainty was above 0.4 % were discarded (orange points in Fig. 6.3).
- iii. Furthermore, regions within solar lines not included in the ESS of Kurucz (2005) and points with spurious low fit uncertainty due to radiance measurement noise were excluded. For this purpose, all points for which the standard deviation of Langley calibration results within a 0.1 cm^{-1} -wide interval around any given spectral point exceeds 0.3 % were excluded (purple points in Fig. 6.3).

Blackbody spectral radiance measurements (see Sect. 6.3) show that the solar FTIR calibration curve varies only slowly with wavenumber. The filtered Langley results (blue points in Fig. 6.3) were therefore averaged (error-weighted mean using Langley fit uncertainties) over 20 cm^{-1} -windows in order to further reduce statistical uncertainty. The final averaged Langley calibration coefficients are shown as red circles in Fig. 6.3 and are designated “Langley points” throughout the remainder of this study.

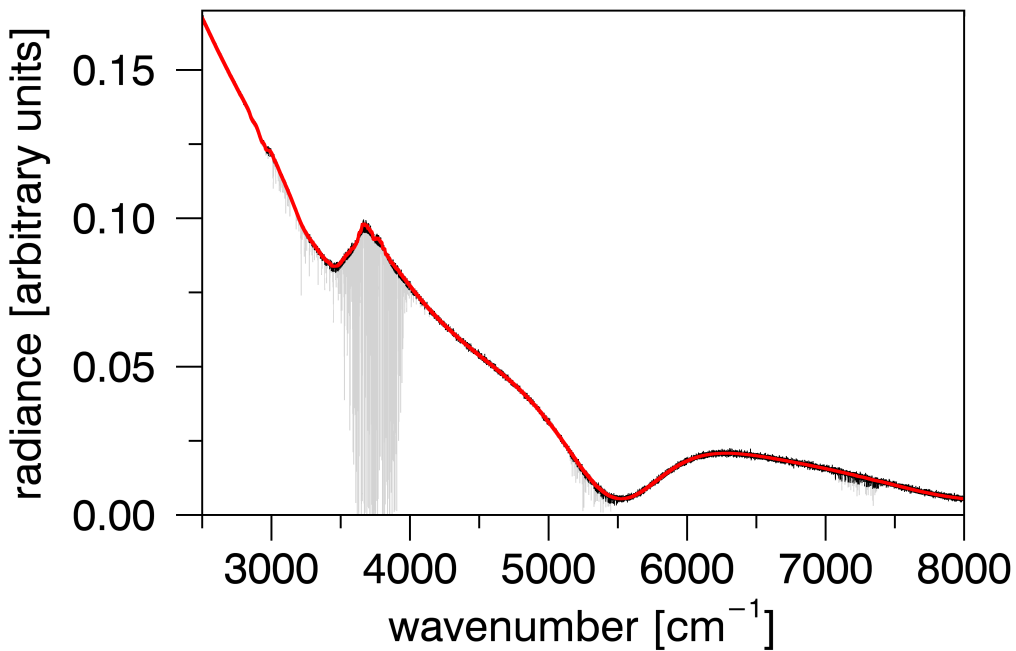


Figure 6.4: Blackbody radiance spectrum recorded on 24 February 2014 with a cavity temperature of 1923.15 K. Grey: measured spectrum, black: result of spectral line exclusion, red: final spectrum after median filtering.

6.3 Blackbody Calibration

Spectral radiance measurements of the blackbody calibration source described in Sect. 6.1 are used to determine the shape of the calibration curve in spectral intervals between the points suitable for precise Langley calibration. Contrary to the calibration approach described by Gardiner et al. (2012), using a source with a temperature of 3000 K, a lower cavity temperature of 1973 K can be used in the Zugspitze experiment due to the combination with Langley measurements. Blackbody calibration spectra were measured with a resolution of 0.02 cm^{-1} .

In order to avoid biased calibration results due to water vapor line absorption in the blackbody spectra, only measurements with an atmospheric water vapor density $\rho_{\text{H}_2\text{O}} < 1 \text{ g m}^{-3}$ at the Zugspitze summit observatory were considered for calibration. Spectra are averaged over time intervals with stable blackbody radiance, i.e. periods for which changes in air temperature inside the solar FTIR dome were slow enough to be compensated by the blackbody thermostat.

Only spectral points outside water vapor lines were considered to avoid bias in the calibration. In detail, only points less than 10σ (where σ designates the mean measurement noise) below the upper envelope of the measured spectra were selected (black spectrum in Fig. 6.4). The influence of measurement noise can then be further reduced by applying a median filter (20 cm^{-1} width) to the spectra (red spectrum in Fig. 6.4). Finally, the blackbody calibration curve $\mathbf{c}_{\text{bb}}(\nu)$ is calculated from the averaged spectra by dividing the Planck curve at the cavity temperature T_{bb} as defined in Eq. 1.4 by the measured spectrum.

6.4 Combined Calibration Method

The combined calibration strategy takes advantage of the low-uncertainty Langley calibration at suitable spectral points (see Sect. 6.2). In between the Langley points, the shape of the calibration curve is constrained by the blackbody measurements (see Sect. 6.3). The combined calibration curve $\mathbf{c}(\nu)$ is given by the relation

$$\mathbf{c}(\nu) = \mathbf{c}_{\text{bb}}(\nu) \cdot \mathbf{c}_{\text{lan, linear}}(\nu) / \mathbf{c}_{\text{bb, linear}}(\nu) , \quad (6.3)$$

where \mathbf{c}_{bb} designates the blackbody calibration curve derived according to Sect. 6.3. $\mathbf{c}_{\text{lan, linear}}$ and $\mathbf{c}_{\text{bb, linear}}$ designate linear interpolations constructed as follows: at the Langley calibration points, $\mathbf{c}_{\text{lan, linear}}$ and $\mathbf{c}_{\text{bb, linear}}$ are set to the Langley and blackbody calibration results, respectively. In between these points, $\mathbf{c}_{\text{lan, linear}}$ and $\mathbf{c}_{\text{bb, linear}}$ are calculated by linear interpolation.

6.5 Calibration Uncertainty

Contributions from Langley Calibration

Several contributions to the calibration uncertainty budget are associated with the Langley measurements. A first contribution results from the uncertainty of the Langley fit. This contribution is calculated as an error-weighted mean over the 2σ fit uncertainties of the spectral points contributing to each Langley point. In between Langley points, the uncertainty estimate is obtained by linear interpolation. The Langley contribution to the calibration uncertainty ranges from 0.35 to 0.72 % throughout the spectral range considered for calibration and is shown in Fig. 6.5 (blue line).

Furthermore, a combination of spatially inhomogeneous reflectivity of the solar tracker mirrors and the fact that the area covered by the instrument's FOV on the mirrors changes over time leads to spurious radiance variations in the Langley calibration. To obtain an estimate of this error, the time-dependent position of the instrument FOV on the tracker elevation mirror was measured using an outgoing laser beam aligned with the instrument's optical axis. In the spectral regions with least atmospheric absorption, the diurnal variation of the measured signal is about 5 %. A conservative estimate of the FOV-related error is obtained assuming that this diurnal variation is solely due to mirror inhomogeneity and that mirror reflectivity drops abruptly by this amount outside the area initially covered by the FOV. Consequently, the error estimate is obtained by multiplying the 5 % reflectivity change with the fraction by which the area within the field of view has changed throughout the calibration time interval. The resulting Langley calibration uncertainty due to mirror inhomogeneity is $\sim 0.2\%$ (cyan line in Fig. 6.5).

The accuracy of the Langley results is also limited by errors in the airmass values used for the fit. Firstly, this is due inaccurate solar zenith angle input. A second and by far dominant effect is due to the fact that the relative airmass for absorbing species with different concentration profiles is not equal for a given solar zenith angle. Depending on the spectral region, the dominant contribution to atmospheric OD for most Langley points is either due

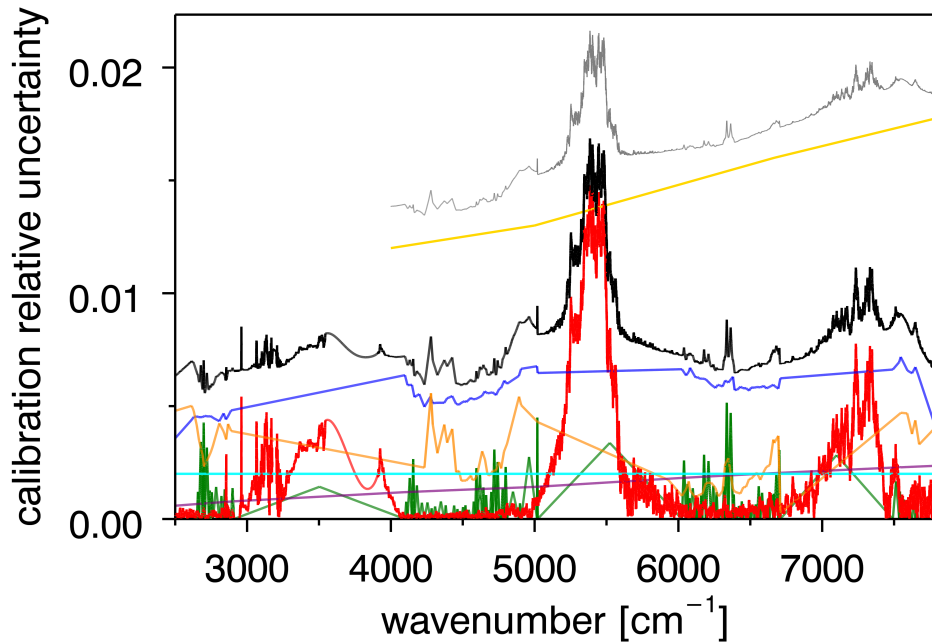


Figure 6.5: Relative 2- σ calibration uncertainty (Langley measurements made on 13 December 2013, blackbody measurements on 24 February 2014). Blue: Langley fit uncertainty, red: blackbody uncertainty, green: shape error uncertainty, orange: airmass uncertainty, purple: mispointing uncertainty, cyan: FOV uncertainty, yellow: ESS uncertainty according to Thuillier et al. (2003), grey: total uncertainty, black: total uncertainty relevant for radiative closure experiment (not including ESS contribution).

to water vapor or aerosols. For our analysis, water vapor relative airmasses were used. The difference of the calibration results when performing the analysis with relative air columns instead of water vapor columns is up to 0.5 % and was taken as an estimate of the airmass related calibration uncertainty (see orange line in Fig. 6.5).

An additional uncertainty contribution of up to 0.25 % results from the uncertainty of the mispointing correction outlined in Sect. 6.2 (purple line in Fig. 6.5). This contribution includes two effects related to the mispointing uncertainty: the effects of airmass uncertainty in the Langley fit and the uncertainty in the solar limb darkening correction outlined in Sect. 6.2.

A further uncertainty contribution is associated with the ESS used in the Langley calibration. The 2- σ uncertainty of the Thuillier et al. (2003) spectrum is reported to be in the range of 1.2 % at 4000 cm⁻¹ to 1.8 % at 8000 cm⁻¹, as shown in Fig. 6.5 (yellow lines). However, this uncertainty estimate is not consistent with the differences between ESS results obtained in several recent studies. As an example, the ESS determined by Menang et al. (2013) differs from the results of Thuillier et al. (2003) by about 10 %. Recent studies by Thuillier et al. (2014, 2015) and Weber (2015) confirm that until now, no firm conclusion on the actual magnitude of the ESS in the infrared can be drawn.

For the main goal of this work, namely the determination of water vapor continuum optical depth from calibrated spectra, ESS errors are of negligible importance. This is due to the fact that the same ESS is used for both calibration and calculation of synthetic spectra, which almost entirely eliminates the effect of ESS errors. This feature of the proposed method is demonstrated in Sect. 11.2. For other applications than determination of atmospheric OD in closure studies, the accuracy of the calibration achieved with the combined method depends on the ESS accuracy, which remains to be constrained more securely by future studies.

Blackbody Calibration Uncertainty

A further contribution to the calibration uncertainty results from the blackbody measurements. The blackbody calibration curve uncertainty was calculated as two times the standard deviation of all normalized blackbody calibration curves recorded under suitably dry atmospheric conditions (near-surface atmospheric water vapor density $\rho_{\text{H}_2\text{O}} < 1 \text{ g m}^{-3}$). These measurements include spectra at $T_{\text{bb}} = 1923.15 \text{ K}$ to 1973.15 K cavity temperature. The relative error in the combined calibration curve resulting from the uncertainty of the blackbody measurements does not exceed 1.5 % and is shown in Fig. 6.5 (red lines).

Combined Calibration Uncertainty Estimate

The combined calibration according to Eq. 6.3 is based on the assumption that the blackbody calibration curve between suitable Langley points can be approximately described by multiplying the Langley calibration curve with a linear function, i.e. that the following relation is fulfilled:

$$\mathbf{c}_{\text{bb}}(\nu)/\mathbf{c}_{\text{bb, linear}}(\nu) \approx \mathbf{c}_{\text{lan}}(\nu)/\mathbf{c}_{\text{lan, linear}}(\nu) \quad (6.4)$$

Equation 6.4 is not exactly fulfilled e.g. if the reflectivity of the additional off-axis mirror used for blackbody measurements does not vary linearly between Langley points. As a consequence, an additional contribution to the calibration uncertainty results from the use of the combined approach presented in Sect. 6.4. In order to obtain an estimate of this shape error contribution, the following procedure was applied:

- i. The calibration error induced by omitting the Langley result at each single Langley spectral point ν_i and using only the neighboring points ν_{i-1} and ν_{i+1} is calculated. A preliminary shape error curve is then constructed from the error values at all ν_i by linear interpolation.
- ii. The final shape error estimate is set to 0 at all Langley points ν_i according to Eq. 6.3. At all spectral points halfway between Langley points, i.e. at $(\nu_{i+1} - \nu_i)/2$, the final error estimate is set to the value of the preliminary curve determined in (i).
- iii. At spectral points between those mentioned in (ii), the estimated error is calculated by linear interpolation. The shape error generally increases with increasing Langley point spacing. By construction, the error estimate resulting from the method given above corresponds to a mean Langley point spacing two times as large as the real spacing. The error estimate provided above is therefore expected to overestimate the real errors in most cases. The final shape error estimate is shown as a green curve in Fig. 6.5 and is up to 0.5 % throughout the spectral range considered.

Thermal emission from instrument parts at room temperature contributes a fraction of less than 10^{-5} to the measured solar radiance within the considered spectral interval. Contrary to the situation for instruments operating in the far-IR spectral range, this contribution is therefore of negligible importance for the calibration error budget. Within the Zugspitze radiative closure experiment, the same ESS is used for Langley calibration and radiative transfer calculations. Therefore, the accuracy of the water vapor continuum optical depth derived in closure experiments from the calibrated spectra is not heavily affected by errors in the extra-atmospheric solar spectrum. The overall uncertainty relevant for water vapor continuum detection, i.e. not including the extra-atmospheric solar spectrum contribution, is shown in Fig. 6.5 (black lines). It is typically below 1 % within the calibration range, except for regions with sparse Langley point density or low beam splitter transmissivity where maxima of up to 1.7 % uncertainty exist. The error budget including the solar spectrum (grey lines in Fig. 6.5) is about 1.5–2.0 % throughout the 4000 to 7800 cm^{-1} wavenumber range.

Chapter 7

Implementation of the Zugspitze Radiative Closure Experiment

This chapter describes the implementation of the basic principle of radiative closure experiments described in Chapter 3 at the Zugspitze summit observatory for water vapor continuum quantification. The implementation makes use of the newly developed methods presented in Chapter 5 and 6.

As outlined in Chapter 3, a comprehensive uncertainty budget for the closure experiment is an important prerequisite for the interpretation of results. This chapter therefore contains a description of all significant contributions to the uncertainty budget of both parts of the experiment, namely the FIR study using thermal emission spectra and the NIR part that relies on solar absorption spectra.

7.1 Idea and Setup

The closure setup includes spectral radiance measurements covering the FIR, the MIR, and the NIR along with atmospheric state measurements, most importantly IWV (Fig. 7.1 and Table 7.2) at the summit of Mt. Zugspitze. The idea of the closure experiment is to compare measured radiance spectra with simulations of the spectra driven by coincident state measurements. Minimization of measured minus simulated spectral radiance (thereafter referred to as “spectral residuals”) leads to improved water vapor absorption parameters used in the radiance simulations (Fig. 3.1). The basic principle behind this approach has been presented before (e.g. Tobin et al., 1999; Turner and Mlawer, 2010). However, there are 4 aspects which are special to our Zugspitze setup:

- i. Very dry atmospheric conditions are a pre-requisite for closure studies of this kind due to the otherwise saturated spectral regions (see e.g. Fig. 1 in Tobin et al., 1999). To achieve this goal, previous campaigns were performed at remote locations like the Sheba ice station (Tobin et al., 1999) or at the Atacama desert where IWV levels down to 0.2 mm were

Table 7.1: Climatological statistics of clear-sky IWV levels above the Zugspitze derived from N multi-annual solar FTIR measurements shown in Fig. 7.2. Numbers (except N) are given in units of mm.

N	mean	stdv	min	median	max
7388	3.0	2.2	0.1	2.3	12.0

achieved (Turner and Mlawer, 2010). On the other hand, at the Zugspitze comparably dry atmospheric conditions (min IWV = 0.1 mm, see Fig. 7.2 and Table 7.1) are frequently encountered, but the Zugspitze is at the same time an easy-to-access site, which can be reached within 20 min by cable car from our institute building at Garmisch-Partenkirchen. Note that the minimum IWV levels at Zugspitze (0.1 mm) are approximately a factor of 40 lower than at typical lowland mid-latitude sites.

- ii. Unlike previous campaign-type studies, our field experiment is designed as a long-term study (time scale \sim 10 years) - this is beneficial for attaining improved measurement statistics.
- iii. The Zugspitze radiative closure experiment is - to our knowledge for the first time - extended to include the NIR spectral range, while previous studies had focused on the MIR (e.g. Tobin et al., 1999) and FIR (e.g. Delamere et al., 2010), respectively.
- iv. A benefit of the Zugspitze high-altitude mountain site is that AOD is typically very low, i.e. about a factor of 10 lower than at typical lowland mid-latitude sites. This is important because otherwise in the NIR the AOD would become significantly higher than the water vapor continuum optical depth and this would be a hindrance for accurate continuum quantification in the NIR (Ptashnik et al., 2015). The AOD levels encountered in the Zugspitze closure data set used in this study (i.e. dry clear sky days within the time span December 2013–February 2014, see Sect. 8.1 for data selection details) are in the range 0.0005–0.00075 at 2500 cm^{-1} and in the range 0.0024–0.0032 at 7800 cm^{-1} at airmass 1.

7.2 Spectral Radiance Measurements

FIR and MIR Radiance Measurements

Downwelling thermal emission is measured in the FIR and MIR spectral range from 400 to 3000 cm^{-1} (3.3–25.0 μm) via an Extended-range Atmospheric Emitted Radiance Interferometer (ER-AERI). This instrument was designed by the University of Wisconsin Space Science and Engineering Centre and is manufactured by ABB Bomem Inc. (Quebec, Canada). Details of the instrument design and performance have been given by Knuteson et al. (2004a,b). Such instruments have been operated e.g. at the SHEBA Ice Station (Tobin et al., 1999), in the Atacama Desert (Turner and Mlawer, 2010), or at Eureka (Mariani et al., 2012). Briefly, the

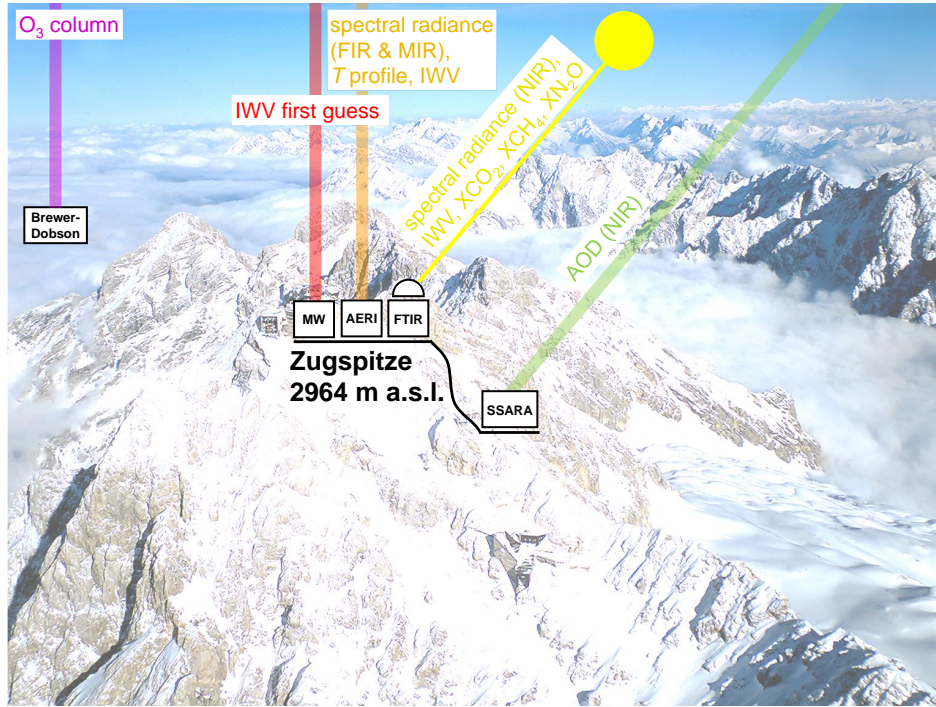


Figure 7.1: Instrumental setup of the Zugspitze radiative closure experiment covering the FIR, MIR, and NIR spectral range (FTIR: Bruker IFS 125 HR high-resolution solar Fourier-Transform infrared Spectrometer; AERI: extended-range Atmospheric Emitted Radiance Interferometer; MW: LHATPRO low-humidity microwave radiometer; SSARA: sun photometer; Brewer-Dobson: ozone spectrophotometer).

instrument inside the Zugspitze container is based on a 0.5 cm^{-1} -resolution (maximum optical path difference $\text{OPD}_{\max} = 1 \text{ cm}$) FTIR spectrometer. The interferometer front window is linked to the frontend which is mounted outside the container in the so-called through-wall configuration and comprises the scene mirror and two blackbodies (BB), at ambient temperature and at 310 K , respectively (Fig. 3.1, top left). The frontend hatch used to protect the scene mirror against precipitation has been modified from its original flat-roof shape to a pitched-roof shape in order to avoid snow accumulations. Scan duration for one interferogram is 2 s and the total repeat cycle is 10 min, with 4 min integration for the atmospheric observations, and 2 times 2 min for the blackbody measurements.

Radiometric calibration of the ER-AERI is performed via the approach by Revercomb et al. (1988). The related FIR and MIR radiometric uncertainty specifications are given in Table 7.2 and more details will be presented in Sect. 7.5. Briefly, there is a known radiometric bias in the ER-AERI radiance measurements which was corrected via the method proposed by Delamere et al. (2010). This method relies on the assumption that a fraction f of the instrument's field of view is obstructed by instrument parts. The value of f is constrained by a fit to measured radiance in the 827 to 835 cm^{-1} spectral window. We obtain $f = 0.0049$ which is then used for performing the bias correction according to Delamere et al. (2010).

An estimate of radiance measurement noise of the ER-AERI is obtained as an output from

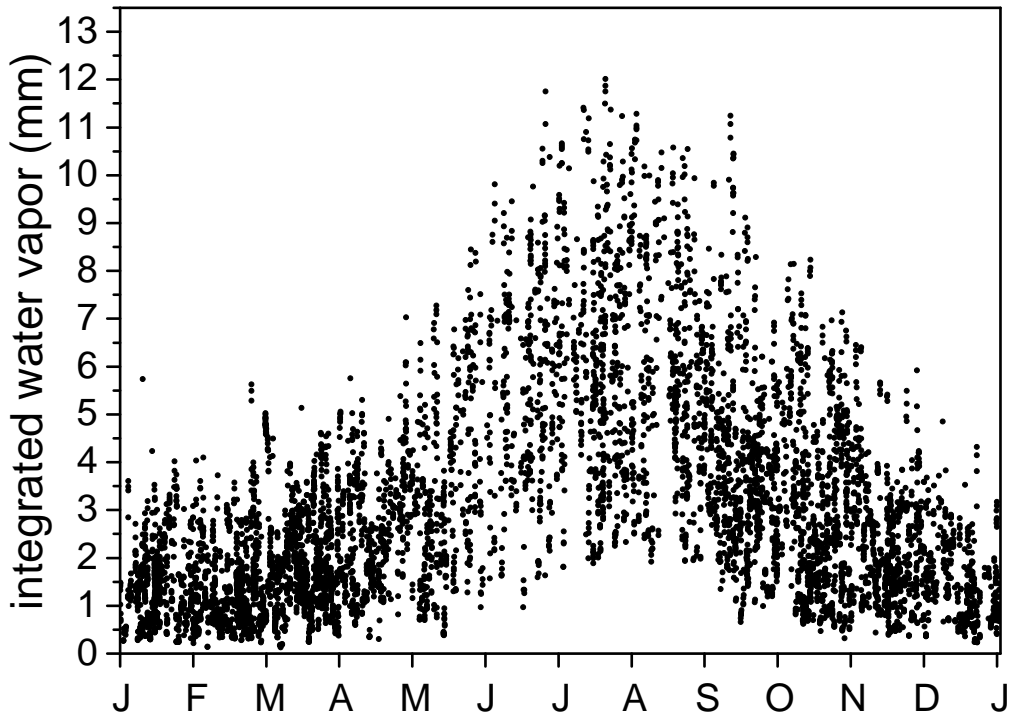


Figure 7.2: Climatology of integrated water vapor above the Zugspitze. Data are from multi-annual (1996–2013) Zugspitze solar FTIR measurements (clear sky, 15–20 min integration; see Sussmann et al., 2009 for details). See Table 7.1 for related statistics.

the calibration procedure, see Sect. 7.5 for numbers. The spectral radiance noise can be reduced using a filter based on principal component analysis as outlined in Antonelli et al. (2004) and Turner et al. (2006). Based on 8000 Zugspitze spectra, this analysis indicated that the use of the first 239 principal components is optimal. This resulted in a ~50 % noise reduction.

NIR Radiance Measurements

Solar absorption spectra in the NIR spectral range from 2500–7800 cm^{−1} (1.3–4.0 μm) were measured using the Zugspitze high-resolution solar FTIR system based on a Bruker IFS 125 HR interferometer with an optical path difference up to 418 cm (Sussmann and Schäfer, 1997). This instrument is operational since 1995 for spectrometric MIR trace gas measurements within the NDACC network. The NIR operations are utilizing an InSb detector along with a KBr beam splitter (InGas/CaF₂ optional), interferograms are recorded with a OPD_{max} of 45 cm and averaged over 4 to 8 scans for one spectrum (75–150 s integration time). Radiometric calibration is achieved by a novel approach utilizing a combination of the Langley calibration method and a hot blackbody calibration source (< 2000 K) used for interpolating the calibration curve between the individual spectral Langley calibration points (see Chapter 6 for detailed information). Related NIR radiometric uncertainties are given in Table 7.2 and will be further discussed in Sect. 7.5.

7.3 State Measurements

Integrated water vapor and water vapor profiles

For the closure experiments based on ER-AERI radiance measurements in the FIR and MIR, IWV is directly retrieved from ER-AERI spectra. This allows for an ideal spatiotemporal matching between the radiance measurements in the terrestrial infrared and the corresponding IWV state measurements. IWV is retrieved by minimizing ER-AERI vs. LBLRTM spectral residuals in IWV-sensitive windows. For this purpose an approach similar to the method proposed by Serio et al. (2008) was implemented. Details of the IWV retrieval and the procedure for selection of suitable spectral windows are outlined below. Numbers for the uncertainty of the ER-AERI-based IWV retrieval are given in Table 7.2. The underlying uncertainty analysis and the resulting radiance uncertainty are presented in Sect. 7.5.

The approach used in this study is similar to the method proposed by Serio et al. (2008), i.e. IWV is retrieved via a derivative approach using one iteration to minimize ER-AERI vs. LBLRTM spectral residuals in IWV-sensitive windows. As first guess IWV, data from a LHATPRO microwave radiometer are used. LHATPRO (Radiometer Physics, Germany; Rose et al., 2005), designed for ultra-low humidity sites ($\text{IWV} < 4.0 \text{ mm}$), is a microwave radiometer located side-by side to the ER-AERI.

The procedure for selection of suitable spectral windows for IWV retrieval from the 400–600 cm^{-1} spectral range has been implemented as follows:

- i. All regions in which continuum has significant influence on the downwelling radiance (relative continuum uncertainty $< 100\%$) are excluded in order to avoid biased water vapor continuum quantification results due to the IWV fit.
- ii. The uncertainty of the IWV fit for single spectral points is calculated for the remaining windows. IWV relative uncertainty is given as the residual uncertainty excluding IWV contribution divided by $\partial \mathbf{I} / \partial \text{IWV}$, i.e. the derivative of downwelling spectral radiance \mathbf{I} with respect to IWV. The overall uncertainty comprises two classes of errors, namely type-(i) errors which are uncorrelated with wavenumber, and type-(ii) errors correlated with wavenumber.
- iii. Spectral points (channels) are ordered from lowest to highest type-(ii) uncertainty.
- iv. Ensembles with stepwise increased number of channels are constructed including channels with increasing type-(ii) uncertainty, and the overall uncertainty, i.e. type (i) + (ii), is calculated for each ensemble. Figure 7.3 shows this overall uncertainty depending on the number of included channels. ER-AERI measurement noise and line parameter errors are treated as type-(i) error contributions (the underlying assumption being that line parameter errors for different lines are independent). Therefore, these contributions to the cumulative uncertainty are reduced by a factor $1/\sqrt{n}$ when n channels are included in the fit (causing the decrease of uncertainty on the left hand side of Fig. 7.3). All other uncertainty contributions (ER-AERI calibration, T profile errors, and water vapor profile

Table 7.2: Instruments and geophysical parameters measured at the Zugspitze radiative closure experiment. Uncertainties are given for 2σ confidence.

geophys. Parameter	instrument	repeat cycle	uncertainty/specification
FIR & MIR spectral radiance (400–3000 cm ⁻¹)	ER-AERI	10 min	¹ resolution 0.5 cm ⁻¹ calibration bias <0.66 % of ambient BB radiance calibration precision <0.13 % of ambient BB radiance
NIR spectral radiance (2500–7800 cm ⁻¹)	solar FTIR	75–150 s	¹ resolution 0.01 cm ⁻¹ calibration accuracy 0.6–1.7 % of measured radiance
IWV (ER-AERI)	retrieval from ER-AERI spectra	10 min	bias 4.4 % precision 4.3 %
IWV (solar FTIR)	retrieval from solar FTIR spectra	75–150 s	bias 1.1 % precision 0.8 %
water vapor profile shape	NCEP	6 h	bias 1.7 % precision 9.4 %
temperature profile	ER-AERI & NCEP	10 min	accuracy <1 K
O ₃ column	Brewer-Dobson	~30 min	accuracy <1 %
XCO ₂	TCCON	100 s	bias <0.07 % precision <0.25 %
XCH ₄	TCCON	100 s	bias <1.04 % precision <0.3 %
XN ₂ O	TCCON	100 s	bias <1.85 % precision <0.5 %
NIR AOD	SSARA-Z	1 s	accuracy at airmass <0.0015 (at 2500 cm ⁻¹) <0.0025 (at 7800 cm ⁻¹)

¹resolution defined as $1 / (2 \cdot \text{OPD}_{\max})$

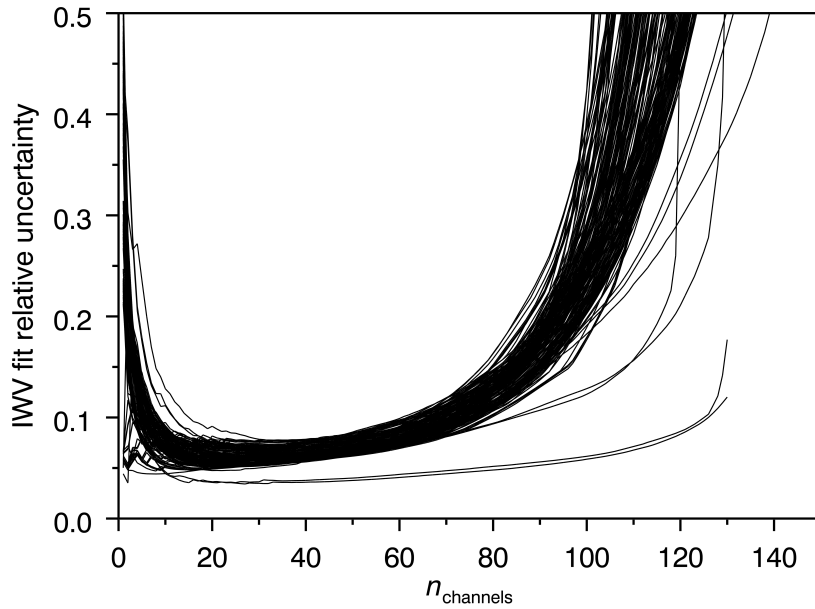


Figure 7.3: Relative uncertainty of the IWV fit depending on the number of spectral points n_{channels} used in the fit for the spectra included in the FIR continuum data set. Channels are ordered by increasing type (ii)-uncertainty. The number of channels used for the fit is adjusted in order to yield minimum overall uncertainty.

errors, see Sect. 7.5 for details) are correlated for different spectral channels, therefore no uncertainty reduction is achieved by including more channels in the fit, and the overall uncertainty increases toward the right hand side of Fig. 7.3. This is because more and more channels with increasing type-(ii) uncertainty are included.

- v. The optimum number of spectral channels for the fit is deduced from the minimum of overall, i.e. type-(i) + (ii) uncertainty (Fig. 7.3). The resulting optimum numbers of channels for the different spectra of our closure dataset are shown in Fig. 7.4; the mean value is 23.7 channels, with a minimum of 8 and a maximum of 40 channels. The results of the IWV fit for all spectra included in the FIR closure data set are shown in Fig. 7.5. The mean correction relative to the LHATPRO first guess IWV was -0.051 mm, with a standard deviation of 0.075 mm.

For the NIR closure measurements, IWV was retrieved directly from the solar FTIR spectral radiance measurements (see Sect. 7.2) using a MIR retrieval scheme which exploits several spectral micro-windows in the $2610\text{--}3050\text{ cm}^{-1}$ range (Schneider et al., 2012, 2016). Again, this allows for an ideal spatiotemporal matching of the solar infrared radiance measurements and the correlative IWV state measurements. Specifications of the uncertainty of the IWV retrieval from the solar FTIR are given in Table 7.2 and in Sect. 7.5, where also the related radiance uncertainty is presented.

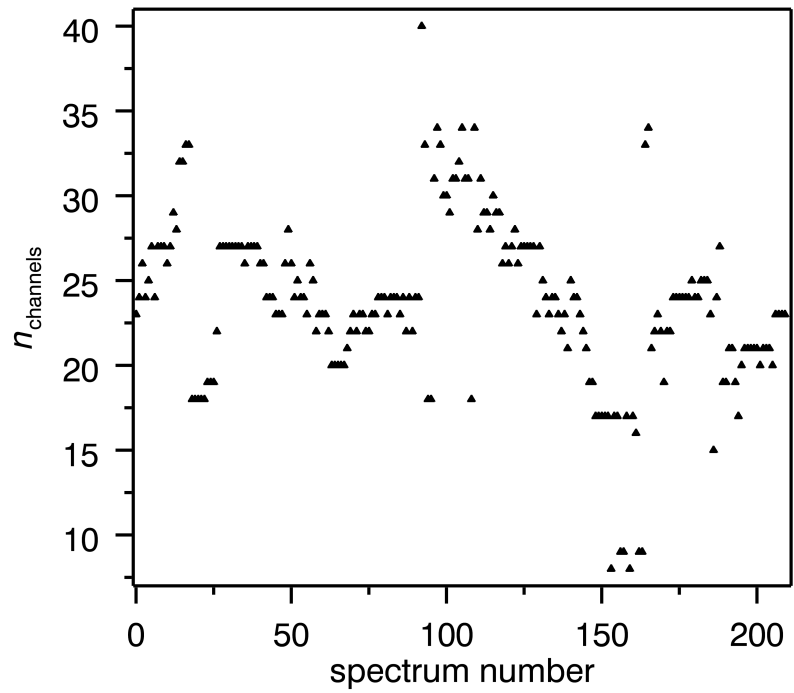


Figure 7.4: Number of spectral channels included in the IWV fit for the spectra of the FIR continuum data set. n_{channels} was chosen according to the minimum uncertainty criterion shown in Fig. 7.3.

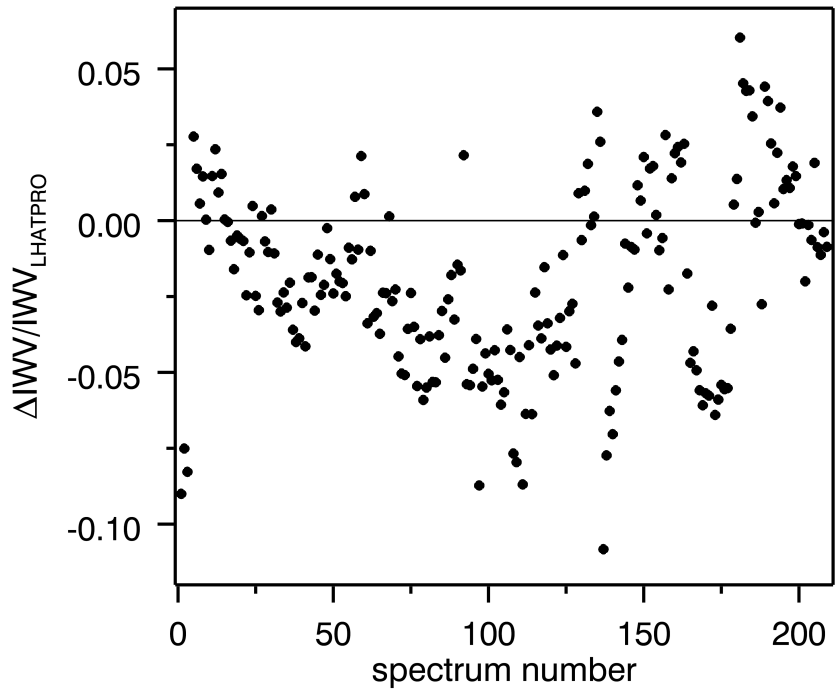


Figure 7.5: Relative adjustment $\Delta \text{IWV}/\text{IWV}_{\text{LHATPRO}}$ derived in the IWV fit for the spectra included in the FIR continuum data set.

Profile shape information on water vapor was taken from four-times-daily National Center for Environmental Prediction (NCEP) resimulation data. The reason for not using water vapor profiles from the LHATPRO microwave radiometer (Radiometer Physics, Germany; Rose et al., 2005) available on site is that a comparison of LHATPRO water vapor profiles with coincident NCEP resimulation profiles for the FIR continuum data set resulted in relatively large discrepancies, i.e. a mean precision (2σ) of 27.6 % and a mean bias of 20.4 %. We therefore use NCEP profiles throughout the closure study. However, a comparison with LHATPRO profiles is used in order to detect and discard atmospheric states in which NCEP fails to realistically cover spatiotemporal variability of water vapor (see Sect. 8.1). An estimate of the NCEP profile shape uncertainty based on a comparison with radiosonde profiles is given in Table 7.2 and derived in Sect. 7.5.

Temperature Profiles

Temperature profiles for the radiative transfer calculations were based on four-times-daily pressure-temperature-humidity profiles from NCEP interpolated to the time of the radiance measurement. Since the lowest atmospheric layer above the Zugspitze summit is certainly influenced by the mountain surface, deviations between the true temperature profile and NCEP are expected. In order to account for this effect, the NCEP profile was corrected for the lowermost 500 m above the Zugspitze summit. The correction is retrieved using the spectral radiance observed by the ER-AERI in the central part of the 15 μm band of CO_2 (i.e. 625–715 cm^{-1}). Because of the strong absorption, the measured radiance in this spectral region strongly correlates to the temperature of the environment close to the instrument. For this kind of boundary layer temperature inversion the retrieval scheme developed by Esposito et al. (2007) is used, which has successfully been utilized by a series of studies (Serio et al., 2008; Masiello et al., 2012; Liuzzi et al., 2014); a similar approach has been used by Rowe et al. (2006) and Rowe and Walden (2009). An estimate of the profile uncertainty based on a comparison with radiosonde profiles is given in Table 7.2 and derived in Sect. 7.5.

Columns of O_3 , CO_2 , CH_4 , and N_2O

Total columns of ozone are obtained from Brewer-Dobson soundings carried out at the nearby Hohenpeissenberg observatory of the German Weather Service (Köhler, 1995) with an accuracy of $\sim 1\%$ (Staehelin et al., 2003). The horizontal distance between Hohenpeissenberg (47.80°N , 11.02°E , 985.5 m a.s.l.) and the Zugspitze is ~ 40 km and the altitude difference was taken into account by correcting the measured ozone columns by a factor of 0.982 inferred from the ozone profile of the (midlatitude winter) US standard atmosphere.

Column-averaged mixing ratios of CO_2 , CH_4 , and N_2O (XCO_2 , XCH_4 , XN_2O) were inferred from solar FTIR measurements. One option is to use the Zugspitze solar FTIR which is at the same time used for the NIR radiance measurements (see Fig. 7.1). However, for practical reasons (beamsplitter change from KBr to CaF_2 necessary for switch between MIR and NIR trace gas measurements, but not possible via remote control) the NIR FTIR instrument operated at the nearby Garmisch site (47.48°N , 11.06°E , 743 m a.s.l.) within the Total Carbon

Table 7.3: Central wavelength and FWHM of the sun photometer (SSARA-Z) filters used for AOD analysis.

λ [nm]	FWHM [nm]
439.6	9.7
498.7	12.3
531.9	11.2
672.5	10.9
781.1	9.7

Column Observing Network (TCCON; www.tccon.caltech.edu, Wunch et al., 2011) has been used for routine operations.

The horizontal distance between Garmisch and Zugspitze is only \sim 8 km. The site altitude difference has been taken into account for CH_4 and N_2O because of the stratospheric slope of the mixing ratio profiles of these species. This has been performed by using the multi-annual mean ratio of column averaged mixing ratios retrieved from the Zugspitze and Garmisch NDACC solar FTIR measurements of 1.8 % (the underlying datasets are displayed in Fig. 1 of Sussmann et al., 2012). Uncertainties given in Table 7.2 were taken from the TCCON wiki (https://tccon-wiki.caltech.edu/Network_PolicyData_Use_PolicyData_Description#Sources_of_Uncertainty).

Aerosol Optical Depth

AOD can become comparably high to water vapor continuum optical depth in NIR window regions and thereby potentially hinder accurate continuum quantification from field experiments as pointed out e.g. by Ptashnik et al. (2015). Therefore, AOD has to be constrained precisely in order to enable continuum quantification in the wings of the strong NIR water vapor bands and within window regions. A great advantage of the Zugspitze site is that AOD is typically very low, i.e. the AOD for the Zugspitze dataset is about a factor of 10 lower than at typical lowland mid-latitude sites. The AOD levels encountered in our closure data set (data set description and selection criteria see Sect. 8.2) are in the range 0.0005–0.00075 at 2500 cm^{-1} and in the range 0.0024–0.0032 at 7800 cm^{-1} at airmass 1.

AOD was measured using the SSARA-Z (Sun-Sky Automatic Radiometer - Zugspitze) sun photometer (Toledano et al., 2009) developed by the Meteorological Institute of the University of Munich and set up at Schneefernerhaus (2675 m a.s.l., 680 m horizontal distance to the Zugspitze solar FTIR). The instrument disposes of 13 spectral channels from 340 to 1640 nm. Only information from 5 channels centered at 439.6 to 781.1 nm was used in the analysis. The exact filter wavelengths and full width at half maximum (FWHM) values of these channels are listed in Table 7.3. The reason for the channel selection is that in the ultra-violet (UV) to visible range, water vapor continuum absorption can be considered negligible compared to AOD, whereas for the NIR channels continuum absorption will lead to biased AOD results. The channels below 440 nm were excluded since the high influence of Rayleigh scattering in the UV leads to increased AOD uncertainties.

The data analysis of the SSARA-Z measurements was implemented similar to the approach outlined by Toledano et al. (2009). In detail, standard Langley calibration is used for cloud-free periods. Rayleigh scattering was accounted for using the formula given by Bodhaine et al. (1999). In the analysis, a Gaussian shape was assumed for the filter transmissivity curves. The influence of absorption by O_3 was subtracted as outlined in Guyemard (1995). NIR AOD was then deduced by assuming AOD wavelength dependence according to the Ångstrom relation:

$$\tau(\lambda) = b \cdot a^{-\lambda} , \quad (7.1)$$

where τ designates AOD. The Ångstrom exponent a and scaling b are determined by a fit to the UV/visible AOD measurements. More sophisticated descriptions of the AOD wavelength dependence such as the relation given by Molineaux et al. (1998) may be used instead of Eq. 7.1. However, the number of sun photometer wavelength channels included in our analysis is not sufficient to place tight constraints on the higher number of parameters used in such models. Furthermore, the very low AOD at Zugspitze leads to high relative errors in the sun photometer measurements, which removes the benefits of more advanced models compared to Eq. 7.1.

The following contributions were included in the calculation of the AOD uncertainty: the sun photometer measurements are affected by uncertainty in the radiance measurements. This uncertainty contribution was set according to the 2σ radiance measurement noise. The calibration uncertainty ensues from the uncertainty of the Langley fit. Additional uncertainty arises from the Rayleigh scattering correction, where central wavelength and FWHM errors of optical filters and atmospheric pressure errors contribute. The treatment of O_3 absorption is also prone to additional errors, due to filter parameter and O_3 column errors. In addition to these contributions, further uncertainty is induced by the fit to Eq. 7.1 that enables constraining the NIR AOD from the UV/visible measurements. The overall AOD uncertainty that ensues from these contributions for our data set at airmass 1 is < 0.0015 at 2500 cm^{-1} and < 0.0025 at 7800 cm^{-1} .

7.4 Radiative Transfer Calculations

Synthetic radiance spectra in the Zugspitze closure experiment were generated using the LBLRTM radiative transfer model (Clough et al., 2005). The atmospheric state necessary as an input to the model was set according to the measurements listed in Sect. 7.3. Parameters not constrained by measurements were set to the values given by the midlatitude winter US standard atmosphere. For spectral line parameters, the aer_v3.2 line list provided alongside the LBLRTM model was used.

The calculations were carried out for a 39-level atmosphere from observer height (2964 m a.s.l.) to 120 km altitude. The altitude grid was chosen in order to keep the error from discretization of the atmosphere in the calculations negligible compared to the remainder of the residual error budget (2.8% of total uncertainty for water vapor continuum retrieval windows). Synthetic radiance spectra were convoluted with a sinc-type instrumental line shape accounting for the

OPD_{max} relevant for the ER-AERI (see Knuteson et al., 2004b) and solar FTIR (see Sect. 7.2) measurements, respectively.

7.5 Uncertainty Analysis of Radiance Residuals

A meaningful interpretation of the spectral residuals derived in the closure experiment relies on a comprehensive residual uncertainty budget. For this purpose, systematic and 2σ statistical error estimates were set up for all significant individual uncertainty contributions. Radiance uncertainties were then calculated from input parameter uncertainties by multiplying them with the corresponding radiance derivatives. In the case of input profiles, state error covariance matrices were used. The radiance derivatives were calculated with the LBLRTM using the finite difference method, except for the T profile radiance derivative matrix, which is calculated using the LBLRTM built-in analytic Jacobian capability.

Uncertainty from Spectral Radiance Measurements

A first group of contributions to the uncertainty is associated with the AERI spectral radiance measurements. An estimate of the AERI measurement noise (see Fig. 7.10a) is automatically generated by the ER-AERI software within the radiometric calibration procedure according to the method established by Revercomb et al. (1988). This noise estimate was reduced by 50 % to account for the effect of the PCA filter applied to the spectra (see Sect. 7.2). Further radiance uncertainty of the ER-AERI measurements ensues from radiometric calibration errors. The calibration uncertainty estimate was set according to Knuteson et al. (2004b), who demonstrate this contribution to be less than 0.67 % (2σ uncertainty) of the ambient blackbody radiance. According to the same authors, the repeatability (precision) is 0.13 % (2σ). The resulting absolute ER-AERI radiance uncertainty is shown in Fig. 7.10a via the purple line, which - divided by the grey ambient blackbody Planck curve - reflects the cited 0.67-% relative calibration uncertainty.

Uncertainty contributions associated with the NIR radiance measurements are the solar FTIR measurement noise and the radiometric calibration uncertainty. The calibration uncertainty includes sources of uncertainty connected with the temporal stability of the calibration which are due to variation of the instrument's field of view on the solar tracker mirrors and ice buildup on the detector causing additional absorption. Figure 7.11 shows the overall 2σ calibration uncertainty (purple) which is between 0.6–1.7 % of measured radiance. A plot of individual contributions is shown in Fig. 6.5.

Uncertainty from Radiative Transfer Calculations

The second group of contributions to the residual uncertainty is associated with the synthetic spectra calculation and the corresponding input for spectroscopic line parameters and atmospheric state. A further uncertainty contribution associated with the LBLRTM ensues from

discretization of the atmosphere used for the calculation. As outlined in Sect. 7.4, the layering was adjusted in order to keep the discretization error negligible compared to the remainder of the uncertainty budget.

Uncertainty from Atmospheric State Measurements

The uncertainties in IWV in case of FIR and MIR closure experiments based on ER-AERI spectra is outlined below. For the FIR closure data set (detailed in Sect. 8.1), a mean IWV precision of 4.3% (2- σ) is achieved, while the mean IWV bias is 4.4%. The resulting IWV related radiance uncertainty is shown in Fig. 7.10 (blue).

An estimate of the statistical and systematic uncertainty of the IWV retrieval can be obtained based on the uncertainty of the ER-AERI vs. LBLRTM spectral residuals presented in Fig. 7.10. The statistical residual uncertainty is calculated as the quadratic sum of the AERI measurement noise and the statistical uncertainties related to calibration, T profiles, and water vapor profiles. The IWV fit uncertainty for single spectral points ensues as the statistical residual uncertainty divided by $\partial I / \partial IWV$. However, the IWV fit result is not derived from single spectral points but from an ensemble of points selected according to the criterion presented in Fig. 7.3. Therefore, the statistical IWV uncertainty for each spectrum results as the error-weighted mean of the single-point-contributions for all channels included in the ensemble. The mean statistical IWV uncertainty achieved for the FIR closure data set is 4.3% (2- σ).

The systematic IWV uncertainty can be derived in an analogous way. Systematic error contributions due to line parameters, ER-AERI calibration, T profiles, water vapor profiles, and columns of further species are summed up quadratically to calculate the systematic residual uncertainty. Using the same further analysis as outlined above for the statistical contribution, a mean systematic IWV uncertainty of 4.4% ensues for the FIR closure data set. In the case of the NIR closure using solar FTIR spectra, the uncertainty of the IWV retrieval (precision: 0.8%, bias: 1.1%) is provided in Schneider et al. (2012). The IWV-related radiance uncertainty in the NIR is shown in Fig. 7.11 (blue).

In addition to the total water vapor column, erroneous input for the shape of the water vapor profiles from NCEP leads to errors in the synthetic radiance. A conservative estimate for this was inferred from a comparison of the NCEP profiles with radiosonde measurements. This estimate is based on radiosonde data from a campaign performed close to the Zugspitze site between March–November 2002 (for details see Sussmann and Camy-Peyret, 2002, 2003; Sussmann et al., 2009). The campaign data set comprises a number of 181 pairs of radiosondes launched with a 1-hour time separation, and each radiosonde pair has been combined to a best estimate of the state of the atmosphere according to the formalism by Tobin et al. (2006). Subsequently, both NCEP profiles and sonde-based Tobin-best-estimate profiles were normalized by IWV analogous to the analysis in the later closure experiment (Sect. 8.1), and then profile differences were computed. The red line in Fig. 7.6 shows the mean difference profile. The profile shape bias of 1.7% given in Table 7.2 is just a simple proxy calculated from the mean of the moduli of the difference profile vector components. The statistical profile shape

uncertainty was set up via an error covariance matrix constructed from the difference profiles between NCEP and sonde-based Tobin-best-estimate profiles. This error covariance was used for the further statistical analysis of radiance uncertainty. Just to illustrate some properties of this covariance, the black error bars in Figure 7.6 show the 2σ statistical uncertainties of the difference profile (corresponding to the diagonal of the covariance). By calculating the mean of these error bars, one can derive a simple scalar proxy for the statistical profile uncertainty of 9.4 % (Table 7.2). Radiance uncertainties were then computed from the profile uncertainty contributions by multiplying these with the corresponding derivative matrix of radiance with respect to water vapor profile shape (see Fig. 7.7). This leads to the residual uncertainty shown in Fig. 7.10 (pink).

The temperature profiles used in the closure study are a composite of T profiles retrieved from the ER-AERI spectra for the altitude range between the Zugspitze up to ~ 3.5 km a.s.l. and a NCEP resimulation profile at higher altitude as described in Sect. 7.3. The uncertainty estimate for these composite profiles was constructed from the same radiosonde campaign data as for the water vapor profile analysis outlined above. To generate an estimate of the uncertainty, synthetic radiance spectra were calculated using all radiosonde-derived best-estimate T profiles from the campaign. The systematic part of the uncertainty was estimated by adding the ER-AERI calibration bias (0.66 %, see Table 7.2) to the synthetic radiance spectra. Then, the near-surface temperature profile retrieval described in Sect. 7.3 was applied to the modified radiances. Finally, the differences between our composite T profiles and the radiosonde-based best-estimate profiles from the campaign were calculated (red line in Fig. 7.8). Note, that the sign of the bias below 3.5 km a.s.l. (see Fig. 7.8) is arbitrary in the sense that it depends on whether the calibration bias is added or subtracted. The random uncertainty of the composite T profile was estimated by adding random error according to the statistical ER-AERI calibration uncertainty (0.13 %, Table 7.2) and ER-AERI noise (yellow line in Fig. 7.10) to the synthetic radiance spectra. Finally, the near-surface temperature profile retrieval described in Sect. 7.3 was applied to the modified radiances. An error covariance matrix estimate was then calculated from the difference of the radiosonde profiles to these composite T profiles. Radiance uncertainties were then calculated by multiplication with the corresponding radiance derivative matrix depicted in Fig. 7.9. The resulting overall radiance uncertainties are shown in Figs. 7.10 and 7.11 (green).

Line parameter uncertainties for water vapor and further trace gases were set according to the error codes given in the aer_v3.2 line list provided alongside the LBLRTM radiative transfer model. The uncertainty of each parameter was assumed to correspond to the mean of the error range specified by the error code value. Column uncertainties of further trace gases (see Table 7.2) are given by the TCCON specifications in the case of CO₂, CH₄ and N₂O and the combined Brewer-Dobson measurement uncertainty for O₃. The resulting radiance uncertainties are depicted in Figs. 7.10 and 7.11 (red and cyan).

An additional contribution ensues in the NIR from the AOD uncertainty, which is < 0.0015 at 2500 cm⁻¹ and < 0.0025 at 7800 cm⁻¹ at airmass 1 as detailed in Sect. 7.3. The resulting radiance uncertainty is shown Fig. 7.11 (grey).

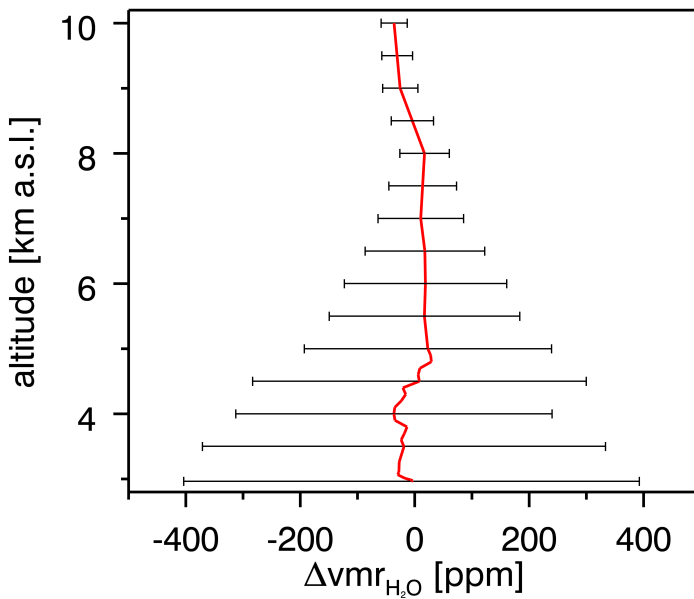


Figure 7.6: Uncertainty analysis of NCEP water vapor profile shape. Red is the mean difference between NCEP profiles normalized with respect to IWV and an ensemble of best-estimate profiles derived from pairs of radiosondes launched with a 1-h separation (also normalized for IWV). Black error bars indicate 2σ differences.

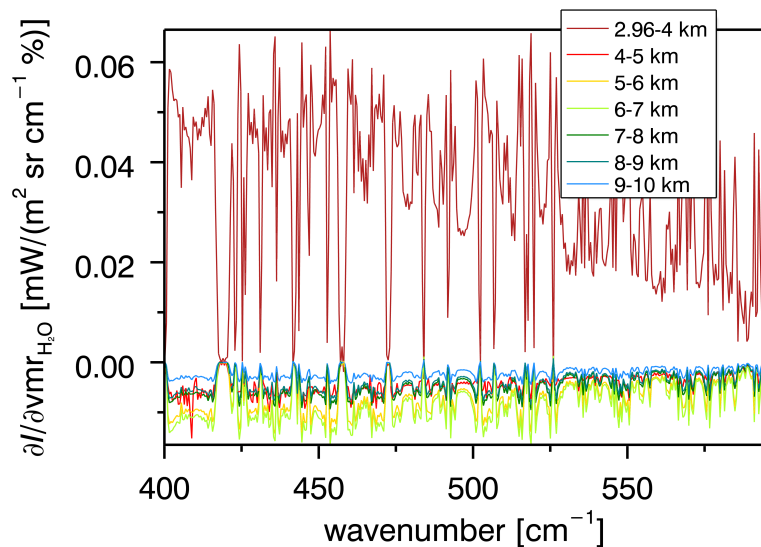


Figure 7.7: Derivative of surface downwelling radiance with respect to water vapor profile shape computed for the mean atmospheric state of the continuum retrieval data set. Color coding indicates the contributions from different altitude layers.

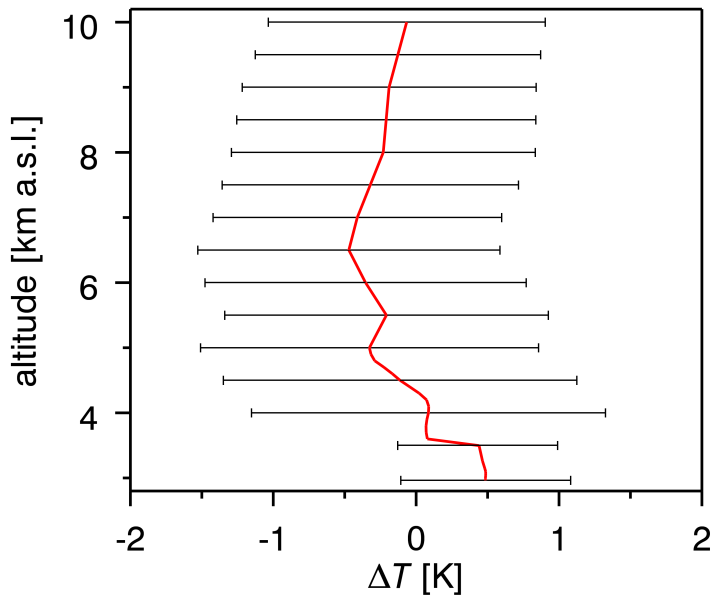


Figure 7.8: Uncertainty analysis of T profiles used in the closure experiment (composite of ER-AERI retrievals < 3.5 km and NCEP). Red is the mean difference between these composite profiles and an ensemble of best-estimate profiles derived from pairs of radiosondes launched with a 1-h separation. Black error bars indicate 2σ of the differences.

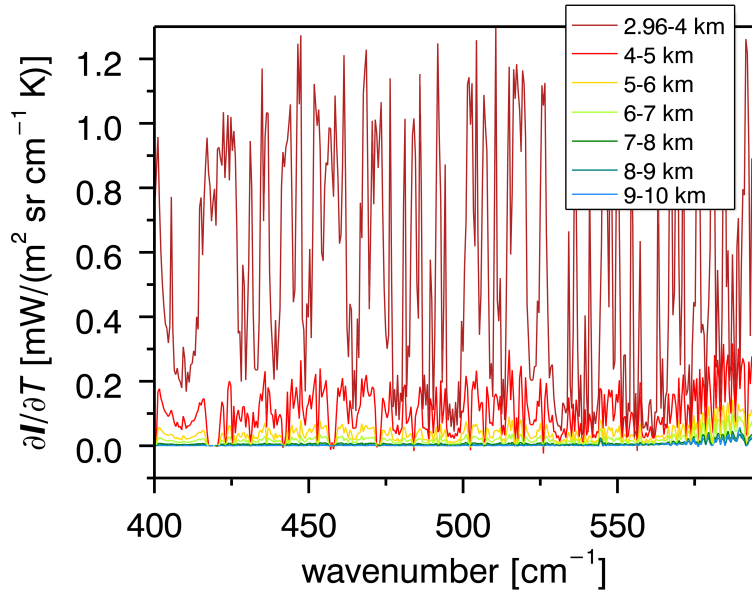


Figure 7.9: Derivative of surface downwelling radiance with respect to the T profile computed for the mean atmospheric state of the continuum retrieval data set. Color coding indicates the contributions from different altitude layers.

Total Uncertainty Budget

Figure 7.10 shows an estimate of the residual uncertainty in the FIR and MIR closure experiment using AERI spectra; the same is shown in Fig. 7.11 for the solar FTIR radiative closure experiment in the NIR. The individual uncertainty contributions presented above were added in quadrature to obtain the total residual uncertainty.

Figure 7.10a shows that the dominant contribution to the total uncertainty in the FIR is from water vapor line parameters, while T profile uncertainties dominate in the MIR. Exceptions from this overall tendency do exist and are shown in Fig. 7.10b as an example for the FIR where a dominant role of T profile uncertainties can be seen within saturated regions, e.g. around 420 cm^{-1} . However, such saturated regions are not included in the spectral micro-windows used for continuum quantification (Fig. 7.10c).

Uncertainty contributions to NIR radiance shown in Fig. 7.11 are dominated by varying contributions depending on wavelength. The overall uncertainty is dominated by water vapor line parameter uncertainties in the vicinity of the strong water vapor bands. The window regions in between are dominated by solar FTIR calibration uncertainties at low NIR wavenumbers but uncertainties due to AOD become an increasing and dominant contribution towards higher NIR wavenumbers. Exceptions are CH_4 or N_2O bands in the NIR, where the associate line parameter uncertainties dominate the overall uncertainty.

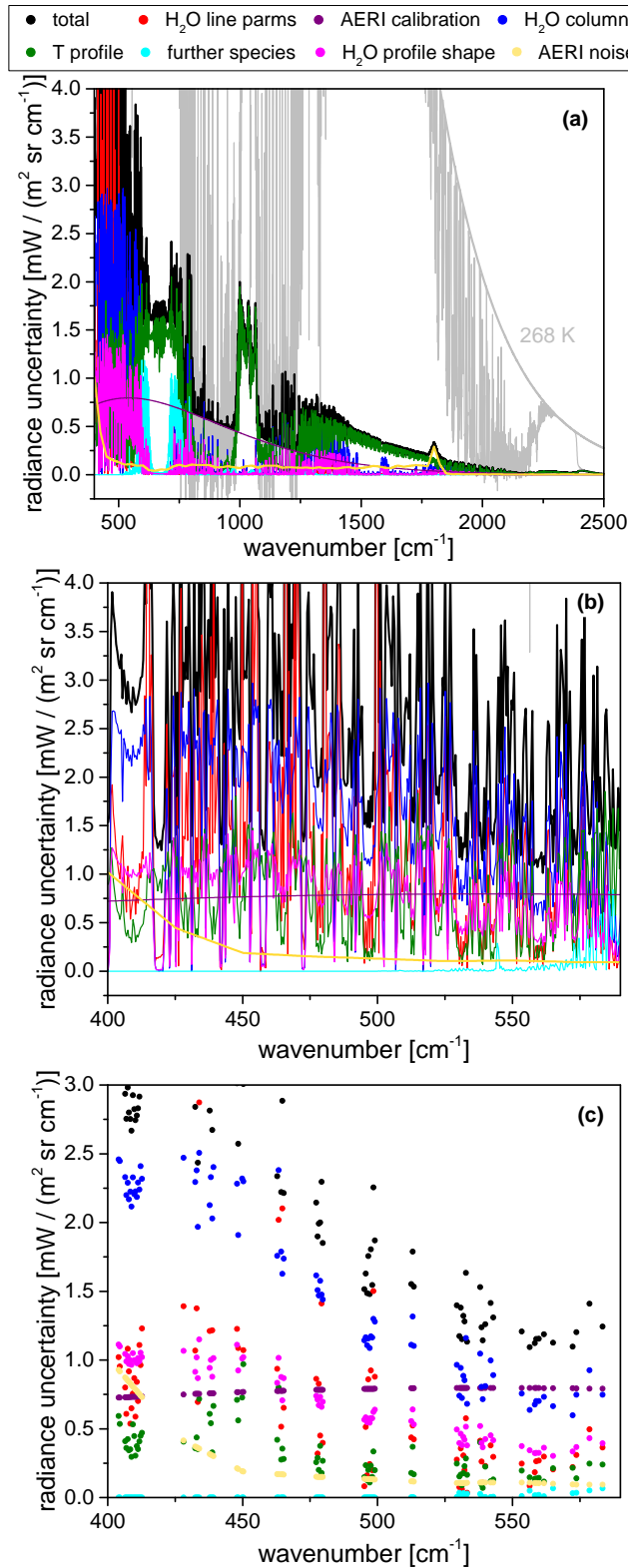


Figure 7.10: Residual uncertainty (2σ , relative to ambient BB radiance) of the FIR and MIR closure experiment for a single AERI thermal emission spectrum and for the mean atmospheric state of the closure data set (IWV = 1.6 mm, for more details see Sect. 8.1). (a) Individual error contributions (colors) to the total residual uncertainty (black). For reference, a calculated radiance spectrum (grey) for the mean atmospheric state is shown along with the ambient BB Planck curve. (b) Zoom of a) for the FIR part. (c) Same as b) but restricted to the spectral windows used for continuum quantification.

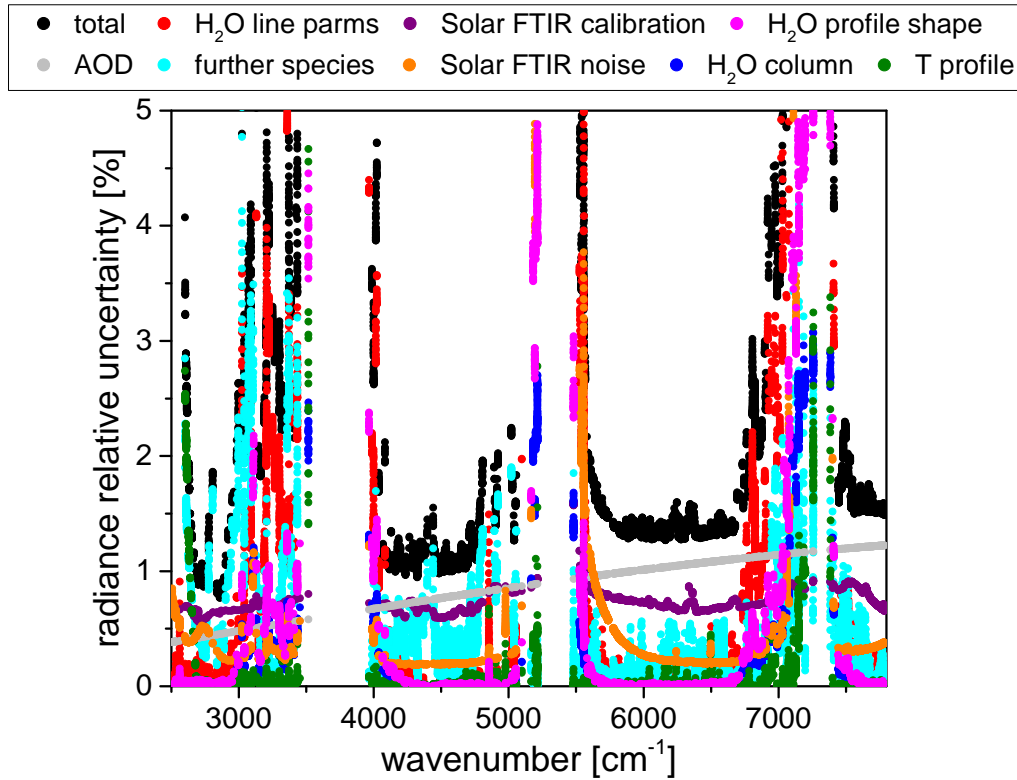


Figure 7.11: Residual uncertainty (2- σ , relative to measured solar radiance) of the NIR closure experiment for a single solar FTIR spectrum and for the mean atmospheric state of the closure data set (IWV = 2.3 mm, for more details see Sect. 8.2). The total residual uncertainty (black) results from contributions by water vapor line parameter uncertainties (red), IWV uncertainty (blue), temperature profile uncertainty (green), further trace gas column and line parameter uncertainties (cyan), AOD uncertainty (grey), solar FTIR calibration uncertainty (purple) and solar FTIR measurement noise (orange). Representation corresponds to the mean atmospheric state of the water vapor continuum quantification data set and the spectral windows used for continuum retrieval.

Chapter 8

Continuum Quantification from Radiative Closure Measurements

This chapter contains a description of the necessary steps to obtain FIR and NIR continuum results. The analysis outlined in this chapter starts out from the measured and synthetic spectra generated with the closure setup presented in Chapter 7.

Due to the influence of atmospheric emission in the FIR and NIR, this spectral range requires an iterative approach to quantify the water vapor continuum that will be presented in Sect. 8.1. For the NIR solar absorption spectra, thermal emission by the atmosphere can be neglected, which removes the need for an iterative approach (see Sect. 8.2).

8.1 Assessment of FIR Continuum

The closure setup presented in Chapter 7 enables to quantify the magnitude of the water vapor continuum in the FIR spectral range in the region $400\text{--}580\text{ cm}^{-1}$ based on a comparison of AERI radiance spectra and LBLRTM results (see Fig. 8.1a).

FIR Spectra Selection

The example analysis is based on measurements carried out in the December 2013–February 2014 period. Several selection criteria were applied to the ER-AERI measurements in order to avoid bias in the quantification of the water vapor continuum. Clear-sky spectra were selected based on a radiance threshold in the MIR atmospheric window where significant thermal emission occurs only under cloudy conditions. Namely, the mean radiance in the 829 to 835 cm^{-1} window was required to be less than the synthetic radiance in this window plus the ER-AERI calibration uncertainty presented in Sect. 7.5.

Due to the reduced number of suitable windows for continuum retrieval under moist atmospheric conditions, only spectra with $\text{IWV} < 5\text{ mm}$ were selected. Snow accumulation on

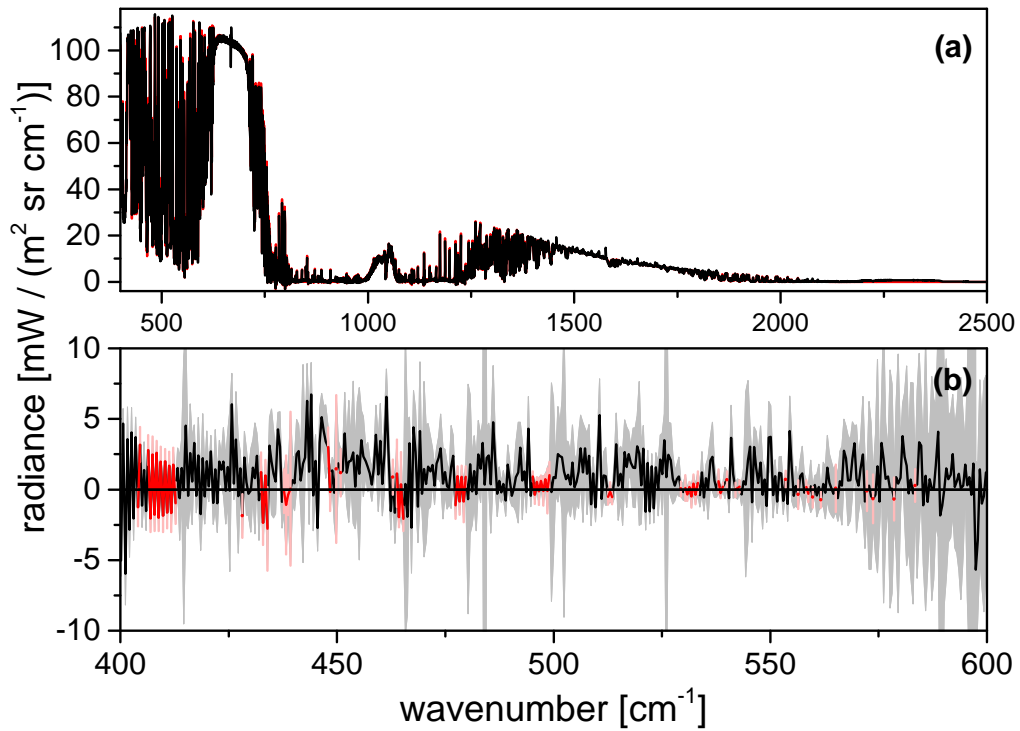


Figure 8.1: (a) Comparison of a measured AERI spectrum (black) recorded on 13 December 2013, 8:28 UTC and the corresponding synthetic LBLRTM spectrum (red). (b) Mean spectral residuals derived from the continuum retrieval data set (black) and residual uncertainty (grey). Spectral windows used for continuum retrieval are highlighted in red.

the LHATPRO may bias the measurements and can be detected based on the LHATPRO LWP measurements. Therefore, only spectra with $LWP < 100 \text{ g m}^{-2}$ were selected. NCEP reanalysis data is used to constrain water vapor profile shape in the closure experiment. Despite the low uncertainties of the NCEP water vapor profiles demonstrated in Sect. 7.5, significant deviations from the real profile shape are expected in rare cases. This is due to the limited (6 hourly) time resolution of the NCEP data and its inability to reproduce small-scale spatial variability of water vapor concentrations. In order to identify these cases, we excluded measurements from further analysis if the mean difference of NCEP vs. LHATPRO water vapor profiles exceeded the $1-\sigma$ uncertainty of the LHATPRO measurements presented in Sect. 7.3. These criteria lead to a continuum retrieval data set of 211 spectra, selected from 2787 spectra measured in December 2013–February 2014.

Window Selection

Spectral residuals, i.e. the difference between synthetic and measured spectra were calculated from the set of selected spectra. Figure 8.1 shows the mean residuals for our data set and their uncertainty according to the estimate provided in Sect. 7.5.

Accurate constraints on the water vapor continuum can only be derived from a number of spectral windows, whereas throughout the remainder of the spectrum the continuum does either not contribute significantly to the measured radiance or the residual uncertainty is too high. In order to select suitable windows, an estimate of the continuum uncertainty achievable in the closure experiment was determined by multiplying the residual uncertainty estimate (see Sect. 7.5) with the continuum Jacobian. The continuum Jacobian, i.e. the derivative of continuum magnitude with respect to measured downwelling radiance, was calculated via the finite difference method using the MT_CKD 2.5.2 model as a priori. For further analysis only windows in which the continuum uncertainty is less than 100 % above the minimum uncertainty in 10 cm^{-1} -wide bins were selected. The selected windows are highlighted in red in Fig. 8.1b.

Continuum Quantification Procedure

Continuum quantification is achieved via an iterative minimization of spectral residuals in the selected windows. Spectral residuals in the windows are interpreted to be due to inaccurate foreign continuum since the radiance contribution by the self continuum is assumed to be negligible given the spectral range and the dry atmospheric conditions. Mean adjusted continuum coefficients are calculated in 10 cm^{-1} -wide bins to reduce influence of measurement noise and ILS uncertainty on the results.

The individual analysis steps comprise a determination of the spectral residuals in the selected windows and subsequent adjustment of the continuum according to these results and the continuum Jacobian. Synthetic radiance is then recalculated using the adjusted continuum input. This process is repeated iteratively until the mean spectral residuals in all bins are below 10 % of the residual uncertainty estimate.

8.2 NIR Continuum Determination

Setup of the NIR Closure Experiment

The closure experiment relies on a quantitative comparison of measurements of spectral radiance with synthetic spectra calculated using the line-by-line radiative transfer model (LBLRTM, Clough et al., 2005). Water vapor continuum absorption is then quantified via the spectral residuals, i.e. the difference between simulated and measured spectra. The instruments used in the Zugspitze radiative closure experiment and the related uncertainties are described in detail in Chapter 7.

The atmospheric state at the time of the radiance measurements is required as an input to the LBLRTM radiative transfer calculations. To enable accurate quantification of the water vapor continuum from spectral residuals, the atmospheric state has to be constrained precisely using a number of additional measurements. The state measurements used in the NIR closure differ from the FIR/MIR setup presented in Sect. 7.1 in the following aspects: Vertically integrated water vapor (IWV) constitutes the key input parameter and is derived directly from the solar FTIR spectra (e.g. Sussmann et al., 2009; Schneider et al., 2012). For precise AOD constraints sun photometer measurements in 12 channels between 339–1640 nm of the SSARA-Z instrument developed by the Meteorological Institute of the University of Munich (Toledano et al., 2009) and set up at Schneefernerhaus (2675 m a.s.l., 680 m horizontal distance to the Zugspitze solar FTIR) were used. The AOD retrieval is based on Toledano et al. (2009) and outlined in detail in Sect. 7.3.

Method Overview

The aim of this study is to constrain the NIR water vapor continuum absorption under atmospheric conditions. The analysis relies on the radiative closure experiment setup at the Zugspitze observatory that is described in detail in Sect. 7.1. Generally, radiative closure experiments comprise a quantitative comparison of spectral radiance measurements to synthetic spectra. The strategy for water vapor continuum quantification employed in this study relies on radiometrically calibrated solar FTIR spectra in the 2500 to 7800 cm^{-1} -range.

Spectra were recorded with the solar FTIR instrument described in Sect. 7.2, using no optical filter, a spectral resolution of 0.02 cm^{-1} (resolution is defined as $0.9/(2 \cdot \text{OPD}_{\text{max}})$), and averaging over 4–8 scans which leads to a 75–150 s repeat cycle per spectrum. The measured spectra are radiometrically calibrated by means of the calibration method outlined in Chapter 6. Briefly, the calibration approach relies on Langley calibration in suitable spectral windows with little atmospheric absorption. In addition to the Langley technique that enables highly accurate calibration in selected windows, the shape of the calibration curve between the windows is constrained using spectral radiance measurements of a high-temperature blackbody source. The calibration uncertainty achieved with this novel method is 1–2 % (2σ) throughout the spectral range considered.

Synthetic radiance spectra are generated using the LBLRTM radiative transfer model. The atmospheric state used as an input to the calculations was set based on the measurements described in Sect. 7.3. Given the calibrated spectral radiance measurements and the synthetic spectra, radiance residuals $\Delta \mathbf{I}$ can then be calculated for a set of spectra selected according to the criteria presented in Sect. 8.2.

$$\Delta \mathbf{I} = \mathbf{I}_{\text{FTIR}} - \mathbf{I}_{\text{LBLRTM, no continuum}} \cdot e^{-\text{AOD}} , \quad (8.1)$$

where \mathbf{I}_{FTIR} designates the radiometrically calibrated solar FTIR spectra, $\mathbf{I}_{\text{LBLRTM, no continuum}}$ the synthetic LBLRTM spectra not including continuum absorption and AOD the aerosol optical depth. Continuum optical depth τ_{cont} is calculated from the spectral residuals as follows:

$$\tau_{\text{cont}} = -\ln\left(\frac{\Delta \mathbf{I}}{\mathbf{I}_{\text{LBLRTM, no continuum}} \cdot e^{-\text{AOD}}} + 1\right) . \quad (8.2)$$

After calculation of the continuum OD, absorption coefficients were derived from these results. The continuum OD τ_{cont} is linked to the continuum absorption coefficient \mathbf{k}_{cont} as follows

$$\tau_{\text{cont}} = m \cdot \int_{h_{\text{obs}}}^{\infty} \mathbf{k}_{\text{cont}}(T, n_{\text{wv}}, n_{\text{air}}) n_{\text{wv}} dh , \quad (8.3)$$

where m designates the relative airmass, h_{obs} the altitude of the observing instrument, n_{wv} the water vapor number density, and n_{air} the dry air number density.

The separation of \mathbf{k}_{cont} in the self and foreign continuum contributions described in Sect. 1.3 from atmospheric measurements is challenging. In principle, an assignment to self and foreign continuum is possible using a large set of measurements covering a wide range of atmospheric conditions, i.e. IWV and temperature. However, the available data does not permit such an assignment given the sensitivity of our setup as will be discussed in Sect. 11.2. Therefore, in the following, continuum strength is characterized using the mean continuum absorption coefficient $\bar{\mathbf{k}}_{\text{cont}}$, defined as follows:

$$\bar{\mathbf{k}}_{\text{cont}} = \frac{\int_{h_{\text{obs}}}^{\infty} \mathbf{k}_{\text{cont}}(T, n_{\text{wv}}, n_{\text{air}}) n_{\text{wv}} dh}{\int_{h_{\text{obs}}}^{\infty} n_{\text{wv}} dh} = \frac{\mathbf{k}_{\text{cont}}}{m \cdot \text{IWV}} \quad (8.4)$$

Low-uncertainty constraints on $\bar{\mathbf{k}}_{\text{cont}}$ can only be placed in a number of spectral windows. The selection of such suitable windows is outlined below. The continuum results for each spectrum were computed as the median of $\bar{\mathbf{k}}_{\text{cont}}$ in all selected spectral windows within 10 cm^{-1} -wide bins. Finally, an error-weighted mean of $\bar{\mathbf{k}}_{\text{cont}}$ was calculated from the set of 52 spectra selected according to the criteria listed below. The uncertainty estimate of the continuum results is presented in the following section.

Uncertainty Estimate

An interpretation of the residual OD and assignment to causative absorption processes requires a comprehensive uncertainty budget of the closure experiment. The uncertainty estimate of

our experimental setup is described in detail in Sect. 7.5 except for contributions only relevant for the NIR closure measurements. The total residual uncertainty and its various contributions are also shown in Fig. 7.11. A description of the NIR-specific contributions and a brief outline of the remaining sources of uncertainty are given below. All uncertainty values are quoted on 2σ confidence level.

- i. Absorption line parameter uncertainties of water vapor and other absorbing species. These uncertainties were set to the mean value of the uncertainty range specified by the error codes provided in the line parameter file (aer.v3.2) provided alongside the LBLRTM model. Line parameter uncertainties are the dominant contribution to the error budget within absorption bands.
- ii. A further significant contribution to the error budget results from the IWV measurement uncertainty. The IWV precision was set to 0.8 %, the bias to 1.1 % according to Schneider et al. (2012). The uncertainty resulting from NCEP water vapor profile shape errors was estimated using a comparison of NCEP profiles to radiosonde data (see Sect. 7.5 for details).
- iii. The OD uncertainty resulting from NCEP temperature profile errors was deduced from a temperature error covariance matrix estimate for the NCEP resimulation profiles. The error covariance matrix estimate was constructed from the comparison of coincident NCEP profiles to a radiosonde campaign conducted at the site (see Sect. 7.5 for details).
- iv. Column uncertainties for further trace gases (e.g. CO₂, CH₄, N₂O, and O₃) are also included in the uncertainty estimate. The respective column accuracies are listed in Table 7.2.
- v. The AOD uncertainty is of crucial importance for the OD uncertainty budget in the window regions. As outlined in Sect. 7.3, the AOD uncertainty at airmass 1 is < 0.0025 for the closure data set throughout the 2500 to 7800 cm⁻¹-range.

The uncertainty contributions (i) to (v) listed above are linked to the accuracy of the atmospheric state input for LBLRTM calculations. Aside from that, an additional group of error contributions stems from the solar FTIR spectral radiance measurements:

- vi. The radiance uncertainty due to the radiometric calibration is about 1–2 % and is described in detail in Chapter 6.
- vii. A further uncertainty contribution results from the solar FTIR measurement noise. It is determined directly from solar FTIR spectra and is among the few uncertainty contributions in the closure experiment of strictly statistical character. It is therefore largely reduced by taking mean results from a larger set of spectra.
- viii. Ice layer formation on the liquid nitrogen cooled InSb detector can occur in case of leaks in the detector's vacuum enclosure. Ice formation leads to additional absorption in

certain spectral regions, most notably in the 3000 to 3400 cm^{-1} -range. The uncertainty contribution by varying ice absorption was estimated using lamp spectra routinely recorded with the solar FTIR. Variations in ice absorption during the time period covered by the experiment can be detected as a change of the ratio of measured signal outside and inside the ice absorption band. The maximum variation of this ratio detected in the lamp spectra (1.6 %) was taken as an estimate of the error due to ice absorption.

- ix. Only a fraction of the solar tracker mirrors is covered by the instrument's field of view (FOV). Due to non-ideal alignment of optical elements, the exact location of the area observed by the instrument on the mirror changes depending on the azimuth and elevation of the instrument's line of sight. The reflectivity of the tracker mirrors features spatial inhomogeneity due to dirt and aging effects. In combination with the moving area covered by the FOV, this results in a variation in measured radiance which leads to spurious variations in the measured OD. An estimate of this uncertainty contribution can be gained using an outgoing laser beam aligned with the instrument's optical axis that enables constraining the mirror area covered by the FOV depending on the instrument's azimuth and elevation. A detailed description of this analysis is given in Sect.6.5.

NIR Spectra Selection

Spectra included in the analysis were recorded under cloud-free conditions in the December 2013–February 2014 period. Due to inaccuracies in the airmass calculation at high solar zenith angle, airmass was required to be below $m = 9.0$.

In Sect. 6, a source of radiance error in the solar FTIR measurements due to the pointing variation on the tracker mirrors was outlined including an estimate of this contribution. For spectra included in the closure data set, this uncertainty contribution was requested to be negligible compared to other sources of uncertainty, in detail the selection threshold was set to a maximum radiance error of 0.1 %. These selection criteria lead to a final dataset of 52 selected solar FTIR spectra covering an I WV range from 1.4 to 3.3 mm for which the continuum results will be presented in Chapter 11. The mean atmospheric state of the closure data set is listed in Table. 11.2.

Micro-window selection

To select suitable windows for continuum quantification, a number of selection criteria were applied to the spectra. Several criteria make use of upper or lower envelopes to the spectra, which were constructed as follows: The upper/lower envelope is defined as the linear interpolation between the highest/lowest values encountered within each 10 cm^{-1} -wide wavenumber bin. In detail, the following filtering criteria were applied to the spectra:

- i. To avoid spectral regions affected by line absorption, only the spectral points with the lowest OD compared to the surrounding spectral region were used. In detail, only points

for which the OD exceeds the lower envelope by less than the 2σ OD uncertainty were used.

- ii. Regions around solar lines were excluded. This was implemented as an exclusion of all points for which the extra-atmospheric solar radiance is more than 0.5 % below the upper envelope.
- iii. Only regions with low OD uncertainty are included. Therefore, points less than 10 % above the lower envelope to the uncertainty are selected.
- iv. In order to avoid biases of the retrieved continuum due to measurement noise, only regions with a signal-to-rms-noise ratio $s/n > 5$ were included.

The selection thresholds cited above were adjusted in order to provide sufficiently dense coverage with selected points while maintaining optimum selection quality. Different experimental setups may therefore require different selection threshold values. The final continuum OD results were computed as the median value of all selected spectral points within 10 cm^{-1} -wide bins.

Part IV

Results

Chapter 9

Pointing Error Correction Results

In this chapter, the results of the mispointing determination and correction applied to the Zugspitze solar FTIR system according to the method described in Chapter 5 are presented. The significant impact of the mispointing is demonstrated exemplary using time series of column-averaged methane mixing ratio (XCH_4) measured at Zugspitze. A validation of the correction results is presented based on trend analysis of XCH_4 in comparison with measurements from the nearby Garmisch instrument. The content of this chapter has been partly adapted from the related publication by Reichert et al. (2015).

9.1 Results and Validation via Methane Trend Analysis

The time interval considered in this analysis ranges from April 2006 until March 2015. This time interval was chosen based on three criteria: it coincides with the phase of renewed increase of atmospheric CH_4 concentrations (e.g. Sussmann et al., 2012). Furthermore, the interval includes the most up-to-date measurements available. The last criterion is that the interval length is a multiple of a one-year period, which is crucial for avoiding bias in the trend analysis.

The time series of mispointing in spectrometer coordinates and the zenith component of the mispointing in sky coordinates is shown in Fig. 9.1. The mean mispointing in zenith direction over the measurements made in the April 2006 to September 2012 time interval, which corresponds to the optics setup shown in Fig. 5.6, is $0.024 \pm 0.001^\circ$. Within the September 2012 to September 2014 interval (optics setup shown in Fig. 5.6a and b and quadrant diode) the mean mispointing is $-0.063 \pm 0.005^\circ$, and for the October 2014–March 2015 interval (optics setup shown in Fig. 5.6a and b and Camtracker) it is $0.024 \pm 0.008^\circ$.

The mispointing determination scheme relies on the basic assumption of approximately constant mispointing within each time bin. The validity of this assumption can be evaluated as outlined in Sect. 5.3, namely by analysis of the intra-bin scatter of mispointing results. Throughout the September 2012 to September 2014 time interval, the median of the scatter of mispointing results within each time bin was only 46 % of the mispointing vector norm in spectrometer coordinates, which means that the assumption of constant mispointing within

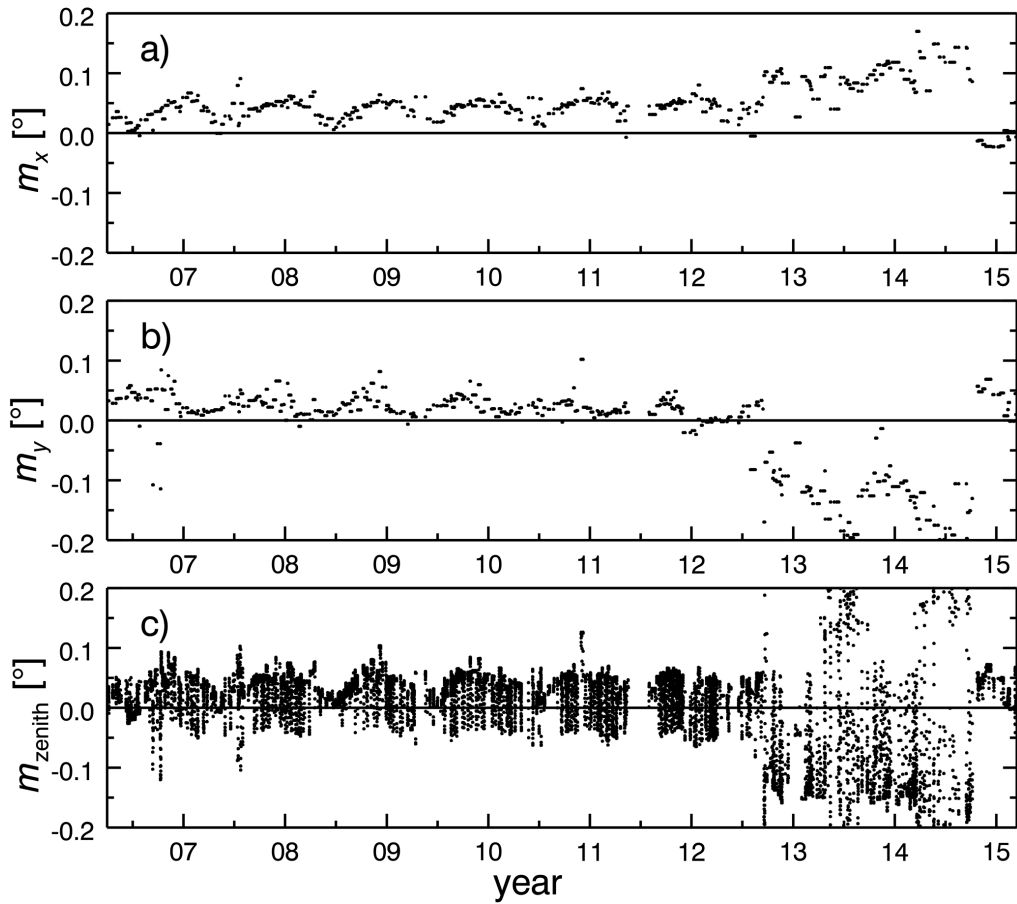


Figure 9.1: Mispointing results determined from Zugspitze measurements. **(a)** x component of mispointing in spectrometer coordinates. **(b)** y component of mispointing in spectrometer coordinates. **(c)** Zenith component of mispointing in sky coordinates.

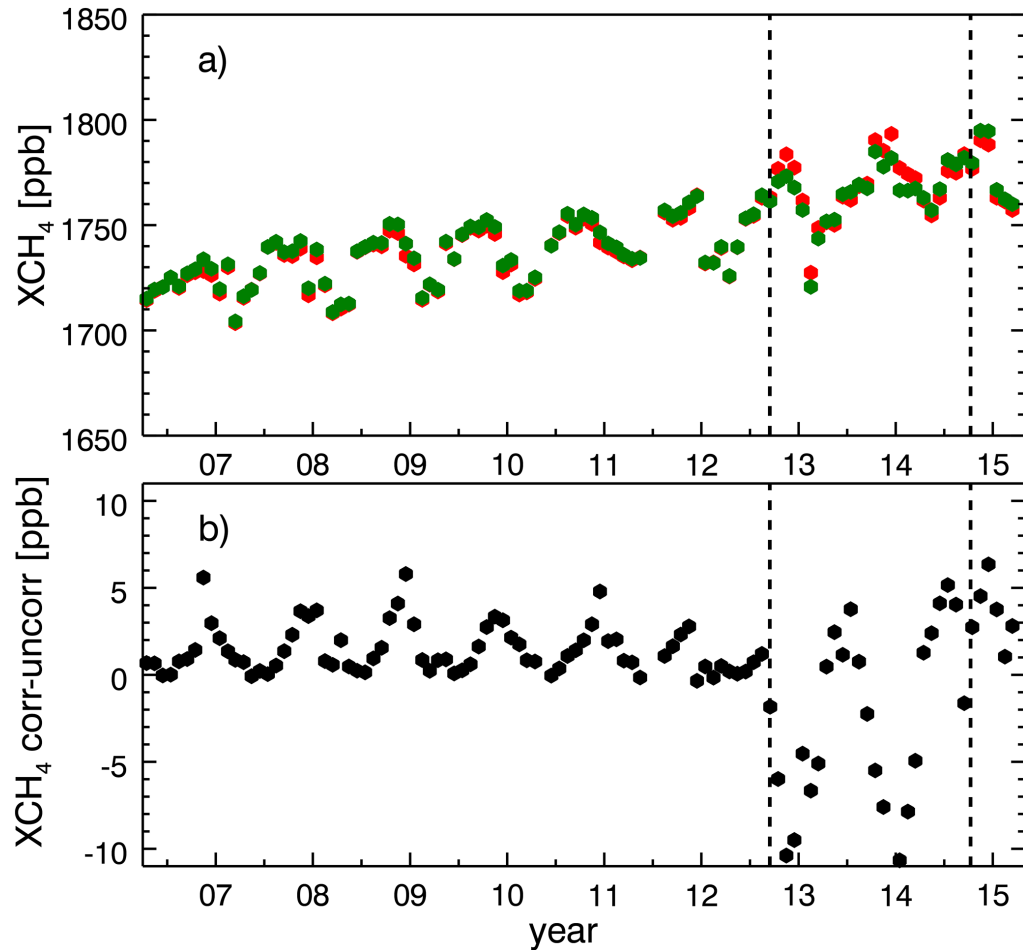


Figure 9.2: (a) Comparison of a posteriori-corrected (green) and uncorrected (red) Zugspitze XCH_4 monthly mean time series. (b) Time series of differences between a posteriori-corrected and uncorrected XCH_4 monthly means.

each time bin is appropriate and leads to a meaningful trace gas column correction. For the April 2006–September 2012 and October 2014–December 2014 phases, the intra-bin mispointing scatter corresponds to 108 and 152 % of the mispointing vector norm in spectrometer coordinates, respectively. Therefore, the basic assumption of constant mispointing is only poorly fulfilled in these phases and in general for the Garmisch instrument. This is due to the fact that the mispointing values in these phases were generally very small, which makes a mispointing determination with small relative error challenging. However, due to the small mispointing values, the mispointing correction has only very minor influence on the XCH_4 values in these time intervals. The Zugspitze and Garmisch instruments are likely to be well representative for standard NDACC and TCCON instruments. Therefore for ideally configured NDACC and TCCON systems, a mispointing correction is unlikely to lead to significant accuracy improvements. However, for non-standard or poorly aligned systems such as the Zugspitze instrument in the 2012–2014 phase, the correction leads to major quality improvements.

The use of the a posteriori correction method presented in Sect. 5.3 instead of the full a priori correction results in a 5 % bias in the zenith component of the mispointing for the Zugspitze measurement time series. This corresponds to only ~ 0.02 % bias in XCH_4 . Therefore, the a posteriori method can be considered to provide a fair approximation to the a priori results that has the advantage of not having to repeat the trace gas retrieval procedure after the mispointing determination.

In conclusion, the errors that result from the approximations made in the a posteriori method are negligible for most typical applications. The benefit of the a priori correction approach is that also the ray tracing in the forward spectral calculations in the retrieval is performed more accurately according to an improved knowledge of the true zenith angle. While this optional a priori correction approach leads only to minor improvements in terms of the total vertical column result, the a priori correction approach should be preferred if the retrieved target product is the trace gas profile shape (because of the more realistic ray tracing for each atmospheric layer).

Figure 9.2a shows a comparison of the corrected and uncorrected Zugspitze time series of XCH_4 monthly means for the phase of renewed methane increase since 2006. In Fig. 9.2b, the mispointing correction applied to the original time series is shown. The mean of XCH_4 correction over all measurements made in the time interval most affected by the mispointing (September 2012–September 2014) is -2.82 ± 2.08 ppb.

The mispointing results are validated by means of methane trend analysis. To perform this analysis, monthly means are calculated from the uncorrected and corrected XCH_4 time series. The trend analysis is performed as described in Gardiner et al. (2008) and Sussmann et al. (2012). In summary, all months with $n > 7$ measured spectra are included in the analysis. We then calculate monthly means and subtract the mean annual cycle fitted as a third order Fourier series from the time series of XCH_4 monthly means. Finally a trend is fitted to the deseasonalized time series. The trend uncertainty is determined by means of bootstrap reanalysis.

Table 9.1 shows the Zugspitze XCH_4 trend for the April 2006–March 2014 time interval and its 95 % confidence interval. Due to the major perturbations in the pointing accuracy in the

Table 9.1: XCH_4 trend [ppb yr^{-1}] for the April 2006–March 2015 time interval and corresponding 95 % confidence intervals; Zugspitze and Garmisch sites, uncorrected, a posteriori and a priori corrected.

	uncorrected	a posteriori corrected	a priori corrected
Zugspitze	6.45 [5.84, 7.04]	6.07 [5.55, 6.59]	6.08 [5.56, 6.60]
Garmisch	5.22 [4.77, 5.65]	5.20 [4.74, 5.64]	5.19 [4.74, 5.63]

Table 9.2: Bias of XCH_4 monthly means between Garmisch and Zugspitze measurements and corresponding 95 % confidence intervals. Results are presented for time intervals with different optical configurations and both a posteriori mispointing-corrected and uncorrected measurements.

time interval	Sep 2010–Aug 2012	Sep 2012–Oct 2014	Nov 2014–Mar 2015
bias uncorrected [%]	2.04 ± 0.18	1.46 ± 0.27	2.24 ± 0.37
bias a posteriori-corrected [%]	1.96 ± 0.19	1.60 ± 0.19	2.05 ± 0.36

September 2012–September 2014 interval (Fig. 9.2), the uncorrected Zugspitze trend is no longer consistent with the trend determined from measurements at the nearby Garmisch site. (Note, trend consistency could be shown for the time period before September 2011, see Sussmann et al. (2012). However, applying mispointing correction restores the consistency of Zugspitze and Garmisch trend results for the whole time series. This holds both for a posteriori-corrected and a priori-corrected results. As outlined in Sect. 9.2, mispointing correction also restores consistency in the bias between the Zugspitze and Garmisch XCH_4 monthly means for the phases with differing optical configurations.

9.2 Verification of Zugspitze Corrections via Comparison to Garmisch Methane Soundings

Due to the lower elevation of the Garmisch site and the decrease of methane concentration with increasing altitude, the XCH_4 values measured at this station are generally higher than at the Zugspitze site. Since the mean shape of the methane number density profile is not expected to vary significantly over the time interval considered in this study, the relative bias between the Zugspitze and Garmisch values is expected to be consistent for different optical configurations.

Table 9.2 shows the mean of XCH_4 monthly mean bias over the following time intervals: September 2010–August 2012, i.e. the two-year period before the optics configuration was changed. Further intervals include September 2012–October 2014, i.e. the approximately two-year period with changed optics and November 2014–March 2015, i.e. the time interval since the setup of the Camtracker system. As visible in Table 9.2, the bias results are not consistent for the three phases for the uncorrected measurements. However, applying the a posteriori mispointing correction results in consistent bias values for all three phases.

Chapter 10

Solar FTIR Radiometric Calibration Results

This chapter entails the results of the radiometric calibration method for solar FTIR spectra presented in Chapter 6. A validation of the calibration results and the corresponding uncertainty estimate is performed by investigation of calibration self-consistency and a comparison of calibrated spectra to radiative transfer model calculations.

Both validation efforts confirm the calibration uncertainty estimate. The calibration accuracy achieved with the combined method therefore enables the use of NIR solar absorption spectra for water vapor continuum quantification, and the corresponding results will be presented in Chapter 11.

10.1 Calibration Curve

The combined calibration curve calculated according to Eq. 6.3 from blackbody measurements made on 24 February 2014 and Langley measurements made on 13 December 2013 is shown in Fig. 10.1. The calibration curve determined from the Langley measurements made on 12 December 2013 is extensively consistent with the results presented in Fig. 10.1, as will be discussed in the following section.

The calibration scheme was implemented in the spectral range 2500 to 7800 cm^{-1} . At lower wavenumber values, thermal emission from the instrument itself becomes non-negligible. Therefore, alternative methods such as the widely used method introduced by Revercomb et al. (1988) are more suitable for calibration in this spectral range. The proposed new method can, however, be implemented with minor changes in the spectral range beyond 7800 cm^{-1} . Substitution of the solar FTIR detector and beam splitter (InGaAs detector and CaF_2 beam splitter instead of InSb/KBr) allows for an extension of the calibration range up to about 9000 cm^{-1} , while the use of a higher temperature blackbody source or standard lamp enables calibration at even higher wavenumber values until the visible spectral range.

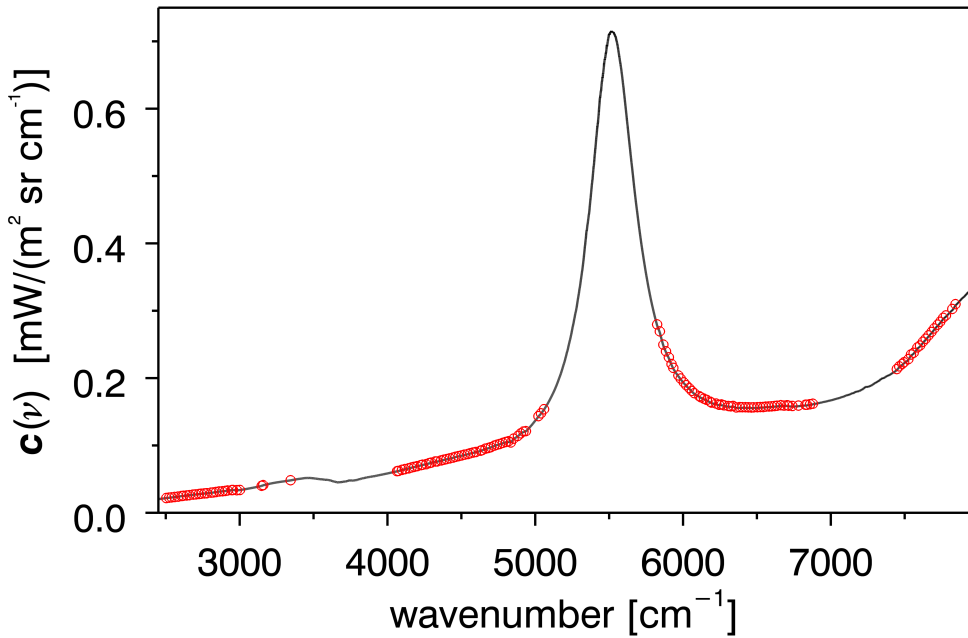


Figure 10.1: Combined calibration curve (black line) and selected Langley calibration points (red circles) for the Langley measurements made on 13 December 2013 in combination with blackbody measurements made on 24 February 2014.

10.2 Validation of Results

Self Consistency

A first method to validate the calibration results and the associated error estimate is to investigate the self-consistency of different calibration cases, i.e. the reproducibility of the calibration. The self-consistency of blackbody measurements is presented in Sect. 6.5. This result is then used as an estimate of the blackbody-related contribution to the total calibration uncertainty. As outlined in Sect. 6.5, this uncertainty contribution does not exceed 1.5 % throughout the spectral interval considered for calibration. The reproducibility of the Langley results is estimated by comparing the Langley measurements made on 12 December 2013 with the ones made on 13 December 2013. As shown in the Fig. 10.2a, the calibration curves determined from those two Langley measurements typically differ by less than 1 % outside absorption bands. In regions with sparse coverage of Langley points, i.e. within water vapor absorption bands, differences are typically around 1.5 %. Throughout 91.1 % of the calibration spectral range (2500 to 7800 cm^{-1}), the calibration curves are consistent within the calibration uncertainty estimate of Sect. 6.5 (grey shaded area in Fig. 10.2a). This extensive consistency consolidates the validity of the error budget presented in Sect. 6.5.

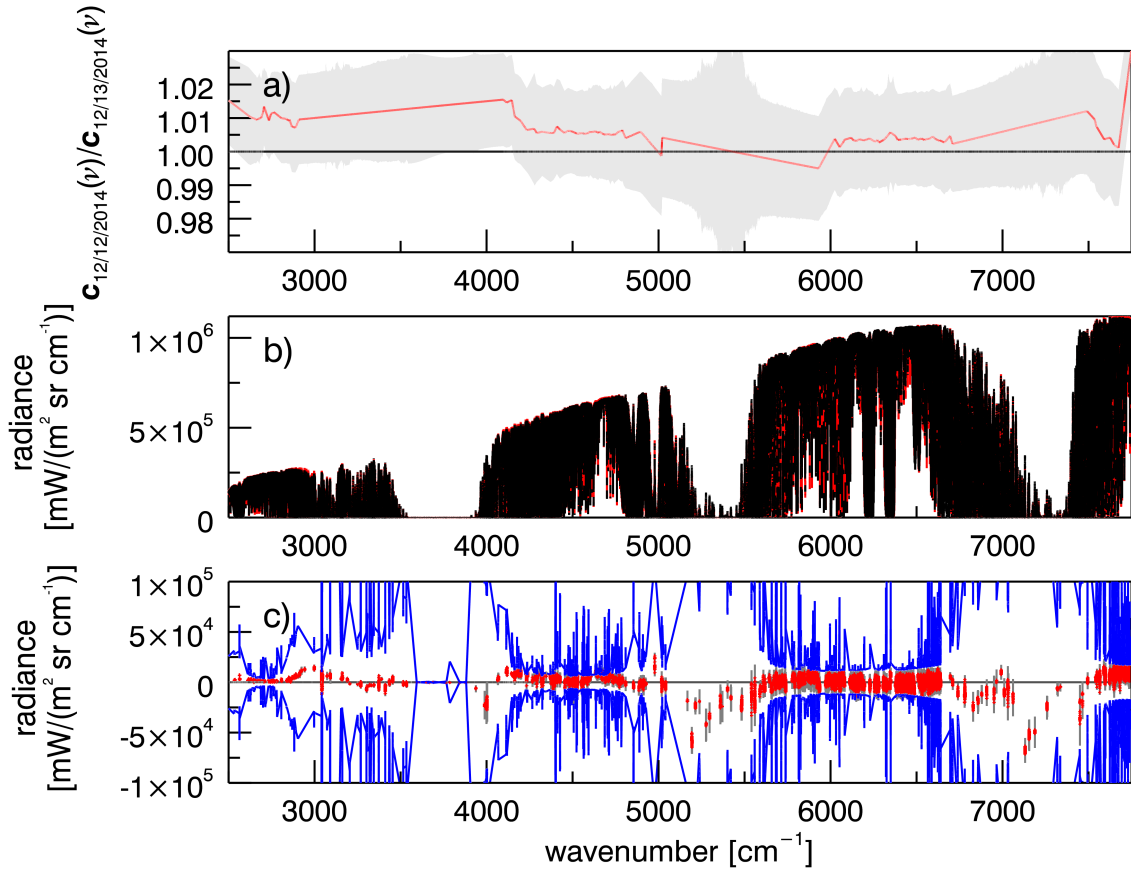


Figure 10.2: Validation of calibration results. a) Ratio of 12 December 2013 and 13 December 2013 results (red line) and 2σ uncertainty estimate (grey shaded area). b) Mean measured (black) and synthetic (red) radiance for the validation dataset. c) Mean residual (red dots) and standard deviation of residuals (grey shaded area) for the validation dataset outside spectral lines in comparison with the 2σ residual uncertainty estimate (blue line).

Comparison to Model Results

The validity of the calibration error estimate provided in Sect. 6.5 can be further investigated by a closure of calibrated spectra with synthetic solar absorption spectra obtained by radiative transfer model calculations. This analysis enables to detect any large deviations of the real calibration accuracy from the uncertainty estimate given in Sect. 6.5. Note, however, that in addition to the calibration uncertainty further sources of radiance uncertainty contribute in the closure setup, e.g. IWV uncertainty or uncertainties related to the water vapor continuum. Therefore, minor deviations from the 1 to 2 %-uncertainty estimate may remain undetected in the comparison analysis.

In detail, a set of calibrated spectra is compared to synthetic spectra obtained with the LBLRTM radiative transfer model (Clough et al., 2005). The atmospheric state used as an input to the LBLRTM calculations was determined as outlined in Sect. 7.3. In summary,

water vapor column data retrieved from the solar FTIR spectra is used. Water vapor profiles were set according to four times-daily National Center for Environmental Prediction (NCEP) resimulation data, while for temperature profiles a combination of NCEP reanalysis results and a fitted near-surface profile obtained from FIR thermal emission spectra was used. Column values of CO₂, CH₄, and N₂O were measured with the nearby Garmisch solar FTIR. Aerosol optical depth was constrained with sun photometer measurements.

The validation analysis includes spectra measured under clear sky conditions during the December 2013 to February 2014 period during which no realignment or other modifications to the spectrometer were performed. All spectra with an airmass greater than 9.0, i.e. a solar zenith angle greater than $\sim 84^\circ$ were discarded due to increasing inaccuracies in the ray tracing calculation and significant airmass variation during the spectral averaging period at high zenith angles. Additionally, the validation dataset only includes spectra for which the radiance uncertainty due to FOV variations on the tracker mirrors (see Sect. 6.5) is negligible ($< 0.1\%$). These selection thresholds lead to a validation dataset of 52 spectra. For calibration, the 13 December 2013 Langley and 24 February 2014 blackbody results were used.

The corresponding synthetic spectra were then computed for all calibrated spectra in the validation dataset. Figure 10.2b shows the mean measured (black) and synthetic (red) radiance for this set of spectra. The mean spectral residuals, i.e. the difference between synthetic and measured radiance is shown in red in Fig. 10.2c, while the standard deviation of the residuals is shown in grey. Quantitatively accurate closure is only possible outside solar lines due the high ESS uncertainty within the lines. Therefore, these regions are excluded from the comparison based on the selection criterion provided in Sect. 6.2. Within atmospheric lines, the uncertainty of the closure is dominated by atmospheric state and line parameter uncertainties and therefore does not provide substantial insights on the calibration accuracy. We therefore discarded these spectral points by excluding all spectral below 99 % of the upper envelope to the mean radiance in 20 cm⁻¹-wide bins. As outlined in Sect. 6.3, the blackbody measurements demonstrate that the calibration curve varies only slowly with wavenumber and contains no narrow line-like features. Therefore, it is sufficient to validate the calibration results in suitable windows between spectral lines as outlined above. The residuals shown in Fig. 10.2 and their further quantitative analysis given hereafter refer to these suitable validation windows.

The accuracy of the calibration uncertainty provided in Sect. 6.5 can be assessed by comparing the mean spectral residuals to their estimated uncertainty (blue lines in Fig. 10.2c). In addition to the calibration uncertainty according to Sect. 6.5, the residual uncertainty given in Fig. 10.2 contains several further contributions. These contributions describe the atmospheric state uncertainty and further contributions related to the solar FTIR spectral radiance measurements. A detailed assessment of this closure uncertainty budget is given in Sect. 7.5. In addition to the contributions listed there, the uncertainty contribution associated with the water continuum absorption has to be taken into account. Since no uncertainty is provided for the MT_CKD 2.5.2-model (Mlawer et al., 2012) used in the synthetic spectra calculation, the continuum error estimate was set to the difference between the upper and lower end of continuum results provided by recent studies, namely the studies by Ptashnik et al. (2012, 2013) and the MT_CKD 2.5.2-model. A more detailed description of these data sets is given in Sect. 11.2. Note that since for both Langley calibration and model calculations

the same ESS is used, the closure validation does not provide information on the accuracy of the ESS.

As visible in Fig. 10.2c, the mean residuals show very good consistency with the estimated uncertainty. In detail, a fraction of 97.7 % of the residual values lies within the 2σ residual uncertainty estimate. The mean residuals correspond to 1.2 % of the measured radiance at each spectral point on average for the suitable comparison windows. This extensive agreement of the mean residuals with the uncertainty estimate further indicates the validity of the calibration uncertainty budget presented in Sect. 6.5.

Chapter 11

Water Vapor Continuum Results

This section comprises the main findings of this work, namely the quantitative results on the water vapor continuum under atmospheric conditions throughout the infrared spectral range. Results were obtained from thermal emission spectra in the FIR and solar absorption spectra in the NIR using the methods presented in Chapter 8.

The results obtained from the Zugspitze experiment are compared to recent laboratory and atmospheric studies. Throughout most of the NIR range, the results constitute the first measurements of the water vapor continuum under atmospheric conditions, and therefore provide a valuable tool for validation of the MT_CKD continuum model and for resolving the inconsistencies between the findings of recent laboratory studies.

11.1 FIR Continuum

Figure 11.1 shows the mean foreign continuum coefficients determined from the Zugspitze data set in 10 cm^{-1} -wide bins. Table 11.1 contains our results in tabulated form. The results are fully consistent with the MT_CKD 2.5.2 model given the continuum uncertainty estimate according to Sect. 8.1. As visible in Fig. 11.1, our results are also fully consistent with the findings of Liuzzi et al. (2014) that were obtained in a comparable atmospheric closure study carried out in Antarctica.

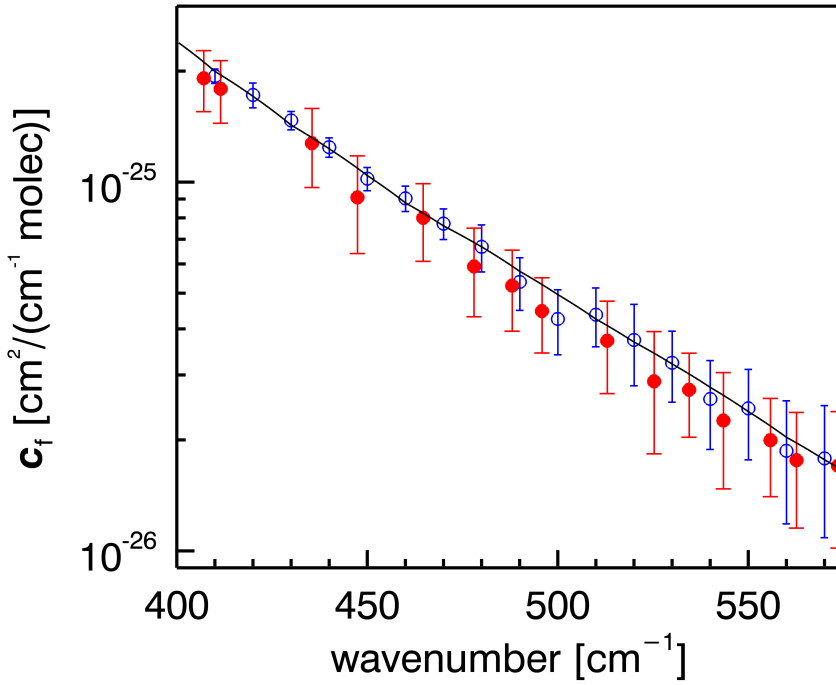


Figure 11.1: Mean foreign continuum coefficients derived from the Zugspitze closure measurements (red) in comparison to the MT_CKD 2.5.2 model (black) and the results of Liuzzi et al. (2014) (blue).

Table 11.1: Mean foreign continuum coefficients derived from the Zugspitze closure measurements and associated (2- σ) uncertainties.

wavenumber [cm ⁻¹]	c_f [cm ² /(cm ⁻¹ molec)]
407.06	$1.91 \cdot 10^{-25} \pm 3.60 \cdot 10^{-26}$
411.49	$1.79 \cdot 10^{-25} \pm 3.46 \cdot 10^{-26}$
435.46	$1.27 \cdot 10^{-25} \pm 3.09 \cdot 10^{-26}$
447.40	$9.09 \cdot 10^{-26} \pm 2.69 \cdot 10^{-26}$
464.67	$8.00 \cdot 10^{-26} \pm 1.90 \cdot 10^{-26}$
478.01	$5.90 \cdot 10^{-26} \pm 1.59 \cdot 10^{-26}$
488.02	$5.24 \cdot 10^{-26} \pm 1.30 \cdot 10^{-26}$
495.83	$4.47 \cdot 10^{-26} \pm 1.03 \cdot 10^{-26}$
512.96	$3.71 \cdot 10^{-26} \pm 1.04 \cdot 10^{-26}$
525.27	$2.88 \cdot 10^{-26} \pm 1.05 \cdot 10^{-26}$
534.45	$2.73 \cdot 10^{-26} \pm 7.02 \cdot 10^{-27}$
543.45	$2.26 \cdot 10^{-26} \pm 7.84 \cdot 10^{-27}$
555.80	$2.00 \cdot 10^{-26} \pm 5.94 \cdot 10^{-27}$
562.63	$1.76 \cdot 10^{-26} \pm 6.10 \cdot 10^{-27}$
573.54	$1.70 \cdot 10^{-26} \pm 6.84 \cdot 10^{-27}$
585.15	$1.10 \cdot 10^{-26} \pm 6.65 \cdot 10^{-27}$

11.2 NIR Continuum

Figure 11.2 shows the mean continuum absorption coefficient \bar{k}_{cont} determined from the Zugspitze dataset in comparison to the MT_CKD 2.5.2 model predictions and several recent laboratory studies. The dry atmospheric conditions at the Zugspitze site (IWV 1.4 to 3.3 mm) enable continuum quantification even within water vapor absorption bands, while only upper limits for continuum absorption can be provided in the centers of window regions. The situation in the window regions is shown in the non-logarithmic plot of Fig. 11.4. The mean atmospheric state of the closure dataset is listed in Table 11.2.

An assignment of the residual OD to water vapor continuum absorption was made based on two arguments: As outlined in Sect. 7.5, great care was taken to construct a comprehensive uncertainty budget including thorough estimates of all relevant error contributions to the closure experiment. Therefore, contributions to the residual OD from other processes than water vapor continuum absorption far beyond the indicated error bars seem unlikely. Furthermore, the IWV dependence of the measured residual OD is consistent with that expected from water vapor continuum absorption. As \bar{k}_{cont} includes contributions due to both foreign- and self continuum, it is expected to scale as the sum of a constant and a linear term with respect to water vapor density and therefore also with respect to IWV. The closure dataset covers an IWV range of $1.4 \text{ mm} < \text{IWV} < 3.3 \text{ mm}$, which enables investigation of the IWV dependence of \bar{k}_{cont} . Due to the narrow range of atmospheric temperatures covered in the data set, temperature dependence of the self continuum can be neglected in this analysis. A fraction of 98.6 % of all measured continuum absorption coefficients in the Zugspitze data set are consistent with a combination of constant and linear scaling with respect to IWV, i.e. with being caused by a combination of foreign- and self water vapor continuum. However, 94.2 % of the data are also consistent with a purely constant scaling, i.e. with being solely due to foreign continuum absorption. This is due to the fact that at the atmospheric conditions covered by the data, in all spectral regions where continuum absorption is detectable beyond the experiment's sensitivity, the foreign continuum constitutes by far the dominant contribution, assuming that the partitioning in self and foreign continuum given by the MT_CKD model is approximately correct.

This analysis shows that the contribution of the self continuum is not unambiguously detectable due to the limited sensitivity of our experiment. Therefore, values of the mean continuum absorption coefficient \bar{k}_{cont} as defined by Eq. 8.4 are provided, including contributions from both self and foreign continuum instead of the more commonly used continuum coefficients c_s and c_f . The prediction of the MT_CKD 2.5.2 model is shown alongside our results for \bar{k}_{cont} in Fig. 11.2. The MT_CKD 2.5.2-values of \bar{k}_{cont} were computed in an analogous way as the values derived from our dataset, i.e. \bar{k}_{cont} was calculated according to Eq. 8.4 for the set of atmospheric states encountered in the data set. The results shown in Fig. 11.2 represent the mean of the MT_CKD predictions for the set of selected measurements. Overall, there is good agreement of our results with the MT_CKD values. Consistency within a 2σ range is observed for 75 % of the spectral range covered by our measurements. The most apparent discrepancy between MT_CKD and our results occurs in the 2800 to 3000 cm^{-1} -range, where our results are about a factor of 5 higher than the MT_CKD predictions. However, care has to be taken in the interpretation of this discrepancy since the 2800 to 3000 cm^{-1} spectral range coincides

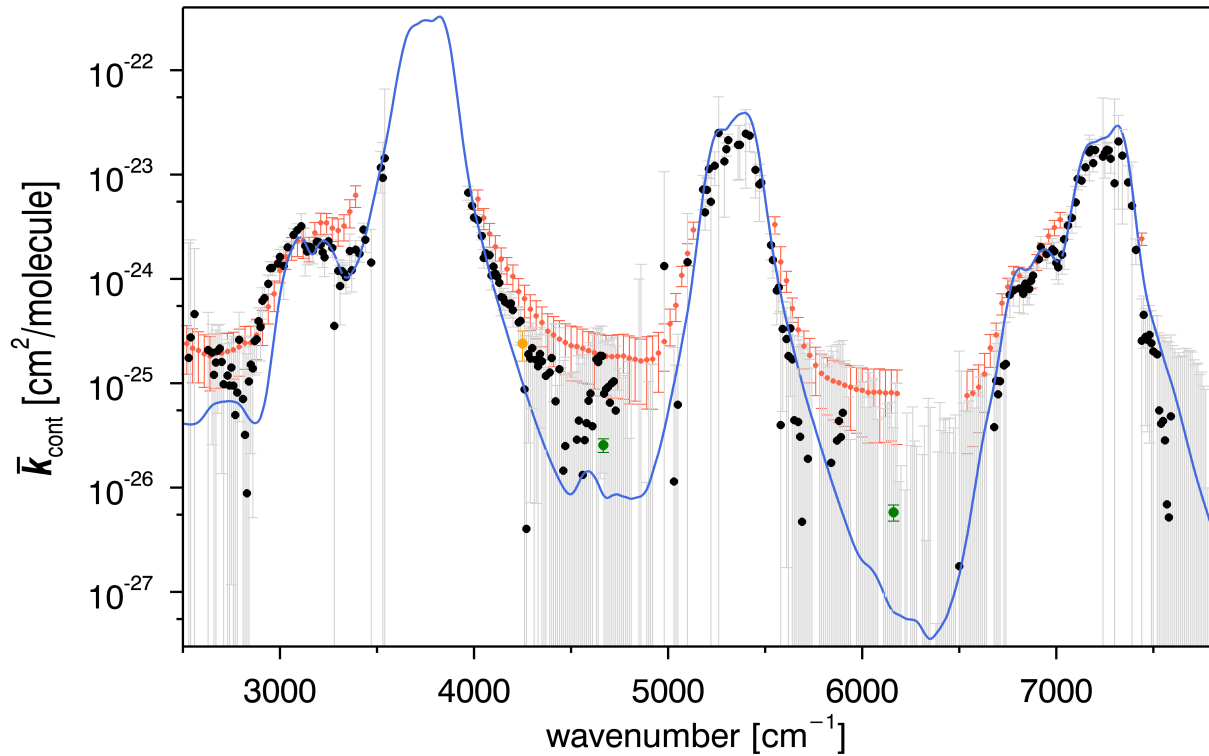


Figure 11.2: Mean continuum absorption coefficient \bar{k}_{cont} determined in the Zugspitze closure experiment and corresponding 2σ uncertainties (black). Results are compared to the MT_CKD 2.5.2 model (blue) and the following laboratory studies: the CRDS measurements of Mondelain et al. (2015) (orange), the calorimetric-interferometric measurements of Bicknell et al. (2006) (green) and the FTIR measurements of Ptashnik et al. (2012, 2013) (red).

Table 11.2: Mean atmospheric state of the closure data set. The data set was selected from Zugspitze solar FTIR spectra measured from December 2013–February 2014 and contains 52 spectra. Spectra selection criteria are listed in Sect. 8.2

altitude [km a.s.l.]	P [mbar]	T [K]	$\rho_{\text{H}_2\text{O}}$ [g m $^{-3}$]	further parameters
2.964	714.074	270.570	1.270	IWV
2.975	713.085	270.522	1.266	XCO ₂
2.987	712.008	270.469	1.263	XCH ₄
3.009	710.036	270.372	1.256	XN ₂ O
3.032	707.982	270.271	1.249	O ₃ column
3.066	704.946	270.121	1.239	
3.099	702.000	269.974	1.229	
3.147	697.763	269.671	1.201	
3.262	687.664	268.899	1.127	
3.497	667.380	267.256	0.966	
3.600	658.649	266.536	0.898	
3.700	650.259	265.838	0.833	
3.800	641.950	265.139	0.769	
3.900	633.727	264.440	0.707	
4.000	625.592	263.741	0.645	
4.100	617.538	263.042	0.585	
4.200	609.570	262.342	0.526	
4.300	601.680	261.644	0.468	
4.400	593.871	260.919	0.446	
4.500	586.147	260.186	0.436	
4.600	578.503	259.455	0.425	
4.700	570.935	258.723	0.415	
4.800	563.441	257.991	0.405	
4.900	556.027	257.260	0.395	
5.000	548.693	256.528	0.385	
5.500	513.149	252.871	0.338	
6.000	479.451	249.366	0.261	
6.500	447.548	245.966	0.169	
7.000	417.379	242.567	0.087	
8.000	361.924	235.748	0.027	
9.000	312.542	228.923	$9.69 \cdot 10^{-3}$	
10.00	268.744	222.463	$2.96 \cdot 10^{-3}$	
15.00	123.703	213.438	$4.17 \cdot 10^{-4}$	
20.00	54.6496	209.890	$2.35 \cdot 10^{-4}$	
30.00	10.775	212.607	$6.27 \cdot 10^{-5}$	
40.00	2.488	248.853	$1.41 \cdot 10^{-5}$	
60.00	0.179	239.829	$9.17 \cdot 10^{-7}$	
100.0	$2.77 \cdot 10^{-4}$	213.601	$1.13 \cdot 10^{-10}$	
120.0	$2.38 \cdot 10^{-5}$	378.719	$8.74 \cdot 10^{-13}$	

with a methane absorption band. Therefore, the accuracy of the continuum result in this range depends on whether the HITRAN error estimate for methane line parameters is correct and whether line coupling effects were treated in sufficiently realistic way in the LBLRTM model. Further significant discrepancies ensue in the 4100 to 4200 cm^{-1} wavenumber region. The higher measurement results from the Zugspitze data indicate that the MT_CKD-model underestimates the continuum absorption in the wings of the 4000 to 5000 cm^{-1} window region. In the centers of water vapor absorption bands (i.e. ~ 5200 – 5400 cm^{-1} and ~ 7100 – 7300 cm^{-1}), our results are significantly lower than the MT_CKD-predictions for a number of spectral points. However, the continuum results in these regions are highly sensitive to accurate input and uncertainty estimates for IWV and water vapor line parameters. Therefore, the slight differences found in the band centers do not provide robust evidence for necessary adjustments of the MT_CKD model.

Figure 11.2 also includes a comparison of our results to several current laboratory studies using different experimental approaches for continuum quantification. For the comparison, \bar{k}_{cont} -values were calculated for the same set of atmospheric states as our results using the continuum coefficients given in the respective studies. For the Mondelain et al. (2015) and Bicknell et al. (2006) results, we used the MT_CKD temperature dependence. For the Ptashnik et al. (2012) and Ptashnik et al. (2013) results, we employ the more sophisticated alternative temperature dependence proposed by Rädel et al. (2015), which was deduced from the measurements of Ptashnik et al. (2011). Note, however, that the importance of the continuum temperature dependence is limited (5 to 20 %, see below) for our dataset. This is due to the fact that no temperature dependence is assumed for the foreign continuum, which is by far dominant for most spectral regions given the dry atmospheric conditions encountered in our data set.

Our results show very good agreement with the CDRS-based measurements of Mondelain et al. (2015). For the spectral range examined by Bicknell et al. (2006) with calorimetric-interferometric measurements, only the upper limit of the continuum absorption is constrained by our data, which is consistent with all laboratory studies cited here. In the window regions, our results show good consistency with the BPS-MT_CKD 2.0-continuum proposed by Paynter and Ramaswamy (2014). The FTIR-based results of Ptashnik et al. (2012) and Ptashnik et al. (2013) in combination with the temperature dependence proposed by Rädel et al. (2015) lead to higher absorption coefficients than our data in several spectral regions. Significant inconsistencies beyond the uncertainty range occur mostly in the wings of water vapor absorption bands, e.g. in the 3200 to 3400 cm^{-1} , and 4000 to 4200 cm^{-1} ranges as visible in Fig. 11.2. In these ranges the absorption coefficients provided by the FTIR laboratory measurements are typically a factor of 2–5 higher compared to our data.

As noted e.g. by Ptashnik et al. (2015), weak lines not included in the line list used for the synthetic spectra calculation may bias the retrieved continuum results. This effect is largely reduced in our analysis due to the spectral selection criteria applied, namely the selection of low-OD windows as outlined in Sect. 8.2, criterion (i). A drawback of this selection scheme is that our analysis is not well suited for the detection of narrow line-like features in the continuum as reported e.g. by Ptashnik et al. (2011).

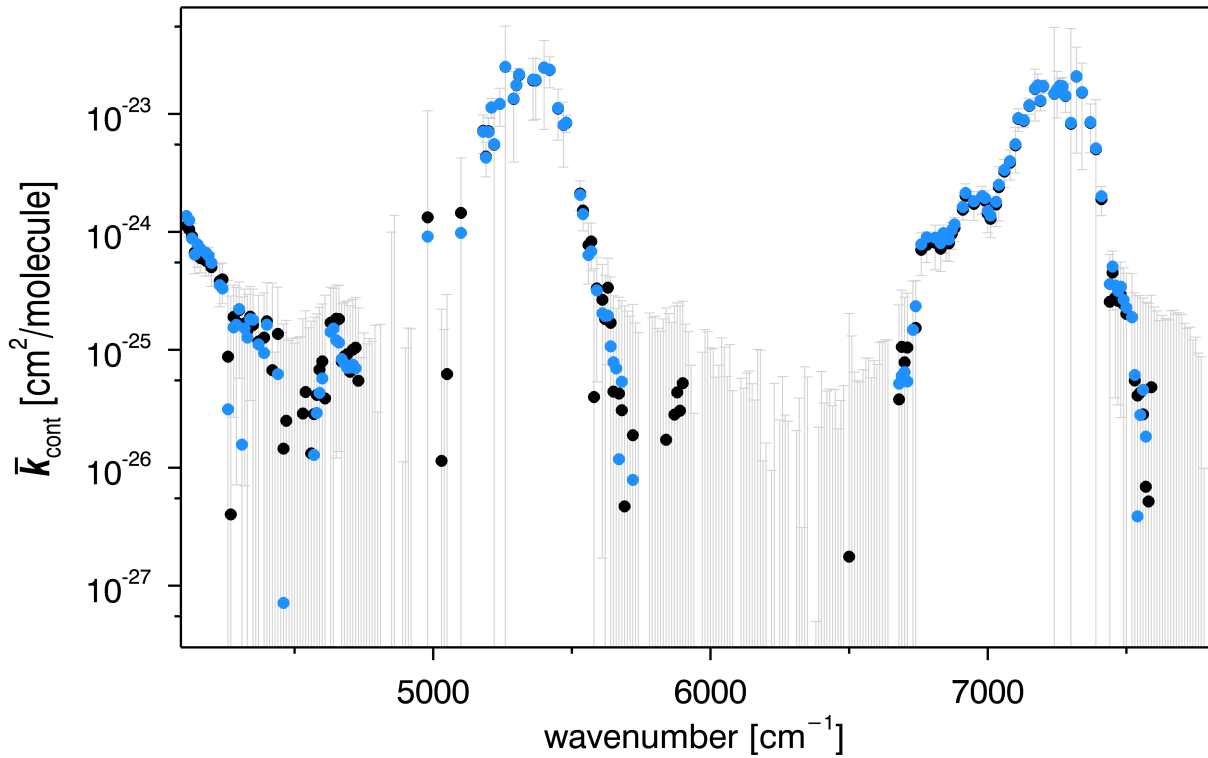


Figure 11.3: Effect of ESS uncertainty on the continuum absorption coefficient \bar{k}_{cont} determined in the Zugspitze closure experiment. \bar{k}_{cont} derived with the ESS of Kurucz (2005) (black data points and grey error bars) in comparison with the results obtained when using the ESS by Menang et al. (2013) (blue data points).

An issue not accounted for in our analysis is the uncertainty of the continuum temperature dependence, since an uncertainty estimate is provided neither for the MT_CKD nor the Rädel et al. (2015) relations. However, under the atmospheric conditions covered by our data set and assuming the MT_CKD self-to-foreign ratio, the self continuum contributes only 10 to 30 % to the total continuum absorption at the spectral points for which significant continuum was detected. While no temperature dependence is assumed for the dominant foreign contribution, the temperature dependence of the self continuum changes the mean continuum absorption coefficient by 5 to 20 % within the spectral range considered here and assuming the Rädel et al. (2015) relation. Therefore, it seems unlikely that the differences between the results of Ptashnik et al. (2012) and Ptashnik et al. (2013) and our data are solely due to inaccuracies in the continuum temperature dependence.

As pointed out in Chapter 6, the design of the combined calibration method leads to much lower influence of ESS inaccuracies on the determined continuum compared to e.g. a pure blackbody calibration. To investigate this influence, the continuum retrieval was repeated using the ESS determined by Menang et al. (2013) instead of the ESS by Kurucz (2005) that was used to generate the results presented in Fig. 11.2. Note that the Menang et al. (2013) ESS only covers the spectral region $\nu > 4000 \text{ cm}^{-1}$. The comparison is therefore restricted to $4233.52 \text{ cm}^{-1} < \nu < 7800 \text{ cm}^{-1}$, which corresponds to the first Langley point covered by

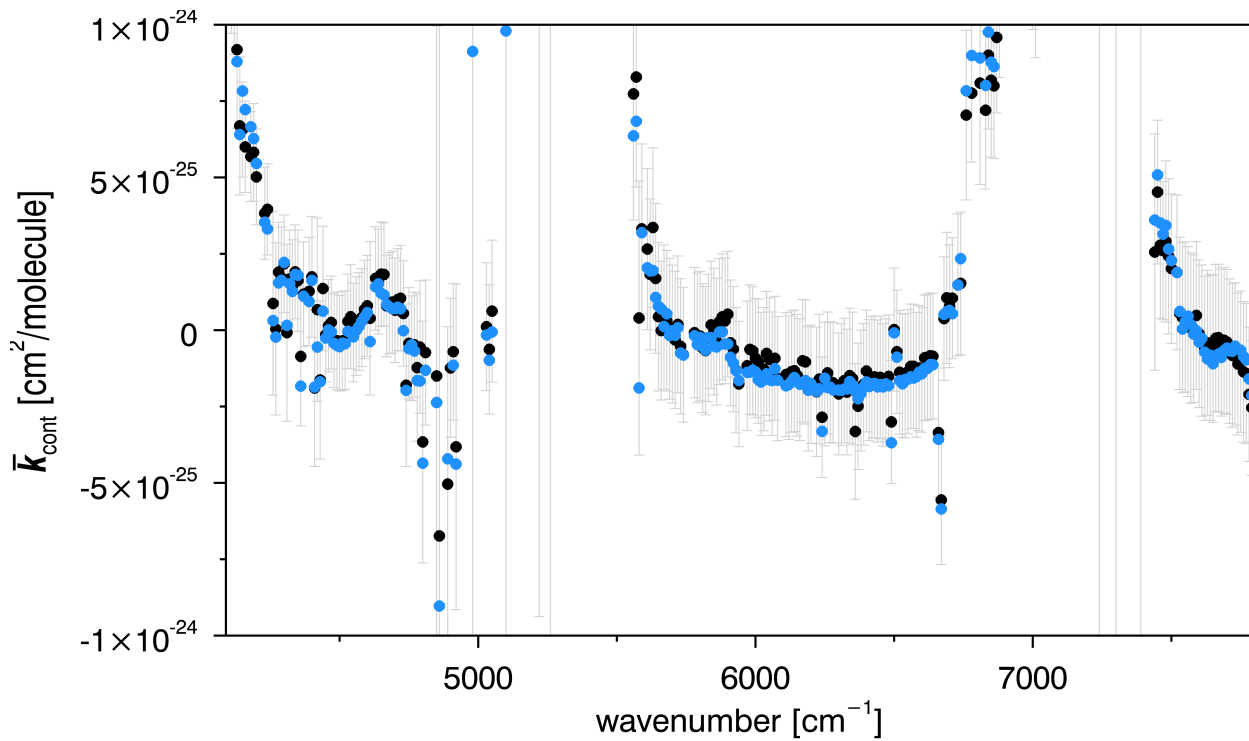


Figure 11.4: Non-logarithmic plot showing the effect of ESS uncertainty on the continuum absorption coefficient \bar{k}_{cont} determined in the Zugspitze closure experiment in the window regions. \bar{k}_{cont} derived with the ESS of Kurucz (2005) (black data points and grey error bars) in comparison with the results obtained when using the ESS by Menang et al. (2013) (blue data points).

the Menang et al. (2013) ESS and the maximum wavenumber value covered by our analysis, respectively.

For this region, the median of the absolute value of the difference between the Menang et al. (2013) and Kurucz (2005) continuum results corresponds to 11 % of the continuum uncertainty estimate. Therefore, ESS uncertainty does not constitute a major accuracy limitation of our analysis. The ESS-related continuum uncertainty was estimated from the difference of the Menang et al. (2013) and Kurucz (2005) results and included in the uncertainty budget as described in Sect. 7.5. In detail, the ESS contribution increases the total uncertainty by 0.6 % on average when added in quadrature to the remaining uncertainty budget.

Part V

Summary and Outlook

Summary

The aim of this work was to improve the quantitative knowledge of the water vapor continuum throughout the infrared spectral range via a radiative closure experiment at the Zugspitze high-altitude observatory (47.42° N, 10.98° E, 2964 m a.s.l.). Water vapor is the most important contributor to the interaction between infrared radiation and trace gases in the atmosphere. Therefore, an accurate quantitative understanding of these interaction processes is a prerequisite for realistic atmospheric radiative transfer calculations, which are applied e.g. in climate models or remote sensing techniques. An important unresolved issue in this field is the lack of precise quantitative knowledge of the water vapor continuum. Numerous laboratory and field studies have addressed this issue in the recent past. However, due to a number of limitations to the experimental techniques, several key open questions concerning the water vapor continuum remain. This thesis therefore addressed the following main research questions:

- What is the magnitude of the water vapor continuum in the NIR spectral range under atmospheric conditions?
- How reliable are current continuum models and the results of atmospheric continuum measurements in FIR?

The experimental setup established for this study furthermore lays the foundation to investigate additional key issues:

- What is the correct temperature dependence of the water vapor continuum?
- What is the ratio between the two contributions to the continuum, i.e. self and foreign continuum?

Several new experimental methods that enable to address these research questions have been presented in this work. The main findings considering these methods and the water vapor continuum results will be summarized in the following.

The method of radiative closure that was employed for continuum quantification consists in a quantitative comparison of spectral radiance measurements to radiative transfer calculations. The spectral residuals, i.e. the differences between measured and synthetic spectra are used to validate and, if necessary, adjust the strength of the water vapor continuum assumed in the model calculations. To this aim, spectral radiance measurements covering the terrestrial and solar infrared between 400 and 7800 cm^{-1} ($1.3\text{--}25.0\text{ }\mu\text{m}$) were implemented at the Zugspitze site. As a benefit for such experiments, atmospheric states with very low IWV and very low AOD are frequently encountered at the Zugspitze mountain site. In addition, the study benefits from the extensive permanent instrumentation available for both spectral radiance and atmospheric

state measurements, which were complemented and further developed for the purpose of this work.

A comprehensive uncertainty budget of the experiment was constructed in order to assess the uncertainty of the continuum results. The dominant contribution to this uncertainty budget in the FIR is from water vapor line parameters, while temperature profile uncertainties dominate in the MIR. Uncertainty in the NIR is dominated by varying contributions, namely water vapor line parameter uncertainties in the vicinity of water vapor bands and solar FTIR calibration uncertainty in combination with AOD uncertainties in the window regions.

A strategy to determine pointing errors in solar absorption spectrometry was introduced in this thesis. Knowledge of the mispointing, i.e. the deviation of the instrument's line of sight from the center of the solar disc, allows for subsequent correction of errors in the radiometric calibration of NIR solar absorption spectra and of trace gas total column or vertical profile retrievals. The presented approach relies on repeated determination of the Doppler shift of solar spectral lines from spectra measured at different orientations of the solar rotation axis relative to the zenith direction. Using this technique, notable mispointing was detected for a short period in the Zugspitze solar FTIR measurement time series (i.e. September 2012–September 2014), which can be attributed to a non-optimum optical configuration. The mispointing was found to cause significant bias in XCH_4 measurements. However, applying the mispointing correction scheme restored consistency in the trend and bias between the Zugspitze results and the measurements made at the nearby Garmisch site (47.48° N , 11.06° E , 743 m a.s.l.). In conclusion, the mispointing correction significantly improved the sensitivity of the closure experiment via more accurate trace gas column measurements and improved radiometric calibration accuracy. Beyond the scope of the closure study, the mispointing correction presented in this work is of particular benefit for refining existing records of trace gas column and profile measurements for all kind of solar absorption spectrometric measurements, i.e. soundings in the MIR and NIR.

Solar FTIR spectral radiance measurements have to be radiometrically calibrated to be used for continuum quantification in the closure experiment. However, no standard calibration method with sufficient accuracy was available previously in the NIR. Therefore, this work described a novel radiometric calibration strategy for solar FTIR spectral radiance measurements in the NIR and MIR which relies on a combination of the Langley method with radiance measurements of a high-temperature blackbody source. While the Langley method yields highly accurate calibration results in narrow spectral windows with little molecular absorption, the blackbody measurements constrain the shape of the calibration curve in between these points. This combined calibration scheme provides a calibration uncertainty of about 1–2%. The calibration results were validated by investigating the consistency of different calibration measurements and by comparison of the calibrated spectra to model calculations. Both validation efforts substantiate the uncertainty estimate. The presented calibration scheme therefore fulfills its main goal, i.e. to provide sufficiently accurate radiometric calibration of solar FTIR spectra for the use in radiative closure experiments.

In the FIR spectral region, the quantification of the water vapor continuum relied on measurements of downwelling atmospheric thermal emission. The continuum results determined

from the Zugspitze data set are consistent with the semi-empirical MT_CKD 2.5.2 continuum model (Mlawer et al., 2012), which is widely used in atmospheric radiative transfer calculations. Furthermore, the FIR results are consistent with other recent atmospheric closure studies. In conclusion, the findings of this work indicate that the magnitude of the FIR water vapor continuum assumed in current climate models and remote sensing techniques is reasonably accurate.

The results of this work constitute the first quantification of the water vapor continuum under atmospheric conditions for most of the spectral range covered by the NIR closure experiment (2500 to 7800 cm^{-1}). Therefore, the measurements constitute a valuable tool for the validation of the MT_CKD continuum model and furthermore allow to resolve the inconsistencies between the results of different recent laboratory studies in this spectral range. Constraints on the continuum absorption were presented in the wings and some spectral windows in the centers of water vapor absorption bands. Due to the low IWV encountered throughout our measurement period, only the upper boundary of the continuum could be constrained in the centers of atmospheric windows. The results are consistent with the MT_CKD 2.5.2 model throughout most of the experiment's spectral range, although they indicate a need for increasing the absorption strength compared to the model in some spectral regions such as the wings of water vapor absorption bands. Compared to recent FTIR laboratory studies (Ptashnik et al., 2012, 2013), our measurements indicate significantly weaker continuum absorption under atmospheric conditions in the wings of water vapor absorption bands. Further experimental techniques used for continuum quantification in laboratory experiments include cavity ring-down spectroscopy (CRDS) and calorimetric-interferometric measurements. The results of the Zugspitze experiment show very good agreement to the findings of studies relying on these alternative methods (Mondelain et al., 2015; Bicknell et al., 2006), which, however, cover only a small fraction of the spectral range investigated by the closure study. In summary, the results provide a valuable foundation for an improved quantification of the NIR water vapor continuum under atmospheric conditions. The findings imply that the MT_CKD continuum model significantly underestimates the continuum absorption in the wings of absorption bands and likely also in window regions. However, according to the atmospheric measurements, this underestimation is less pronounced than indicated by recent FTIR laboratory studies. The detected deviations from the MT_CKD model have an important impact since they lead to inaccuracies in radiative transfer calculations employed e.g. in climate models and numerous remote sensing techniques.

Outlook

Throughout this work, important advances in the quantification of the infrared water vapor continuum under atmospheric conditions have been presented. This leads to the question whether the changes in the magnitude of the NIR continuum suggested by this work have a significant influence e.g. in climate models. Therefore, a follow-up analysis including the implementation of the results in the ECHAM climate model is planned in collaboration with the model developers at Max Planck Institute for Meteorology, Hamburg, Germany.

An estimate of the possible climate effects caused by the adjustments to the water vapor continuum that were presented in this work can be gained from the recent studies by Paynter and Ramaswamy (2014) and Rädel et al. (2015). These publications investigate the climate relevance of modifications to the continuum which are in fair agreement to the findings of this work, most notably of an increased NIR continuum absorption in window regions compared to the widely used MT_CKD 2.5.2.-model. Therefore, when investigating the impact of the Zugspitze results, one may expect similar influence in climate models. Namely, the main effects comprise an increase in clear-sky global dimming, which leads to an adjustment of the surface energy budget through a decrease in both surface latent and sensible heat. Further implications of these adjustments are e.g. a decrease in tropical convection and rainfall.

Despite the advances presented in this work, a number of open questions concerning the water vapor continuum remain unsolved. The open questions in the field of continuum measurements comprise the separation of the measured total continuum in self and foreign continuum contributions and improved constraints on the temperature dependence of the continuum. Due to the limited amount of measurement data included in this work, these parameters could not be securely constrained from the available data. However, the experimental setup implemented at the Zugspitze observatory is designed as a long-term experiment and may contribute to the solution of these key questions in the future. Data acquisition at the Zugspitze site is ongoing, which means that a future study based on a more extensive data set, covering a broader range of I WV and atmospheric temperature, may enable to resolve these open questions.

Obviously, the final objective in the field of the water vapor continuum is to establish a physical explanation of the causative processes of the continuum in addition to an accurate quantification by measurements. Previous theoretical advances have shown that attaining this objective requires a combination of significant progress in all three aspects that contributed to improving our understanding of the water vapor continuum: the theoretical quantum mechanical framework, laboratory studies, and field experiments as described in this work.

Bibliography

Ackerman, T. P. and Stokes, G. M.: The Atmospheric Radiation Measurement Program, *Phys. Today*, 56, 38–44, doi:10.1063/1.1554135, 2003.

Adrian, G. P., Baumann, M., Blumenstock, T., Fischer, H., Friedle, A., Gerhardt, L., Maucher, G., Oelhaf, H., Scheuerpflug, W., Thomas, P., Trieschmann, O., and Wegner, A.: First results of ground-based FTIR measurements of atmospheric trace gases in north Sweden and Greenland during EASOE, *Geophys. Res. Lett.*, 21, 1343–1346, doi:10.1029/93GL01304, 1994.

Anderson, G. P., Clough, S. A., Kneizys, F. X., Chetwynd, J. H., and Shettle, E. P.: AFGL atmospheric constituent profiles (0–120km), AFGL-TR-86-0110, Air Force Geophys. Laboratory, Hanscom AFB, MA, USA, 1986.

Antonelli, P., Revercomb, H. E., Sromovsky, L. A., Smith, W. L., Knuteson, R. O., Tobin, D. C., Garcia, R. K., Howell, H. B., Huang, H.-L., and Best, F. A.: A principal component noise filter for high spectral resolution infrared measurements, *J. Geophys. Res.*, 109, D23 102, doi:10.1029/2004JD004862, 2004.

Arrhenius, S.: On the influence of carbonic acid in the air upon the temperature of the ground, *Philos. Mag.*, 41, 237–275, doi:10.1086/121158, 1896.

Baranov, Y. I. and Lafferty, W. J.: The water-vapor continuum and selective absorption in the 3–5 μm spectral region at temperatures from 311 to 363 K, *J. Quant. Spectrosc. Radiat. Transfer*, 112, 1304–1313, doi:10.1016/j.jqsrt.2011.01.024, 2011.

Baranov, Y. I. and Lafferty, W. J.: The water vapour self- and water–nitrogen continuum absorption in the 1000 and 2500 cm^{-1} atmospheric windows, *Philos. T. Roy. Soc. A.*, 370, 2578–2589, doi:10.1098/rsta.2011.0234, 2012.

Baranov, Y. I., Lafferty, W. J., Ma, Q., and Tipping, R. H.: Water-vapor continuum absorption in the 800–1250 cm^{-1} spectral region at temperatures from 311 to 363 K, *J. Quant. Spectrosc. Radiat. Transfer*, 109, 2291–2302, doi:10.1016/j.jqsrt.2008.03.004, 2008.

Bhawar, R., Bianchini, G., Bozzo, A., Cacciani, M., Calvello, M. R., Carlotti, M., Castagnoli, F., Cuomo, V., Di Girolamo, P., Di Iorio, T., Di Liberto, L., di Sarra, A., Esposito, F., Fiocco, G., Fu, D., Grieco, G., Maestri, T., Masiello, G., Muscari, G., Palchetti, L., Papandrea, E., Pavese, G., Restieri, R., Rizzi, R., Romano, F., Serio, C., Summa, D., Todini, G., and Tosi,

- E.: Spectrally resolved observations of atmospheric emitted radiance in the H₂O rotation band, *Geophys. Res. Lett.*, 35, L04812, doi:10.1029/2007GL032207, 2008.
- Bianchini, G., Palchetti, L., Muscari, G., Fiorucci, I., Di Girolamo, P., and Di Iorio, T.: Water vapor sounding with the far infrared REFIR-PAD spectroradiometer from a high-altitude ground-based station during the ECOWAR campaign, *J. Geophys. Res.*, 116, D02310, doi:10.1029/2010JD014530, 2011.
- Bicknell, W., Cecca, S., Griffin, M., Swartz, S., and Flusberg, A.: Search for low absorption regions in the 1.6 and 2.1 μ m atmospheric windows, *J. Dir. Energy*, 2, 151–161, 2006.
- Bodhaine, B. A., Wood, N. B., Dutton, E. G., and Slusser, J. R.: On Rayleigh Optical Depth Calculations, *J. Atmos. Ocean. Tech.*, 16, 1854–1861, doi:10.1175/1520-0426(1999)016<1854:ORODC>2.0.CO;2, 1999.
- Borsdorff, T. and Sussmann, R.: On seasonality of stratospheric CO above midlatitudes: New insight from solar FTIR spectrometry at Zugspitze and Garmisch, *Geophys. Res. Lett.*, 36, L21804, doi:10.1029/2009GL040056, 2009.
- Brunt, D.: Notes on radiation in the atmosphere, *Q. J. Roy. Meteor. Soc.*, 58, 389–420, doi:10.1002/qj.49705824704, 1932.
- Burch, D. E.: Continuum absorption by H₂O, Report AFGL-TR-81-0300, Air Force Geophys. Laboratory, Hanscom AFB, MA, USA, 1982.
- Burch, D. E.: Absorption by H₂O in narrow windows between 3000 and 4200 cm^{-1} , Report AFGL-TR-85-0036, Air Force Geophys. Laboratory, Hanscom AFB, MA, USA, 1985.
- Burch, D. E. and Alt, R. L.: Continuum absorption by H₂O in the 700–1200 cm^{-1} and 2400–2800 cm^{-1} windows, Report AFGL-TR-84-0128, Air Force Geophys. Laboratory, Hanscom AFB, MA, USA, 1984.
- Chandrasekhar, S.: Radiative Transfer, The International Series of Monographs on Physics, Fowler, R. H., Kapitza, P., Mott, N. F., and Bullard, E. C. (eds.), Clarendon Press, Oxford, UK, 1950.
- Clough, S. A., Kneizys, F. X., and Davies, R. W.: Line Shape and the Water Vapor Continuum, *Atmos. Res.*, 23, 229–241, doi:10.1016/0169-8095(89)90020-3, 1989.
- Clough, S. A., Shephard, M. W., Mlawer, E. J., Delamere, J. S., Iacono, M. J., Cady-Pereira, K., Boukabara, S., and Brown, P. D.: Atmospheric radiative transfer modeling: a summary of the AER codes, *J. Quant. Spectrosc. Radiat. Transfer*, 91, 233–244, doi:10.1016/j.jqsrt.2004.05.058, 2005.
- Cormier, J. G., Ciurylo, R., and Drummond, J. R.: Cavity ringdown spectroscopy measurements of the infrared water vapor continuum, *J. Chem. Phys.*, 116, 1030, doi:10.1063/1.1425825, 2002.

- Cormier, J. G., Hodges, J. T., and Drummond, J. R.: Infrared water vapor continuum absorption at atmospheric temperatures, *J. Chem. Phys.*, 122, 114309, doi:10.1063/1.1862623, 2005.
- Delamere, J. S., Clough, S. A., Payne, V. H., Mlawer, E. J., Turner, D. D., and Gamache, R. R.: A far-infrared radiative closure study in the Arctic: Application to water vapor, *J. Geophys. Res.*, 115, D17106, doi:10.1029/2009JD012968, 2010.
- Elsasser, W. M.: Far infrared absorption of atmospheric water vapor, *Astrophys. J.*, 87, 497–507, doi:10.1086/143940, 1938.
- Esposito, F., Grieco, G., Masiello, G., Pavese, G., Restieri, R., Serio, C., and Cuomo, V.: Inter-comparison of line-parameter spectroscopic databases using downwelling spectral radiance, *Q. J. Roy. Meteor. Soc.*, 133, 191–202, doi:10.1002/qj.131, 2007.
- Fourier, J.: Remarques Générales Sur Les Températures Du Globe Terrestre Et Des Espaces Planétaires, *Annales de Chimie et du Physique*, 27, 136–167, 1824.
- Fulghum, S. F. and Tilleman, M. M.: Interferometric calorimeter for the measurement of water-vapor absorption, *J. Opt. Soc. Am. B.*, 8, 2401–2413, doi:10.1364/JOSAB.8.002401, 1991.
- Gardiner, T. D., Forbes, A., de Mazière, M., Vigouroux, C., Mahieu, E., Demoulin, P., Velasco, V., Notholt, J., Blumenstock, T., Hase, F., Kramer, I., Sussmann, R., Stremme, W., Mellqvist, J., Strandberg, A., Ellingsen, K., and Gauss, M.: Trend analysis of greenhouse gases over Europe measured by a network of ground-based remote FTIR instruments, *Atmos. Chem. Phys.*, 8, 6719–6727, doi:10.5194/acp-8-6719-2008, 2008.
- Gardiner, T. D., Coleman, M., Browning, H., Tallis, L., Ptashnik, I. V., and Shine, K. P.: Absolute high spectral resolution measurements of surface solar radiation for detection of water vapour continuum absorption, *Philos. T. Roy. Soc. A.*, 370, 2590–2610, doi:10.1098/rsta.2011.0221, 2012.
- Giles, P. M.: Time-Distance Measurements of Large-Scale Flows in the Solar Convection Zone, PhD thesis, Stanford University, CA, USA, 2000.
- Gisi, M., Hase, F., Dohe, S., and Blumenstock, T.: Camtracker: a new camera controlled high precision solar tracker system for FTIR-spectrometers, *Atmos. Meas. Tech.*, 4, 47–54, doi:10.5194/amt-4-47-2011, 2011.
- Griffiths, P. and De Haseth, J.: Fourier Transform Infrared Spectrometry, 2nd Edition, John Wiley & Sons, Inc., Hoboken, NJ, USA, doi:10.1002/047010631X, 2007.
- Guyemard, C.: SMARTS2, Simple Model of the Atmospheric Radiative Transfer of Sunshine: Algorithms and Performance Assessment, Report FSEC-PF-270-95, Florida Solar Energy Center, Cocoa, FL, USA, 1995.

Harries, J., Carli, B., Rizzi, R., Serio, C., Mlynczak, M., Palchetti, L., Maestri, T., Brindley, H., and Masiello, G.: The Far-infrared Earth, *Rev. Geophys.*, 46, RG4004, doi:10.1029/2007RG000233, 2008.

Hase, F.: Inversion von Spurengasprofilen aus hochaufgelösten bodengebundenen FTIR-Messungen in Absorption, PhD thesis, Karlsruhe Institute of Technology, Karlsruhe, Germany, 2000.

Hase, F., Hannigan, J. W., Coffey, M. T., Goldman, A., Hopfner, M., Jones, N. B., Rinsland, C. P., and Wood, S. W.: Intercomparison of retrieval codes used for the analysis of high-resolution, ground-based FTIR measurements, *J. Quant. Spectrosc. Radiat. Transfer*, 87, 25–52, doi:10.1016/j.jqsrt.2003.12.008, 2004.

Hausmann, P., Sussmann, R., and Smale, D.: Contribution of oil and natural gas production to renewed increase in atmospheric methane (2007–2014): topdown estimate from ethane and methane column observations, *Atmos. Chem. Phys.*, 16, 3227–3244, doi:10.5194/acp-16-3227-2016, 2016.

Held, I. M. and Soden, B. J.: Water Vapor Feedback and Global Warming, *Annu. Rev. Energ. Env.*, 25, 441–475, doi:10.1146/annurev.energy.25.1.441, 2000.

Hestroffer, D. and Magnan, C.: Wavelength dependency of the Solar limb darkening, *Astron. Astrophys.*, 333, 338–342, 1998.

IPCC: Historical Overview of Climate Change, in: Climate Change 2007: The Physical Science Basis. Contribution of Working Group I to the Fourth Assessment Report of the Intergovernmental Panel on Climate Change, Solomon, S., Qin, D., Manning, M., Chen, Z., Marquis, M., Averyt, K. B., Tignor, M., and Miller, H. L. (eds.), Cambridge University Press, Cambridge, UK and New York, NY, USA, 93–127, 2007.

IPCC: Climate Change 2013: The Physical Science Basis. Contribution of Working Group I to the Fifth Assessment Report of the Intergovernmental Panel on Climate Change, Stocker, T. F., Qin, D., Plattner, G.-K., Tignor, M., Allen, S.K., Boschung, J., Nauels, A., Xia, Y., Bex, V., and Midgley, P. M. (eds.), Cambridge University Press, Cambridge, UK and New York, NY, USA, doi:10.1017/CBO9781107415324, 2013.

Kämpfer, N., ed.: Monitoring Atmospheric Water Vapour: Ground-Based Remote Sensing and In-situ Methods, ISSI Scientific Report Series, Vol. 10, Springer, Berlin, Germany, doi:10.1007/978-1-4614-3909-7, 2013.

Kasten, F. and Young, A. T.: Revised optical air mass tables and approximation formula, *Appl. Opt.*, 28, 4735–4738, doi:10.1364/AO.28.004735, 1989.

Kiehl, J. T. and Trenberth, K. E.: Earth's Annual Global Mean Energy Budget., *B. Am. Meteorol. Soc.*, 78, 197–197, doi:10.1175/1520-0477(1997)078<0197:EAGMEB>2.0.CO;2, 1997.

- Knuteson, R. O., Revercomb, H. E., Best, F. A., Ciganovich, N. C., Dedecker, R. G., Dirkx, T. P., Ellington, S. C., Feltz, W. F., Garcia, R. K., Howell, H. B., Smith, W. L., Short, J. F., and Tobin, D. C.: Atmospheric Emitted Radiance Interferometer. Part I: Instrument Design, *J. Atmos. Ocean. Tech.*, 21, 1763, doi:10.1175/JTECH-1662.1, 2004a.
- Knuteson, R. O., Revercomb, H. E., Best, F. A., Ciganovich, N. C., Dedecker, R. G., Dirkx, T. P., Ellington, S. C., Feltz, W. F., Garcia, R. K., Howell, H. B., Smith, W. L., Short, J. F., and Tobin, D. C.: Atmospheric Emitted Radiance Interferometer. Part II: Instrument Performance, *J. Atmos. Ocean. Tech.*, 21, 1777, doi:10.1175/JTECH-1663.1, 2004b.
- Köhler, U.: Homogenization and Re-evaluation of the Long-Term Ozone Series at the Met. Obs. Hohenpeissenberg, Final Report of the DWD-Project K/U 31, DWD, Meterologisches Observatorium Hohenpeissenberg, Germany, 1995.
- Kurucz, R. L.: The Solar Irradiance by Computation, <http://kurucz.harvard.edu/sun.html>, 2005.
- Kurylo, M. J.: Network for the detection of stratospheric change, *Proc. SPIE 1491, Remote Sensing of Atmospheric Chemistry*, Orlando, FL, USA, 1 September 1991, 168, 1991.
- Liou, K. N.: An introduction to atmospheric radiation, 2nd Edition, International Geophysics, Vol. 84, Dmowska, R., Holton, J. R., Rossby, H. T. (eds.), Academic Press, Cambridge, MA, USA, doi:10.1256/003590003102695746, 2002.
- Liuzzi, G., Masiello, G., Serio, C., Palchetti, L., and Bianchini, G.: Validation of H_2O continuum absorption models in the wave number range 180-600 cm^{-1} with atmospheric emitted spectral radiance measured at the Antarctica Dome-C site, *Opt. Express*, 22, 16 784–16 801, doi:10.1364/OE.22.016784, 2014.
- Mariani, Z., Strong, K., Wolff, M., Rowe, P., Walden, V., Fogal, P. F., Duck, T., Lesins, G., Turner, D. S., Cox, C., Eloranta, E., Drummond, J. R., Roy, C., Turner, D. D., Hudak, D., and Lindenmaier, I. A.: Infrared measurements in the Arctic using two Atmospheric Emitted Radiance Interferometers, *Atmos. Meas. Tech.*, 5, 329–344, doi:10.5194/amt-5-329-2012, 2012.
- Masiello, G., Serio, C., Esposito, F., and Palchetti, L.: Validation of line and continuum spectroscopic parameters with measurements of atmospheric emitted spectral radiance from far to mid infrared wave number range, *J. Quant. Spectrosc. Radiat. Transfer*, 113, 1286 – 1299, doi:10.1016/j.jqsrt.2012.01.019, 2012.
- Mayer, B.: Radiative transfer in the cloudy atmosphere, *Eur. Phys. J. Conferences* 1, ERCA 2008 - From the Human Dimensions of Global Environmental Change to the Observation of the Earth from Space, Grenoble, France, January 7–February 1, 2008, 75-99, 2009.
- Menang, K. P., Coleman, M. D., Gardiner, T. D., Ptashnik, I. V., and Shine, K. P.: A high-resolution near-infrared extraterrestrial solar spectrum derived from ground-based Fourier transform spectrometer measurements, *J. Geophys. Res.*, 118, 5319–5331, doi:10.1002/jgrd.50425, 2013.

- Mlawer, E. J., Taubman, S. J., Brown, P. D., Iacono, M. J., and Clough, S. A.: Radiative transfer for inhomogeneous atmospheres: RRTM, a validated correlated-k model for the longwave, *J. Geophys. Res.*, 102, 16 663–16 682, doi:10.1029/97JD00237, 1997.
- Mlawer, E. J., Payne, V. H., Moncet, J.-L., Delamere, J. S., Alvarado, M. J., and Tobin, D. C.: Development and recent evaluation of the MT_CKD model of continuum absorption, *Philos. T. Roy. Soc. A.*, 370, 2520–2556, doi:10.1098/rsta.2011.0295, 2012.
- Molineaux, B., Ineichen, P., and O'Neill, N.: Equivalence of Pyrheliometric and Monochromatic Aerosol Optical Depths at a Single Key Wavelength, *Appl. Opt.*, 37, 7008–7018, doi:10.1364/AO.37.007008, 1998.
- Mondelain, D., Aradj, A., Kassi, S., and Campargue, A.: The water vapour self-continuum by CRDS at room temperature in the 1.6 μm transparency window, *J. Quant. Spectrosc. Radiat. Transfer*, 130, 381–391, doi:10.1016/j.jqsrt.2013.07.006, 2013.
- Mondelain, D., Manigand, S., Kassi, S., and Campargue, A.: Temperature dependence of the water vapor self-continuum by cavity ring-down spectroscopy in the 1.6 μm transparency window, *J. Geophys. Res.*, 119, 5625–5639, doi:10.1002/2013JD021319, 2014.
- Mondelain, D., Vasilchenko, S., Cermak, P., Kassi, S., and Campargue, A.: The self- and foreign-absorption continua of water vapor by cavity ring-down spectroscopy near 2.35 μm , *Phys. Chem. Chem. Phys.*, 17, 17 762–17 770, doi:10.1039/C5CP01238D, 2015.
- Newman, S. M., Green, P. D., Ptashnik, I. V., Gardiner, T. D., Coleman, M. D., McPheat, R. A., and Smith, K. M.: Airborne and satellite remote sensing of the mid-infrared water vapour continuum, *Philos. T. Roy. Soc. A.*, 370, 2611–2636, doi:10.1098/rsta.2011.0223, 2012.
- Notholt, J., Beninga, I., and Schrems, O.: Shipborne FT-IR measurements of atmospheric trace gases on a south (33° S) to north (53° N) Atlantic traverse, *Appl. Spectrosc.*, 49, 1525–1527, doi:10.1366/0003702953965498, 1995.
- Paynter, D. and Ramaswamy, V.: Variations in water vapor continuum radiative transfer with atmospheric conditions, *J. Geophys. Res.*, 117, D16 310, doi:10.1029/2012JD017504, 2012.
- Paynter, D. and Ramaswamy, V.: Investigating the impact of the shortwave water vapor continuum upon climate simulations using GFDL global models, *J. Geophys. Res.*, 119, 10 720–10 737, doi:10.1002/2014JD021881, 2014.
- Paynter, D. J. and Ramaswamy, V.: An assessment of recent water vapor continuum measurements upon longwave and shortwave radiative transfer, *J. Geophys. Res.*, 116, D20 302, doi:10.1029/2010JD015505, 2011.
- Paynter, D. J., Ptashnik, I. V., Shine, K. P., and Smith, K. M.: Pure water vapor continuum measurements between 3100 and 4400 cm^{-1} : Evidence for water dimer absorption in near atmospheric conditions, *J. Geophys. Res.*, 34, L12808, doi:10.1029/2007GL029259, 2007.

- Paynter, D. J., Ptashnik, I. V., Shine, K. P., Smith, K. M., McPheat, R., and Williams, R. G.: Laboratory measurements of the water vapor continuum in the 1200-8000 cm^{-1} region between 293 K and 351 K, *J. Geophys. Res.*, 114, D21301, doi:10.1029/2008JD011355, 2009.
- Pfeilsticker, K., Lotter, A., Peters, C., and Bösch, H.: Atmospheric Detection of Water Dimers via Near-Infrared Absorption, *Science*, 300, 2078–2081, doi:10.1126/science.1082282, 2003.
- Planck, M.: Über das Gesetz der Energieverteilung im Normalspektrum., *Ann. Phys.*, 309, 553–563, 1901.
- Ptashnik, I. V.: Evidence for the contribution of water dimers to the near-IR water vapour self-continuum, *J. Quant. Spectrosc. Radiat. Transfer*, 109, 831–852, doi:10.1016/j.jqsrt.2007.09.004, 2008.
- Ptashnik, I. V., Smith, K. M., Shine, K. P., and Newnham, D. A.: Laboratory measurements of water vapour continuum absorption in spectral region 5000-5600 cm^{-1} : Evidence for water dimers, *Q. J. Roy. Meteor. Soc.*, 130, 2391–2408, doi:10.1256/qj.03.178, 2004.
- Ptashnik, I. V., McPheat, R. A., Shine, K. P., Smith, K. M., and Williams, R. G.: Water vapor self-continuum absorption in near-infrared windows derived from laboratory measurements, *J. Geophys. Res.*, 116, D16305, doi:10.1029/2011JD015603, 2011.
- Ptashnik, I. V., McPheat, R. A., Shine, K. P., Smith, K. M., and Williams, R. G.: Water vapour foreign-continuum absorption in near-infrared windows from laboratory measurements, *Philos. T. Roy. Soc. A.*, 370, 2557–2577, doi:10.1098/rsta.2011.0218, 2012.
- Ptashnik, I. V., Petrova, T. M., Ponomarev, Y., Shine, K. P., Solodov, A. A., and Solodov, A. M.: Near-infrared water vapour self-continuum at close to room temperature, *J. Quant. Spectrosc. Radiat. Transfer*, 120, 23–35, doi:10.1016/j.jqsrt.2013.02.016, 2013.
- Ptashnik, I. V., Petrova, T. M., Ponomarev, Y. N., Solodov, A. A., and Solodov, A. M.: Water vapor continuum absorption in near-IR atmospheric windows, *Atmos. Ocean. Opt.*, 28, 115–120, doi:10.1134/S1024856015020098, 2015.
- Quinn, P. K. and Coffman, D. J.: Local closure during the First Aerosol Characterization Experiment (ACE 1): Aerosol mass concentration and scattering and backscattering coefficients, *J. Geophys. Res.*, 103, 16 575–16 596, doi:10.1029/97JD03757, 1998.
- Rädel, G., Shine, K. P., and Ptashnik, I. V.: Global radiative and climate effect of the water vapour continuum at visible and near-infrared wavelengths, *Q. J. Roy. Meteor. Soc.*, 141, 727–738, doi:10.1002/qj.2385, 2015.
- Ramanathan, V. and Inamdar, A.: The radiative forcing due to clouds and water vapor, in: *Frontiers of Climate Modeling*, Kiehl, J. T. and Ramanathan, V. (eds.), Cambridge University Press, Cambridge, UK, 119–151, 2006.
- Reichert, A., Hausmann, P., and Sussmann, R.: Pointing errors in solar absorption spectrometry - correction scheme and its validation, *Atmos. Meas. Tech.*, 8, 3715–3728, doi:10.5194/amt-8-3715-2015, 2015.

Revercomb, H. E., Buijs, H., Howell, H. B., LaPorte, D. D., Smith, W. L., and Sromovsky, L. A.: Radiometric calibration of IR Fourier transform spectrometers: solution to a problem with the High-Resolution Interferometer Sounder, *Appl. Opt.*, 27, 3210–3218, doi:10.1364/AO.27.003210, 1988.

Roeckner, E., Arpe, K., Bengtsson, L., Christoph, M., Claussen, M., Dmenil, L., Esch, M., Giorgetta, M., Schlese, M., and Schulzweida, U.: The atmospheric general circulation model ECHAM-4: Model description and simulation of present-day climate, MPI-Report No. 218, Max-Planck-Institut für Meteorologie, Hamburg, Germany, 1996.

Rose, T., Crewell, S., Löhner, U., and Simmer, C.: A network suitable microwave radiometer for operational monitoring of the cloudy atmosphere, *Atmos. Res.*, 75, 183–200, doi:10.1016/j.atmosres.2004.12.005, 2005.

Rothman, L. S., Gordon, I. E., Babikov, Y., Barbe, A., Chris Benner, D., Bernath, P. F., Birk, M., Bizzocchi, L., Boudon, V., Brown, L. R., Campargue, A., Chance, K., Cohen, E. A., Coudert, L. H., Devi, V. M., Drouin, B. J., Fayt, A., Flaud, J.-M., Gamache, R. R., Harrison, J. J., Hartmann, J.-M., Hill, C., Hodges, J. T., Jacquemart, D., Jolly, A., Lamouroux, J., Le Roy, R. J., Li, G., Long, D. A., Lyulin, O. M., Mackie, C. J., Massie, S. T., Mikhailenko, S., Müller, H. S. P., Naumenko, O. V., Nikitin, A. V., Orphal, J., Perevalov, V., Perrin, A., Polovtseva, E. R., Richard, C., Smith, M. A. H., Starikova, E., Sung, K., Tashkun, S., Tennyson, J., Toon, G. C., Tyuterev, V. G., and Wagner, G.: The HITRAN2012 molecular spectroscopic database, *J. Quant. Spectrosc. Radiat. Transfer*, 130, 4–50, doi:10.1016/j.jqsrt.2013.07.002, 2013.

Rowe, P. M. and Walden, V. P.: Improved measurements of the foreign-broadened continuum of water vapor in the 6.3 μm band at -30 °C, *Appl. Opt.*, 48, 1358–1365, doi:10.1364/AO.48.001358, 2009.

Rowe, P. M., Walden, V. P., and Warren, S. G.: Measurements of the foreign-broadened continuum of water vapor in the 6.3 μm band at -30 °C, *Appl. Opt.*, 45, 4366–4382, doi:10.1364/AO.45.004366, 2006.

Schneider, M., Barthlott, S., Hase, F., González, Y., Yoshimura, K., García, O. E., Sepúlveda, E., Gomez-Pelaez, A., Gisi, M., Kohlhepp, R., Dohe, S., Blumenstock, T., Wiegele, A., Christner, E., Strong, K., Weaver, D., Palm, M., Deutscher, N. M., Warneke, T., Notholt, J., Lejeune, B., Demoulin, P., Jones, N., Griffith, D. W. T., Smale, D., and Robinson, J.: Ground-based remote sensing of tropospheric water vapour isotopologues within the project MUSICA, *Atmos. Meas. Tech.*, 5, 3007–3027, doi:10.5194/amt-5-3007-2012, 2012.

Schneider, M., Wiegele, A., Barthlott, S., González, Y., Christner, E., Dyroff, C., García, O. E., Hase, F., Blumenstock, T., Sepúlveda, E., Mengistu Tsidiu, G., Takele Kenea, S., Rodríguez, S., and Andrey, J.: Accomplishments of the MUSICA project to provide accurate, long-term, global and high-resolution observations of tropospheric $\{\text{H}_2\text{O}, \delta\text{D}\}$ pairs-a review, *Atmos. Meas. Tech.*, 9, 2845–2875, doi:10.5194/amt-9-2845-2016, 2016.

- Serio, C., Masiello, G., Esposito, F., di Girolamo, P., di Iorio, T., Palchetti, L., Bianchini, G., Muscari, G., Pavese, G., Rizzi, R., Carli, B., and Cuomo, V.: Retrieval of foreign-broadened water vapor continuum coefficients from emitted spectral radiance in the H₂O rotational band from 240 to 590 cm⁻¹, *Opt. Express*, 16, 15 816, doi:10.1364/OE.16.015816, 2008.
- Shine, K. P., Ptashnik, I. V., and Rädel, G.: The Water Vapour Continuum: Brief History and Recent Developments, *Surv. Geophys.*, 33, 535–555, doi:10.1007/s10712-011-9170-y, 2012.
- Shine, K. P., Campargue, A., Mondelain, D., McPheat, R. A., Ptashnik, I. V., and Weidmann, D.: The water vapour continuum in near-infrared windows-Current understanding and prospects for its inclusion in spectroscopic databases, *J. Mol. Spectrosc.*, doi:10.1016/j.jms.2016.04.011, in press, 2016.
- Sierk, B., Solomon, S., Daniel, J. S., Portmann, R. W., Gutman, S. I., Langford, A. O., Eubank, C. S., Dutton, E. G., and Holub, K. H.: Field measurements of water vapor continuum absorption in the visible and near-infrared, *J. Geophys. Res.*, 109, D08 307, doi:10.1029/2003JD003586, 2004.
- Snodgrass, H. B. and Ulrich, R. K.: Rotation of Doppler features in the solar photosphere, *Astrophys. J.*, 351, 309–316, doi:10.1086/168467, 1990.
- Staehelin, J., Kerr, J., Evans, R., and Vanicek, K.: Comparison of total ozone measurements of Dobson and Brewer spectrophotometers and recommended transfer functions, WMO TD No. 1147, WMO, Geneva, Switzerland, 2003.
- Sussmann, R. and Camy-Peyret, C.: Ground-Truthing Center Zugspitze, Germany for AIRS/IASI Validation, Phase I Report, EUMETSAT, Darmstadt, Germany, 2002.
- Sussmann, R. and Camy-Peyret, C.: Ground-Truthing Center Zugspitze, Germany for AIRS/IASI Validation, Phase II Report, EUMETSAT, Darmstadt, Germany, 2003.
- Sussmann, R. and Schäfer, K.: Infrared spectroscopy of tropospheric trace gases: combined analysis of horizontal and vertical column abundances, *Appl. Opt.*, 36, 735–741, doi:10.1364/AO.36.000735, 1997.
- Sussmann, R., Borsdorff, T., Rettinger, M., Camy-Peyret, C., Demoulin, P., Duchatelet, P., Mahieu, E., and Servais, C.: Technical Note: Harmonized retrieval of column-integrated atmospheric water vapor from the FTIR network - first examples for long-term records and station trends, *Atmos. Chem. Phys.*, 9, 8987–8999, doi:10.5194/acp-9-8987-2009, 2009.
- Sussmann, R., Forster, F., Rettinger, M., and Jones, N.: Strategy for high-accuracy-and-precision retrieval of atmospheric methane from the mid-infrared FTIR network, *Atmos. Meas. Tech.*, 4, 1943–1964, doi:10.5194/amt-4-1943-2011, 2011.
- Sussmann, R., Forster, F., Rettinger, M., and Bousquet, P.: Renewed methane increase for five years (2007–2011) observed by solar FTIR spectrometry, *Atmos. Chem. Phys.*, 12, 4885–4891, doi:10.5194/acp-12-4885-2012, 2012.

Thuillier, G., Hersé, M., Labs, D., Foujols, T., Peetermans, W., Gillotay, D., Simon, P. C., and Mandel, H.: The Solar Spectral Irradiance from 200 to 2400 nm as Measured by the SOLSPEC Spectrometer from the Atlas and Eureca Missions, *Sol. Phys.*, 214, 1–22, doi:10.1023/A:1024048429145, 2003.

Thuillier, G., Bolsée, D., Schmidtke, G., Foujols, T., Nikutowski, B., Shapiro, A. I., Brunner, R., Weber, M., Erhardt, C., Hersé, M., Gillotay, D., Peetermans, W., Decuyper, W., Pereira, N., Haberreiter, M., Mandel, H., and Schmutz, W.: The Solar Irradiance Spectrum at Solar Activity Minimum Between Solar Cycles 23 and 24, *Sol. Phys.*, 289, 1931–1958, doi:10.1007/s11207-013-0461-y, 2014.

Thuillier, G., Harder, J. W., Shapiro, A., Woods, T. N., Perrin, J.-M., Snow, M., Sukhodolov, T., and Schmutz, W.: The Infrared Solar Spectrum Measured by the SOLSPEC Spectrometer Onboard the International Space Station, *Sol. Phys.*, 290, 1581–1600, doi:10.1007/s11207-015-0704-1, 2015.

Tipping, R. H. and Ma, Q.: Theory of the water vapor continuum and validations, *Atmos. Res.*, 36, 69–94, doi:10.1016/0169-8095(94)00028-C, 1995.

Tobin, D. C., Best, F. A., Brown, P. D., Clough, S. A., Dedecker, R. G., Ellingson, R. G., Garcia, R. K., Howell, H. B., Knuteson, R. O., Mlawer, E. J., Revercomb, H. E., Short, J. F., van Delst, P. F. W., and Walden, V. P.: Downwelling spectral radiance observations at the SHEBA ice station: Water vapor continuum measurements from 17 to 26 μm , *J. Geophys. Res.*, 104, 2081–2092, doi:10.1029/1998JD200057, 1999.

Tobin, D. C., Revercomb, H. E., Knuteson, R. O., Lesht, B. M., Strow, L. L., Hannon, S. E., Feltz, W. F., Moy, L. A., Fetzer, E. J., and Cress, T. S.: Atmospheric Radiation Measurement site atmospheric state best estimates for Atmospheric Infrared Sounder temperature and water vapor retrieval validation, *J. Geophys. Res.*, 111, D09S14, doi:10.1029/2005JD006103, 2006.

Toledano, C., Wiegner, M., Garhammer, M., Seefeldner, M., Gasteiger, J., Mller, D., and Koepke, P.: Spectral aerosol optical depth characterization of desert dust during SAMUM 2006, *Tellus B*, 61, 216–228, doi:10.1111/j.1600-0889.2008.00382.x, 2009.

Toon, G., Blavier, J.-F., Washenfelder, R., Wunch, D., Keppel-Aleks, G., Wennberg, P., Connor, B., Sherlock, V., Griffith, D., Deutscher, N., and Notholt, J.: Total Column Carbon Observing Network (TCCON), Advances in Imaging, OSA Technical Digest (CD), Fourier Transform Spectroscopy 2009, Vancouver, Canada, 26-30 April, JMA3, 2009.

Turner, D. D. and Mlawer, E. J.: The Radiative Heating in Underexplored Bands Campaigns, *Bull. Am. Meteorol. Soc.*, 91, 911–923, doi:10.1175/2010BAMS2904.1, 2010.

Turner, D. D., Tobin, D. C., Clough, S. A., Brown, P. D., Ellingson, R. G., Mlawer, E. J., Knuteson, R. O., Revercomb, H. E., Shippert, T. R., Smith, W. L., and Shephard, M. W.: The QME AERI LBLRTM: A Closure Experiment for Downwelling High Spectral Resolution Infrared Radiance., *J. Atmos. Sc.*, 61, 2657–2675, doi:10.1175/JAS3300.1, 2004.

- Turner, D. D., Knuteson, R. O., Revercomb, H. E., Lo, C., and Dedecker, R. G.: Noise Reduction of Atmospheric Emitted Radiance Interferometer (AERI) Observations Using Principal Component Analysis, *J. Atmos. Ocean. Tech.*, 23, 1223–1238, doi:10.1175/JTECH1906.1, 2006.
- Turner, D. D., Merrelli, A., Vimont, D., and Mlawer, E. J.: Impact of modifying the longwave water vapor continuum absorption model on community Earth system model simulations, *J. Geophys. Res.*, 117, D04106, doi:10.1029/2011JD016440, 2012a.
- Turner, D. D., Mlawer, E. J., Bianchini, G., Cadeddu, M. P., Crewell, S., Delamere, J. S., Knuteson, R. O., Maschwitz, G., Mlynaczak, M., Paine, S., Palchetti, L., and Tobin, D. C.: Ground-based high spectral resolution observations of the entire terrestrial spectrum under extremely dry conditions, *Geophys. Res. Lett.*, 39, L10801, doi:10.1029/2012GL051542, 2012b.
- Tyndall, J.: On the Absorption and Radiation of Heat by Gases and Vapours, and on the Physical Connexion of Radiation, Absorption, Conduction, *Philos. Mag.*, 4, 169–94, 273–85, 1861.
- Ventrillard, I., Romanini, D., Mondelain, D., and Campargue, A.: Accurate measurements and temperature dependence of the water vapor self-continuum absorption in the 2.1 μm atmospheric window, *J. Chem. Phys.*, 143, 134304, doi:10.1063/1.4931811, 2015.
- Vogelmann, H., Sussmann, R., Trickl, T., and Reichert, A.: Spatiotemporal variability of water vapor investigated using lidar and FTIR vertical soundings above the Zugspitze, *Atmos. Chem. Phys.*, 15, 3135–3148, doi:10.5194/acp-15-3135-2015, 2015.
- Washenfelder, R. A., Toon, G. C., Blavier, J.-F., Yang, Z., Allen, N. T., Wennberg, P. O., Vay, S. A., Matross, D. M., and Daube, B. C.: Carbon dioxide column abundances at the Wisconsin Tall Tower site, *J. Geophys. Res.*, 111, D22305, doi:10.1029/2006JD007154, 2006.
- Weber, M.: Comment on the Article by Thuillier et al. “The Infrared Solar Spectrum Measured by the SOLSPEC Spectrometer onboard the International Space Station”, *Sol. Phys.*, 290, 1601–1605, doi:10.1007/s11207-015-0707-y, 2015.
- Wild, M., Folini, D., Schär, C., Loeb, N., Dutton, E. G., and König-Langlo, G.: The global energy balance from a surface perspective, *Clim. Dynam.*, 40, 3107–3134, doi:10.1007/s00382-012-1569-8, 2013.
- Wunch, D., Toon, G. C., Blavier, J.-F. L., Washenfelder, R. A., Notholt, J., Connor, B. J., Griffith, D. W. T., Sherlock, V., and Wennberg, P. O.: The Total Carbon Column Observing Network, *Philos. T. Roy. Soc. A.*, 369, 2087–2112, doi:10.1098/rsta.2010.0240, 2011.
- Zdunkowski, W., Trautmann, T., and Bott, A.: *Radiation in the Atmosphere*, Cambridge University Press, Cambridge, UK, doi:10.1017/CBO9780511535796, 2007.

List of Figures

1.1	Schematic overview of the Earth's mean global energy balance.	10
1.2	Optical depth of spectral lines throughout the infrared.	11
1.3	Standard definition of the water vapor continuum.	14
1.4	Water vapor OD for a mid-latitude winter standard atmosphere.	15
3.1	Logical scheme of the Zugspitze radiative closure experiment.	26
4.1	Schematic overview of the Michelson-type interferometer used in the solar FTIR technique.	30
5.1	Schematics of the mispointing determination strategy.	37
5.2	Conversion of solar shift to radial mispointing.	39
5.3	Linear approximation of differential rotation.	40
5.4	Calculation of sun axis orientation relative to zenith direction.	43
5.5	Calculation of mispointing uncertainty.	44
5.6	Geometry of the Zugspitze solar tracker optics.	45
5.7	Time series of solar line shifts determined from Zugspitze FTIR spectra. . . .	46
5.8	Choice of time bin size for Zugspitze mispointing determination.	49
6.1	Blackbody calibration source.	53
6.2	Selection of spectra for the Langley measurements.	55
6.3	Selection of suitable spectral points and averaging for Langley calibration . . .	57
6.4	Blackbody radiance spectrum and further analysis.	58
6.5	Relative 2σ calibration uncertainty.	60
7.1	Instrumental setup of the Zugspitze radiative closure experiment.	65
7.2	Climatology of integrated water vapor above the Zugspitze.	66

7.3	Relative uncertainty of the IWV fit.	69
7.4	Number of spectral channels included in the IWV fit.	70
7.5	Relative adjustment IWV/IWV _{LHATPRO}	70
7.6	Uncertainty analysis of NCEP water vapor profile shape.	77
7.7	Derivative of surface downwelling radiance with respect to water vapor profile shape.	77
7.8	Uncertainty analysis of T profiles used in the closure experiment.	78
7.9	Derivative of surface downwelling radiance with respect to the T profile.	78
7.10	Residual uncertainty (2- σ) of the FIR and MIR closure experiment	80
7.11	Residual uncertainty (2- σ) of the NIR closure experiment.	81
8.1	AERI mean spectral residuals.	84
9.1	Mispointing results determined from Zugspitze measurements.	94
9.2	Comparison of a posteriori-corrected and uncorrected Zugspitze XCH ₄ monthly mean time series.	95
10.1	Combined calibration curve and selected Langley calibration points.	100
10.2	Validation of calibration results.	101
11.1	Mean foreign continuum coefficients derived from the Zugspitze closure measurements.	106
11.2	Mean continuum absorption coefficient \bar{k}_{cont} determined in the Zugspitze closure experiment.	108
11.3	Effect of ESS uncertainty on the continuum absorption coefficient \bar{k}_{cont} determined in the Zugspitze closure experiment.	111
11.4	Non-logarithmic plot of the effect of ESS uncertainty on the continuum absorption coefficient \bar{k}_{cont}	112

List of Tables

6.1	Specifications of the blackbody calibration source.	52
7.1	Climatological statistics of clear-sky IWV levels above the Zugspitze derived from solar FTIR measurements.	64
7.2	Instruments and geophysical parameters measured at the Zugspitze radiative closure experiment.	68
7.3	Central wavelength and FWHM of the sun photometer (SSARA-Z) filters. .	72
9.1	XCH ₄ trend for the April 2006–March 2015 time interval, Zugspitze and Garmisch sites.	97
9.2	Bias of XCH ₄ monthly means between Garmisch and Zugspitze measurements. .	97
11.1	Mean foreign continuum coefficients derived from the Zugspitze closure measurements	106
11.2	Mean atmospheric state of the closure data set.	109

List of Acronyms

(ER-)AERI	(Extended Range -) Atmospheric Emitted Radiance Interferometer (Knuteson et al., 2004a, 2004b)
AOD	Aerosol optical depth
ARM	Atmospheric Radiation Measurement program (Ackerman and Stokes, 2003)
BPS-MT-CKD	Baranov, Paynter, Serio, Mlawer, Tobin, Clough, Kneizys and Davies continuum model (Paynter and Ramaswamy, 2014)
CAVIAR	Continuum Absorption at Visible and Infrared wavelengths and its Atmospheric Relevance consortium
CESM	Community Earth System Model
CKD	Clough, Kneizys and Davies continuum model (Clough et al., 1989)
CRDS	Cavity ring-down spectroscopy
ECHAM4	ECMWF Hamburg global circulation model(Roeckner et al., 1996)
ECOWAR	Earth Cooling by Water Vapor Radiation project
ESS	Extra-atmospheric solar spectrum
FIR	Far infrared
FOV	Field of view

FTIR	Fourier transform infrared
FWHM	Full width at half maximum
GFDL	Geophysical Fluid Dynamics Laboratory
HITRAN	High-resolution Transmission Molecular Absorption Database (Rothman et al., 2013)
ILS	Instrumental line shape
IWV	Integrated water vapor
LBLRTM	Line-by-line Radiative Transfer Model (Clough et al., 2005)
LHATPRO	Low Humidity and Temperature Profile Microwave Radiometer
LWP	Liquid water path
NCEP	National Center for Environmental Prediction
NDACC	Network of the Detection of Atmospheric Composition Change (Kurylo, 1991)
NIR	Near infrared
MIR	Mid-infrared
MT_CKD	Mlawer, Tobin, Clough, Kneizys and Davies continuum model (Mlawer et al., 2012)
OD	Optical depth
OF-CEAS	Optical feedback cavity enhanced spectroscopy
OPD	Optical path difference
PROFFIT	Profile Fit (trace gas retrieval software, Hase et al., 2004)
RHUBC	Radiative Heating in Underexplored Bands Campaigns (Turner and Mlawer, 2010)
RRTM	Rapid Radiative Transfer Model (Mlawer et al., 1997)
SSARA-Z	Sun-sky Automatic Radiometer - Zugspitze (Toledano et al., 2009)

sza	Solar zenith angle
TCCON	Total Carbon Column Observing Network(Wunch et al., 2011)
UV	Ultra-violet
XCH₄	Column-averaged mole fraction of methane

Publications

This section contains a list of publications in peer-reviewed journals and contributions to international conferences that have been prepared on the subject of this thesis.

Publications in Peer-reviewed Journals

- [1] Reichert, A., Hausmann, P., and Sussmann, R.: Pointing errors in solar absorption spectrometry - correction scheme and its validation, *Atmos. Meas. Tech.*, 8, 3715-3728, doi:10.5194/amt-8-3715-2015, 2015.
- [2] Vogelmann, H., Sussmann, R., Trickl, T., and Reichert, A.: Spatio-temporal variability of water vapor investigated by lidar and FTIR vertical soundings above Mt. Zugspitze, *Atmos. Chem. Phys.*, 15, 3135-3148, doi:10.5194/acp-15-3135-2015, 2015.

Publications Submitted to Peer-reviewed Journals

- [3] Reichert, A., Rettinger, M., and Sussmann, R.: The Zugspitze radiative closure experiment for quantifying water vapor absorption over the terrestrial and solar infrared. Part II: Accurate calibration of high spectral resolution infrared measurements of surface solar radiation, *Atmos. Meas. Tech. Discuss.*, doi:10.5194/amt-2016-127, in review, 2016.
- [4] Reichert, A. and Sussmann, R.: The Zugspitze radiative closure experiment for quantifying water vapor absorption over the terrestrial and solar infrared. Part III: Quantification of the near-infrared water vapor continuum under atmospheric conditions, *Atmos. Chem. Phys. Discuss.*, doi:10.5194/acp-2016-323, in review, 2016.
- [5] Sussmann, R., Reichert, A., and Rettinger, M.: The Zugspitze radiative closure experiment for quantifying water vapor absorption over the terrestrial and solar infrared. Part I: Setup, uncertainty analysis, and assessment of far-infrared water vapor continuum, *Atmos. Chem. Phys. Discuss.*, doi:10.5194/acp-2016-321, in review, 2016.

Contributions to International Conferences

- [6] Reichert, A., Sussmann, R., and Rettinger, M.: Quantification of the Near-Infrared Water Vapor Continuum from Atmospheric Measurements at the Zugspitze, International Radiation Symposium, Auckland, New Zealand, 16–22 April, 2016.
- [7] Reichert, A., Rettinger, M., and Sussmann, R.: A novel method for accurate calibration of high spectral resolution infrared measurements of surface solar radiation, International Radiation Symposium, Auckland, New Zealand, 16–22 April, 2016.
- [8] Reichert, A., Sussmann, R., and Rettinger, M.: Improved quantification of far-infrared water vapor absorption by long-term radiative closure measurements at the Zugspitze, International Radiation Symposium, Auckland, New Zealand, 16–22 April, 2016.
- [9] Reichert, A., Sussmann, R., and Rettinger, M.: The Zugspitze radiative closure experiment: quantification of the near-infrared water vapor continuum from atmospheric measurements, EGU General Assembly, Vienna, Austria, 17-22 April, EGU2016–13494, 2016.
- [10] Reichert, A., Hausmann, P., and Sussmann, R.: Determination and correction of pointing errors in solar FTIR spectrometry, Int. Joint Workshop of the NDACC Infrared Working Group and the TCCON Science Team, Toronto, Canada, 8–12 June, 2015.
- [11] Reichert, A., Sussmann, R., and Rettinger, M.: The Zugspitze water vapor radiative closure experiment. Part 2: validation of continuum coefficients in the far-IR, Int. Joint Workshop of the NDACC Infrared Working Group and the TCCON Science Team, Toronto, Canada, 8–12 June 2015, 2015.
- [12] Vogelmann, H., Sussmann, R., Trickl, T., and Reichert, A.: Spatio-Temporal Variability of Water Vapor in the Free Troposphere Investigated by DIAL and FTIR Vertical Soundings, EPJ Web of Conferences Volume 119, 27th International Laser and Radar Conference, New York, USA, 5–10 July, 24006, 2015.
- [13] Vogelmann, H., Sussmann, R., Trickl, T., and Reichert, A.: Spatio-Temporal Variability of Water Vapor Investigated by LIDAR and FTIR vertical soundings above Mt. Zugspitze, Verhandl. DPG (VI) 50, Heidelberg, Germany, 23–27 March, UP2.3, 2015.
- [14] Reichert, A., Sussmann, R., and Rettinger, M.: Quantification of the water vapor greenhouse effect: setup and first results of the Zugspitze radiative closure experiment, EGU General Assembly, Vienna, Austria, 27 April-02 May, EGU2014–5349, 2014.
- [15] Vogelmann, H., Sussmann, R., Trickl, T., and Reichert, A.: Spatio-temporal variability of water vapor investigated by lidar and FTIR vertical soundings above Mt. Zugspitze, EGU General Assembly, Vienna, Austria, 27 April-02 May, EGU2014-7204, 2014.
- [16] Sussmann R., Rettinger M., Hausmann, P., Ostler, A., and Reichert, A.: Garmisch (TCCON) and Zugspitze (NDACC) site news, Int. Joint Workshop of the NDACC Infrared Working Group and the TCCON Science Team, Bad Sulza, Germany, 12–15 May, 2014.

- [17] Reichert, A., Sussmann, R., Rettinger, M., Klanner, L., Trickl, T., and Vogelmann, H.: The Zugspitze Water Vapor Radiative Closure Experiment, NDACC Steering Committee Meeting, Garmisch-Partenkirchen, Germany, 15–18 October, 2012.

Acknowledgments

First of all, I would like to thank my supervisors who provided outstanding guidance and continuously excellent support throughout my PhD:

I am indebted to my supervisor at KIT/IMK-IFU, PD Dr. Ralf Sussmann for elaborating and offering me the very interesting theme for my dissertation in a highly topical research field. This work was made possible by his excellent and dedicated scientific advice and discussions that crucially endorsed my development as a scientist. He helped to overcome obstacles in the project, e.g. through his support to purchase the LHATPRO, the funding of frequent participation in international conferences and much more. I am very grateful for the excellent working conditions, i.e. the top level instrumentation and the inspiring atmosphere he created in the working group “Atmospheric Variability and Trends”. Furthermore, I am thankful for his consent to review this thesis as coexaminer. Not least I thank Ralf Sussmann for elaborating the concept of my successful PhD grant application to DBU as well as for subsequent funding via two BStMUV projects lead by him.

I am equally grateful to my supervisor at LMU München, Professor Bernhard Mayer. First of all, I am very thankful for the warm welcome that he provided me as a PhD student from an external research institution at LMU München. He enabled this work by his very trustworthy disposition to assume the academic supervision of my PhD and via his outstanding support in many occasions. Throughout this work, his scientific and academic mentoring and advice was of vital importance. This project would not have been possible without his frequent and excellent support in administrative issues, especially concerning the cooperation with Deutsche Bundesstiftung Umwelt. Finally, I am very grateful that he agreed to conduct the review of this thesis as primary examiner.

I am very thankful to Professor Hans Peter Schmid (KIT/IMK-IFU and Technische Universität München), director of KIT/IMK-IFU. His ongoing efforts enable outstanding working conditions at KIT/IMK-IFU, which were of vital importance for this project. I want to thank for his continuous interest in this work and his crucial institutional support to purchase the LHATPRO.

This work has been significantly supported by the scientific contributions of my colleagues at KIT/IMK-IFU and a number of external contributions:

Markus Rettinger (KIT/IMK-IFU) provided ongoing support in instrument-related questions, and assisted in all modifications considering the instrumentation at the Zugspitze observatory throughout my work. The data set used in this study is a result of his unceasing

effort to maintain highly reliable routine operations at the Zugspitze observatory. Petra Hausmann (KIT/IMK-IFU) substantially supported this work by providing IWV retrievals as well as Frank Hase (KIT/IMK-ASF) via valuable discussions.

I am grateful to Matthias Wiegner (LMU München) for his vital support to this project by providing sun photometer measurement data. I furthermore want to thank Ulf Köhler (Meteorologisches Observatorium Hohenpeissenberg, DWD) for providing ozone column measurements. Fabian Jakub and Carolin Klinger (LMU München) provided helpful suggestions that contributed to improve this manuscript.

This project was funded by the Deutsche Bundesstiftung Umwelt via a dissertation grant. I would especially like to thank Dr. Maximilian Hempel, my advisor at Deutsche Bundesstiftung Umwelt, for his ongoing support. Further extensive funding by the Bavarian State Ministry of the Environment and Consumer Protection (contracts TLK01U-49581 and VAO-II TP I/01) is gratefully acknowledged.

I am very grateful to my colleagues in the working group “Atmospheric Variability and Trends” for making daily work life at KIT/IMK-IFU truly enjoyable. I especially want to thank my office mate Andreas Ostler (KIT/IMK-IFU) for providing company and advice in countless occasions throughout our respective PhD work.

Finally, I want to thank my family for their caring support in everyday life and for always being supportive and encouraging given the time and energy I dedicated to my PhD project.